Extrusion-based 3d freeze printing of multi-functional aerogels

by

Guang Yang

B.S., Kansas State University, 2015

AN ABSTRACT OF A DISSERTATION

submitted in partial fulfillment of the requirements for the degree

DOCTOR OF PHILOSOPHY

Department of Industrial and Manufacturing Systems Engineering
Carl R. Ice College of Engineering

KANSAS STATE UNIVERSITY
Manhattan, Kansas

2024

Abstract

Aerogels constitute a unique class of synthetic porous ultralight materials, derived from gels where the liquid component is substituted by gas while retaining the gel structure. Their outstanding material properties, including high porosity and low density, have spurred exploration across various domains such as catalysis, thermal insulation, solar energy utilization, piezoelectricity, energy storage, low-temperature glass formation, sensors, adsorption, and photocatalysis. The integration of 3D printing technology into aerogel production offers unprecedented design flexibility and the capacity to customize material characteristics. Nevertheless, prevailing 3D printing methods for aerogels encounter challenges concerning printability, microstructure regulation, and macrostructure manipulation.

To tackle these obstacles, a novel 3D printing method known as 3D Freeze Printing (3DFP) has been developed internally, merging freeze casting with additive manufacturing techniques. This approach facilitates the precise fabrication of tailored geometries with controlled microporous structures. Previous investigations have primarily focused on a limited range of materials such as graphene and silver nanowires, necessitating exploration into diverse materials to unlock the full potential of 3DFP. Additionally, comparative evaluations between multifunctional aerogels produced via 3DFP and those from conventional methods remain unexplored. Former studies predominantly relied on optical imaging for 3DFP characterization, constraining insights into material deposition and solidification. Systematic analysis of the extrusion process and quantitative assessment pose considerable challenges but are crucial for optimizing 3DFP processes across industries like chemical, machinery, electronics, aerospace, and biomedical engineering.

This thesis addresses these gaps by fundamentally studying the extrusion-based 3DFP method and its potential applications. After a comprehensive review of freeze casting and current extrusion-based 3D printing techniques, precedes investigations using X-ray synchrotron micro-radiography from leading facilities like the Advanced Photon Source and SLAC National Accelerator Laboratory are presented. These experiments provide real-time insights into material behavior during freeze casting and 3DFP processes. Moreover, the fabrication and characterization of novel cellulose nanocrystal (CNC) aerogels using 3DFP demonstrate exceptional acoustic absorption and mechanical properties tailored through freezing direction modification. These nano-cellulose aerogels present promising applications in ultra-lightweight sound absorption devices for aerospace use. Additionally, this thesis extends to extrusion-based 3D printing of zirconium carbide (ZrC) nuclear fuel cell structures, reporting the influence of additives like Nano Crystalline Cellulose (NCC) and Vanadium Carbide (VC) through rheological and mechanical testing. Integrating additive manufacturing with advanced materials like ZrC and tailored additives marks a significant stride towards sustainable propulsion systems for future space missions.

In conclusion, this thesis delves into the fundamental aspects and practical applications of extrusion-based 3DFP, paving the way for optimized aerogel production across diverse industries and advancing materials science for futuristic technologies.

Extrusion-based 3d freeze printing of multi-functional aerogels

by

Guang Yang

B.S., Kansas State University, 2015

A DISSERTATION

submitted in partial fulfillment of the requirements for the degree

DOCTOR OF PHILOSOPHY

Department of Industrial and Manufacturing Systems Engineering
Carl R. Ice College of Engineering

KANSAS STATE UNIVERSITY
Manhattan, Kansas

2024

Approved by:

Co-Major Professor
Dr. Dong Lin

Approved by:

Co-Major Professor
Dr. Shuting Lei

Copyright

Abstract

Aerogels constitute a unique class of synthetic porous ultralight materials, derived from gels where the liquid component is substituted by gas while retaining the gel structure. Their outstanding material properties, including high porosity and low density, have spurred exploration across various domains such as catalysis, thermal insulation, solar energy utilization, piezoelectricity, energy storage, low-temperature glass formation, sensors, adsorption, and photocatalysis. The integration of 3D printing technology into aerogel production offers unprecedented design flexibility and the capacity to customize material characteristics. Nevertheless, prevailing 3D printing methods for aerogels encounter challenges concerning printability, microstructure regulation, and macrostructure manipulation.

To tackle these obstacles, a novel 3D printing method known as 3D Freeze Printing (3DFP) has been developed internally, merging freeze casting with additive manufacturing techniques. This approach facilitates the precise fabrication of tailored geometries with controlled microporous structures. Previous investigations have primarily focused on a limited range of materials such as graphene and silver nanowires, necessitating exploration into diverse materials to unlock the full potential of 3DFP. Additionally, comparative evaluations between multifunctional aerogels produced via 3DFP and those from conventional methods remain unexplored. Former studies predominantly relied on optical imaging for 3DFP characterization, constraining insights into material deposition and solidification. Systematic analysis of the extrusion process and quantitative assessment pose considerable challenges but are crucial for optimizing 3DFP processes across industries like chemical, machinery, electronics, aerospace, and biomedical engineering.

This thesis addresses these gaps by fundamentally studying the extrusion-based 3DFP method and its potential applications. After a comprehensive review of freeze casting and current extrusion-based 3D printing techniques, precedes investigations using X-ray synchrotron micro-radiography from leading facilities like the Advanced Photon Source and SLAC National Accelerator Laboratory are presented. These experiments provide real-time insights into material behavior during freeze casting and 3DFP processes. Moreover, the fabrication and characterization of novel cellulose nanocrystal (CNC) aerogels using 3DFP demonstrate exceptional acoustic absorption and mechanical properties tailored through freezing direction modification. These nano-cellulose aerogels present promising applications in ultra-lightweight sound absorption devices for aerospace use. Additionally, this thesis extends to extrusion-based 3D printing of zirconium carbide (ZrC) nuclear fuel cell structures, reporting the influence of additives like Nano Crystalline Cellulose (NCC) and Vanadium Carbide (VC) through rheological and mechanical testing. Integrating additive manufacturing with advanced materials like ZrC and tailored additives marks a significant stride towards sustainable propulsion systems for future space missions.

In conclusion, this thesis delves into the fundamental aspects and practical applications of extrusion-based 3DFP, paving the way for optimized aerogel production across diverse industries and advancing materials science for futuristic technologies.

Table of Contents

List of Figures

List of Tables

Acknowledgements

I would like to express my deepest gratitude and appreciation to everyone who contributed to the completion of this Ph.D. thesis. Without their support, guidance, and encouragement, this work would not have been possible.

First and foremost, I am indebted to my advisors, Dr. Shuting Lei and Dr. Dong Lin, for their invaluable mentorship, expertise, and unwavering support throughout this journey. Their insightful feedback, patience, and dedication have been instrumental in shaping this research and improving the quality of this thesis.

I am thankful to the members of my thesis committee, Dr. Shing Chang and Mark L Weiss, for their valuable input, suggestions, and constructive criticism, which have greatly enriched this work.

I want to express my heartfelt appreciation to Dr. Chih-Hang (John) Wu for his steadfast support during the completion of this doctoral thesis. His encouragement and mentorship have been invaluable, and I am grateful for the opportunity he provided me to serve as the department IT. Dr. Wu's belief in my abilities and his unwavering support have been instrumental in this endeavor.

I extend my gratitude to Kansas State University for providing resources, facilities, and a conducive research environment that facilitated the progress of this research.

I am thankful to my colleagues and fellow researchers at the Industrial and Manufacturing System Engineering Department for their camaraderie, insightful discussions, and shared experiences. Their contributions have enriched my understanding and perspectives on various aspects of this study.

I am profoundly grateful for the support and understanding of my family during this demanding period; their love, encouragement, and belief in my abilities have been a constant source of motivation. I am especially thankful to my wife, Binghui Liu, for her unwavering support, understanding, and love throughout this Ph.D. journey. Her encouragement, sacrifices, and belief in me have been my driving force, and I feel incredibly fortunate to have her by my side. Thank you, Binghui, for being my constant source of strength and inspiration.

Lastly, I express my appreciation to all individuals, whether mentioned here or not, who in one way or another contributed to this research endeavor.

Thank you all for your contributions, encouragement, and belief in the importance of this work.

Chapter 1 - Introduction

Aerogel represents a class of synthetic porous ultralight materials derived from gels, where the liquid component is replaced by gas without compromising the gel structure's integrity [1]. The inception of aerogel dates back to 1931 when Samuel Stephens Kistler, an American scientist and chemical engineer, first invented it [2]. Since Kistler's groundbreaking discovery of silica aerogel, researchers worldwide have delved into exploring various materials such as metals, ceramics, polymers, and organic substances to synthesize aerogels [3]. The evolution of aerogel research has led to a profound understanding of its unique properties, which span from the nanoscale to the macroscale. These properties include high porosity, extremely low density, and exceptionally high surface area, making aerogels highly desirable for a wide range of applications across different industries.

Aerogels' remarkable properties have spurred extensive exploration in various fields such as catalysis, thermal insulation, solar energy utilization, piezoelectricity, energy storage, low-temperature glass formation, sensors, adsorption, and photocatalysis [4]. Their versatility and adaptability to diverse applications make aerogels a subject of continuous research and innovation. The synthesis of aerogels involves a series of intricate steps, including solution-sol transition, sol-gel transition (gelation), and gel-aerogel transition (drying). These steps are crucial in determining the microstructure of the aerogel, which in turn influences its properties and applications significantly.

In recent years, freeze casting, also known as ice templating, has emerged as a promising technique for fabricating controlled porous materials across various substrates, including ceramics, metals, polymers, biomacromolecules, and carbon-based materials [5]. Freeze casting involves controlled solidification of a solution, suspension, sol, or gel, followed by solvent

sublimation under reduced pressure and subsequent densification post-processing. By leveraging phase separation during solidification, freeze casting allows for tailored microstructures, although its macrostructure heavily depends on the mold geometry during processing.

Integrating Additive Manufacturing (AM) techniques into aerogel fabrication offers unparalleled design flexibility and the ability to tailor material properties as desired. AM, also known as 3D printing, encompasses techniques like stereolithography (SLA), selective laser sintering (SLS), fused deposition modeling (FDM), and direct ink writing (DIW), among others [8]. These techniques have revolutionized manufacturing capabilities but face challenges when applied to aerogel fabrication due to limited microstructure control and challenges in engineering both macrostructures and microstructures simultaneously.

To address these challenges, a novel method termed 3D Freeze Printing (3DFP) has been developed, combining the advantages of freeze casting with AM techniques for tailored micro-porous structures and customized geometries [9]. While 3DFP opens new possibilities for aerogel fabrication, several challenges persist in characterizing the process comprehensively, expanding material types beyond the current scope, and evaluating multifunctional aerogels against conventionally fabricated ones. Systematic analysis of extrusion processes and quantitative assessments are necessary for optimizing 3DFP across industries like chemical, machinery, electronics, aerospace, and biomedical engineering.

This thesis endeavors to delve deep into extrusion-based 3DFP's fundamentals and practical applications, bridging the gap between theory and real-world aerogel production. The research begins with a comprehensive review of freeze casting and current extrusion-based 3D printing techniques, leveraging advanced imaging techniques like X-ray synchrotron micro-

radiography from leading facilities to gain real-time insights into material behavior during freeze casting and 3DFP processes.

Moreover, the thesis showcases novel cellulose nanocrystal (CNC) aerogels' fabrication and characterization using 3DFP, demonstrating exceptional acoustic absorption and mechanical properties tailored through freezing direction modification. These nano-cellulose aerogels present promising applications in ultra-lightweight sound absorption devices for aerospace use, marking a significant advancement in lightweight material technology for aerospace applications.

Additionally, the exploration extends to extrusion-based 3D printing of zirconium carbide (ZrC) nuclear fuel cell structures, studying the influence of additives like NanoCrystalline Cellulose (NCC) and Vanadium Carbide (VC) through rheological and mechanical testing. The integration of additive manufacturing with advanced materials like ZrC and tailored additives marks a significant stride towards sustainable propulsion systems for future space missions, aligning with global efforts towards sustainable technological advancements.

In conclusion, this research encompasses two primary objectives. Firstly, it seeks to conduct a fundamental investigation into the key features of extrusion-based 3D Freeze Printing, namely material deposition and solidification, which significantly impact the quality of 3D printed samples. Secondly, it aims to introduce novel materials and explore advanced applications for 3DFP aerogels. The remainder of this thesis is structured as follows: a comprehensive review of the two key features (freeze casting technique and direct ink writing) is provided initially. Subsequently, the freeze casting process and 3DFP are characterized and visualized using synchrotron X-ray micro-radiography. Following this, a nano cellulose-based acoustic aerogel absorber tailored for aerospace applications is developed. Lastly, a 3D printed

zirconium carbide ceramic is engineered for nuclear fuel cells, with concurrent systematic study of ink rheology to optimize printability. Conclusions and avenues for future research are also outlined in the closing sections.

References

[1] J. Alemán, A.V. Chadwick, J. He, M. Hess, K. Horie, R.G. Jones, P. Kratochvíl, I. Meisel, I. Mita, G. Moad, Definitions of terms relating to the structure and processing of sols, gels, networks, and inorganic-organic hybrid materials (IUPAC Recommendations 2007), Pure and Applied Chemistry 79(10) (2007) 1801-1829.

[2] S.S. Kistler, Coherent expanded aerogels and jellies, Nature 127(3211) (1931) 741-741.

[3] H. Tetik, Y. Wang, X. Sun, D. Cao, N. Shah, H. Zhu, F. Qian, D. Lin, Additive manufacturing of 3D aerogels and porous scaffolds: a review, Advanced Functional Materials 31(45) (2021) 2103410.

[4] A. Du, B. Zhou, Z. Zhang, J. Shen, A special material or a new state of matter: a review and reconsideration of the aerogel, Materials 6(3) (2013) 941-968.

[5] S. Deville, E. Saiz, R.K. Nalla, A.P. Tomsia, Freezing as a path to build complex composites, Science 311(5760) (2006) 515-518.

[6] G. Shao, D.A. Hanaor, X. Shen, A. Gurlo, Freeze casting: from low‐dimensional building blocks to aligned porous structures—a review of novel materials, methods, and applications, Advanced Materials 32(17) (2020) 1907176.

[7] S.H. Huang, P. Liu, A. Mokasdar, L. Hou, Additive manufacturing and its societal impact: a literature review, The International Journal of Advanced Manufacturing Technology 67(5) (2013) 1191-1203.

[8] K.V. Wong, A. Hernandez, A review of additive manufacturing, International scholarly research notices 2012 (2012).

[9] X. Song, H. Tetik, T. Jirakittsonthon, P. Parandoush, G. Yang, D. Lee, S. Ryu, S. Lei, M.L. Weiss, D. Lin, Biomimetic 3D printing of hierarchical and interconnected porous hydroxyapatite

structures with high mechanical strength for bone cell culture, Advanced Engineering Materials 21(1) (2019) 1800678.

Chapter 2 - Review of Key Features in 3D Freeze Printing

Abstract

Over the past few decades, significant advancements have been made in additive manufacturing (3D printing) techniques, enabling the fabrication of complex geometries in aerogels with tailored macrostructures. Despite these strides, the lack of microstructure control during the 3D printing process poses limitations on the mechanical properties and potential applications of 3D printed aerogels. To address this challenge, we have developed the 3D Freeze Printing (3DFP) technique, which integrates the benefits of additive manufacturing with freeze casting. This innovative approach empowers us to produce customized geometries while maintaining control over microstructures. This section provides a review of freeze casting techniques and the current state of extrusion-based 3D printing, aiming to enhance our understanding of the capabilities offered by the 3DFP technique.

2.1 Review of the Freeze Casting Technique

2.1.1 Introduction of Freeze Casting

Freeze casting, also known as ice templating, is a highly versatile technique that has gained significant traction in recent years for fabricating controllable porous materials across various domains such as ceramics, metals, polymers, biomacromolecules, and carbon materials. This process imparts new properties to these materials, broadening their applicability in different fields. Similar to natural systems, the cell templates produced through freeze casting can imbue structures with diverse physical and mechanical properties. Consequently, freeze casting

represents a logical approach for designing synthetic materials inspired by nature, with the morphology of resulting structures being adjustable by modifying freeze casting parameters.

The freeze casting process involves controlled solidification of a solution, suspension, sol, or gel, followed by sublimation of the solvent (typically water) under reduced pressure, and subsequent post-processing for densification [1, 2]. Controlled solidification induces phase separation as the solvent solidifies, with the solid phase (usually ice) serving as a template. Hence, freeze casting is also known as ice templating or ice formwork. Subsequently, the cured solvent template is sublimated, preserving the structural framework and yielding a well-defined monolith. A key advantage of freeze casting lies in its broad applicability to diverse materials, including nanoparticles, nanotubes, nanowires, nanofibers, nanosheets, polymer chains, and macromolecules, provided they are stably dispersed. Furthermore, varying processing conditions can lead to significant alterations in the micro- and macro-structure of freeze-cast scaffolds. Microstructural properties such as porosity and pore morphology (lamellar, honeycomb, radial, etc.) can be tailored using chemical and physical methods, while freeze casting enables the realization of different scaffold geometries at the macroscale. When combined with other processing techniques, freeze casting can achieve complex shaping routes [3].

2.1.2 Single-Particle Model

The exclusion of solid particles by the solidification front is crucial for freeze casting processes aimed at producing aligned or customized porous structures. Without this exclusion, the formation of an ice template would be hindered as the particles would be uniformly dispersed throughout the freezing system. Understanding the freeze casting process hinges on the thermodynamic free energy of the system, illustrated in Figure 2-1A [4] through a single particle model. During the solidification phase, the thermodynamic requirement for suspended "particles"

to be repelled by the solidification front is determined by the interface free energy, which must meet the following criteria:

$$\Delta\gamma_0 = \gamma_{ps} - (\gamma_{pl} + \gamma_{sl}) > 0 \text{ (1)}$$

where γ_{ps}, γ_{pl} and γ_{sl} are the interfacial free energies associated with the particle–solid, particle–liquid, and solid–liquid interfaces respectively. This energy balance facilitates the analysis of systems where suspended particles experience both repulsive, F_R, and attractive, F_A, forces with respect to the advancing freezing front arising due to interparticle van der Waals interactions at the liquid-solid interface and viscous drag, respectively.

$$F_R = 2\pi r \Delta\gamma_0 \left(\frac{\alpha_0}{d}\right)^n \text{ (2)}$$

$$F_A = \frac{6\pi\eta v r^2}{d} \text{ (3)}$$

where r is the radius of the solid particle, v is the freezing front velocity, α_0 is the mean distance between molecules in the liquid phase, d is the thickness of the liquid layer between the solid–liquid interface and the particle (i.e., the distance between the ice front and the particle), η is the dynamic viscosity of the liquid and n is an empirical correction factor for the repulsive forces that generally ranges from 1 to 4 [5].

Equating FR and FA and solving for the ice front velocity, v, results in an expression for the critical freezing front velocity, v_{cr}

$$v_{cr} = \frac{\Delta\gamma_0 d}{3\eta r}\left(\frac{a_0}{d}\right)^n \text{(4)}$$

As illustrated in Figure 2-1B–E, at very low solidification velocities ($v << v_{cr}$), the ice-growth proceeds as a planar front, displacing particles and increasing the solids loading of the unfrozen region. For $v < v_{cr}$, particles will generally be rejected and will form lamellar walls within the final freeze-cast scaffold and for $v \geqslant v_{cr}$, a certain fraction of particles will generally

be entrapped by the solid phase, creating bridges between lamellar walls, yielding fine-scale porosity throughout the resulting freeze cast structure [5]. Another freeze-cast structure occurs when particles are given insufficient time to segregate from the suspension, resulting in complete encapsulation of the particles within the ice front. This occurs when the freezing rates are rapid ($v >> v_{cr}$).

The equilibrium between forces, originating from the original FR and FA terms, is intricately tied to the characteristics of the liquid phase, solid particles, and their interactions with the advancing freezing front. As Equation 4 suggests, the entrapment or rejection of particles can be controlled through both chemical and physical means by altering the composition of the suspension (solvents, additives, solids) and adjusting freezing parameters (temperature, velocity, direction, external force fields). This manipulation leads to finely tailored pore morphologies and desired microstructural features.

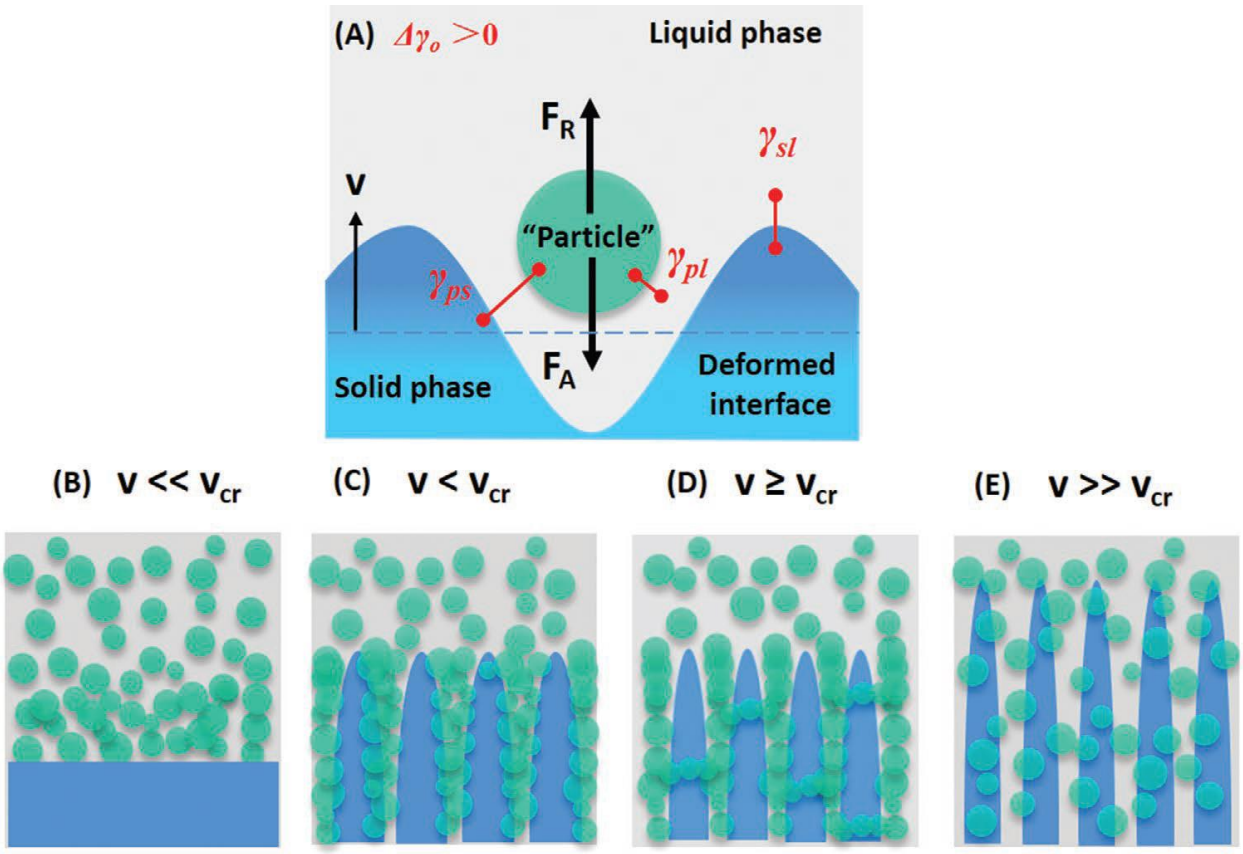

Figure 2-1 A) Illustration of the forces acting on a suspended particle in the vicinity of a freezing front. B–E) four cases of freezing front progression at different velocities.[4]

2.1.3 Multiple-Particle Model

Most mechanistic studies concerning structure formation in freeze casting primarily focus on the interaction between individual particles and the solidification front. However, to account for interactions among particles, single-particle analytical models can be extended to consider multiple particles by incorporating viscous friction within the compacted particle layer, a topic that recent research has addressed. The force acting on a particle near the solidification front can be decomposed into three components (refer to Figure 2-2A). Within the compacted particle layer, viscous friction within the particle matrix, along with the accompanying fluid pressure drop, results in an additional trapping force (FP) on particles. At the particle entry level into the

front, a "lubrication force" (FL) reduces the film thickness separating the particle and the front, consequently increasing the repelling thermomolecular force (FT) exerted by the front on particles [6].

The average velocities of the fluid, particles, and solid concerning the solidification front are denoted as Vf, Vs, and Vp, respectively [7]. The velocities of the suspension and frozen phase both match the solidification velocity but in opposite directions. However, within the compacted particle layer, their velocities differ due to the increasing particle volume fraction. This disparity leads to a thicker compacted layer until equilibrium is achieved. In a steady-state regime, particles become encapsulated as the interface advances, maintaining a constant thickness of the compact layer ahead of the interface.

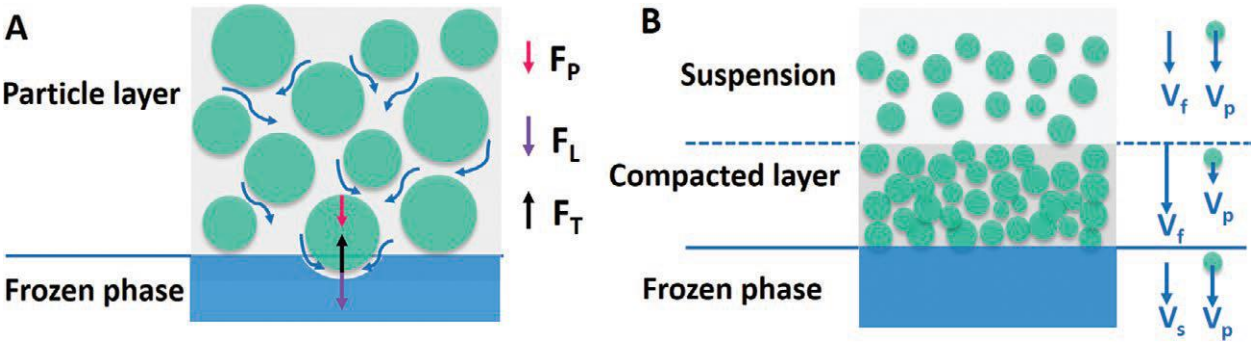

Figure 2-2 Forces acting on a particle entering the frozen phase. B) Cross section of the multiple-particle system: the suspension, the compacted layer of particles, and the frozen phase. [4]

2.1.4 Suspension Preparation

The successful formulation of precursor suspensions for freeze casting processes is a critical step involving solid components, suspension media, and additives, essential for achieving scaffold structures. The solid phase exists as suspended particles, acting as the building blocks in freeze-casting processes. Besides the characteristics of these building blocks, the inclusion of

solvents to modify freezing behavior and surfactants to adjust interparticle forces governs the resulting porous structure from freeze casting, as elucidated by the force balances in Equations 2 and 3. Similar to conventional suspensions, using dispersible particles is imperative, and achieving homogeneous dispersion of 1D and 2D building blocks often requires macromolecular or polymeric additives as dispersants and binders [8-14]. Freeze casting is applicable not only to particulate suspensions but also to colloidal sols and gels, attainable through surface grafting or functionalization akin to conventional sol-gel processing, to control open network formation [15, 16].

The pore characteristics of freeze-cast structures are significantly influenced by solvent chemistry. The four commonly used solvents in freeze casting—water, camphene, camphor-naphthalene, and tert-butyl alcohol—impart distinct lamellar, cellular, dendritic, and prismatic pore morphologies, respectively, owing to their different crystallization behaviors. Moreover, the formation of crystalline ice structures, including nucleation, growth, and recrystallization, is further regulated through ice structuring agents, typically in the form of alcohols or salts [17-20]. By controlling crystallization processes, freeze cast materials' final pore morphologies can be precisely tailored.

2.1.5 Solidification

In freeze-casting processes, various parameters such as solidification velocity, temperature, direction, and external force fields can be adjusted to influence the resulting microstructure of scaffolds. Modulating the freezing-front velocity and temperature gradient of solutions can alter the spacing and thickness of scaffold walls. Lower freezing temperatures induce higher undercooling and solidification velocity, leading to narrower pore channels and thinner walls in the final structure [21].

Different freezing techniques such as unidirectional freezing, bidirectional freezing, radial freezing, radial-concentric freezing, freezing under flow, dynamic freezing, random freezing, and freeze-thawing have been studied to control porosity and microstructure in freeze-cast scaffolds [22-32]. Conventional unidirectional freezing initiates ice nucleation randomly on a cold surface, resulting in microscale crystallites aligned along the freezing direction and small-scale lamellar structures. Bidirectional freezing, achieved through modified freeze-casting setups generating dual temperature gradients, produces large-size single-domain aligned lamellar structures from solid phase building blocks like ceramic particles, platelets, boron nitride nanosheets, or graphene sheets [22, 23, 33, 34].

Radial freeze casting, using a copper mold and subjected to two temperature gradients, creates longitudinally and radially aligned porosity [26, 27]. Inspired by capillary transport in trees, recent studies have used radial freeze casting to mimic cellular tracheid structures in conifers, producing biomimetic structures optimized for fluid transport efficiency [35].

In addition to controlling freeze cast structures through controlled thermal gradients, external fields such as magnetic [36-38], electric [39-41], acoustic [42], and light irradiation [43, 44] can further manipulate the chemical states of suspension media or solid particles in colloidal suspensions during or after solidification. Magnetic fields, created by permanent magnets arranged in various spatial orientations, can yield scaffolds with different microstructural patterns when used in freeze casting magnetic particles or other building blocks functionalized with magnetic nanoparticles. For instance, a continuous core-shell structure consisting of radially aligned lamellae and a core can form under a radial magnetic field. Applying an axial field parallel to the solidification direction leads to scaffolds with three banded regions of low-density and high-density core-shell architectures. Transverse magnetization results in scaffolds with two

primary structural features: lamellar walls and mineral bridges (Figure 2-3G,H), producing uniform architectures compared to gradient architectures formed under radial and axial magnetic fields. Recent studies in magnetic freeze casting have explored various magnets and positioning techniques, including rotating magnets, to control field strength and produce tailored freeze cast structures such as helical scaffolds, uniform scaffolds, and functionally graded materials.

An alternative approach involves applying an electric field to create a temperature gradient, thus controlling ice crystal growth paths. Perpendicular electric fields to the freezing direction lead to long-range alignment of lamellar walls through angled ice crystal formation (Figure 2-3I,J). Conversely, electric fields parallel to the solidification direction produce scaffolds with bilayered dense/porous regions. Utilizing a standing ultrasonic wave field (Figure 2-3K) generates standing pressure waves, creating regions of high and low pressure in freeze-casting processes. As particles migrate to low-pressure regions, resulting scaffolds exhibit alternating dense/porous rings (Figure 2-3L). A novel approach involves using light irradiation to drive reactions and rearrangements among polymeric building blocks in the frozen state [45, 46]. This incorporation of light-driven cross-linking into freeze-casting processes plays an increasingly crucial role in developing techniques for fabricating aligned porous polymers and polymer-based materials, as discussed in subsequent sections.

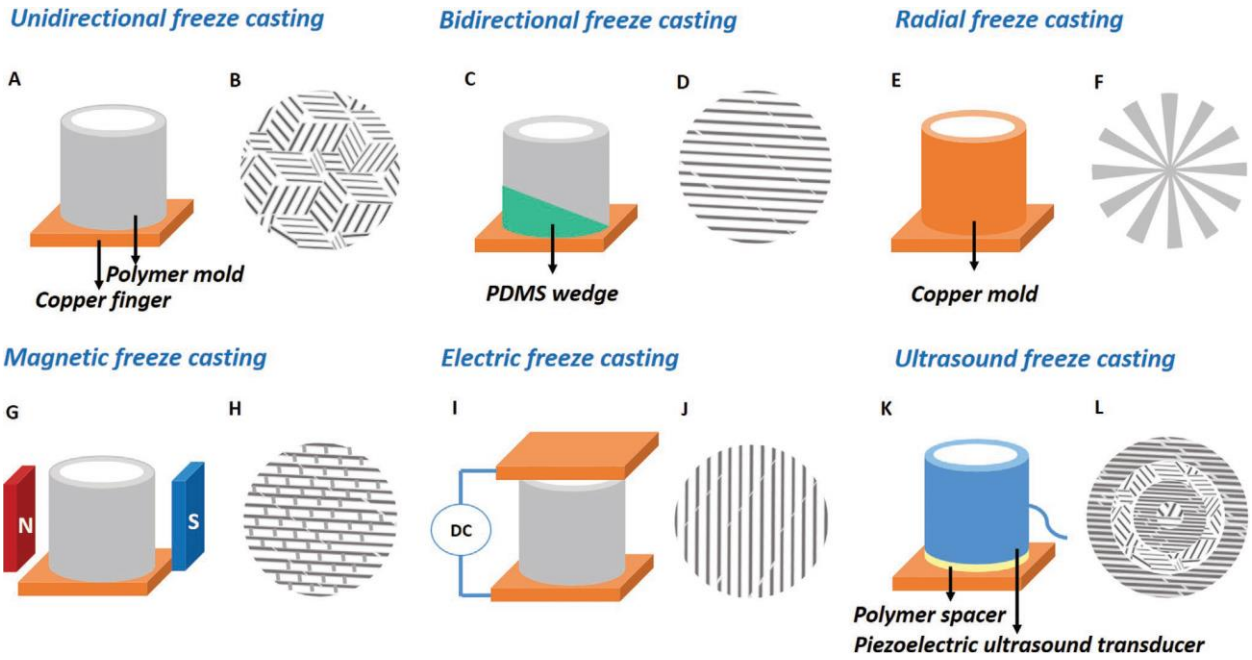

Figure 2-3 Schematics of freeze casting techniques and corresponding top-view microstructures of resulting scaffolds. A,B) unidirectional, C,D) bidirectional, E,F) radial, G,H) magnetic, I,J) electric and K,L) ultrasound freeze casting. [4]

2.1.6 Recrystallization

When a solvent remains frozen for an extended period, Ostwald ripening may occur, wherein large crystals grow at the expense of smaller ones, leading to an increase in mean crystal size and a decrease in the total number of crystals. The resulting grain size can be adjusted by adding ionic solutes and controlling freezing time and temperature [47]. This phenomenon of recrystallization can be leveraged as a templating approach for crafting various 2D and 3D porous materials using nanoparticles [20], Ag nanowires (AgNWs) [35], graphene oxide (GO) nanosheets [48], and polymers with customizable pore sizes.

2.1.7 Sublimation

Freeze drying (lyophilization) is the predominant method for sublimating the solidified solvent (suspension media) template after the solidification process. Freeze drying parameters have not been observed to significantly affect the final microstructure of freeze-cast samples. More recently, freeze substitution (rapid freezing followed by dissolution of solidified fluids) and supercritical drying have been employed to remove solidified solvents containing nonvolatile cryoprotectants like glycerol or ethylene glycol, which are not effectively removed by freeze-drying alone. This technique allows for the use of high cryoprotectant concentrations to manipulate pore forms, resulting in highly uniform, crack-free aerogels with a finer pore texture [49].

2.1.8 Post-treatment

To achieve desired structural and physical properties in aligned porous materials created by freeze-casting, post-treatment processes such as densification, pyrolysis, thermal reduction, and carbonization are employed on dried scaffolds. Densification processes are crucial for imparting adequate mechanical properties to porous scaffolds, especially those composed of ceramic or metallic building blocks. High-temperature sintering stands as the most common method for densification. This process involves the removal of binders and the sintering together of particles. Furthermore, in nanowire-based systems, high-temperature processes facilitate chemical bonding between glass binders and 1D building blocks [9, 10, 50].

In recent investigations of innovative freeze casting systems, high-temperature pyrolysis under inert atmospheres is utilized for the ceramization of freeze-cast preceramic polymer precursors. For freeze casting novel assembled graphene scaffolds, thermal reduction processes are employed to eliminate functional groups from graphene oxide units and reconstruct graphene

structures, thereby enhancing the electrical and mechanical properties of 3D graphene-based scaffolds [13, 51, 52]. Additionally, lightweight carbon materials can be derived from biomacromolecular-based scaffolds through the carbonization process [11, 34, 53-57].

2.1.9 Post-fabrication

Infiltrating freeze-cast skeletons with a secondary phase enables the fabrication of aligned composites, hydrogels, and nacre-mimetic hybrids. While not intrinsic to the freeze casting process, post-fabrication infiltration adds new functionalities to freeze-cast structures and expands the scope of systems achievable through this synthesis method. Various infiltration techniques have been established, including polymer/metal melt immersion [1, 58, 59], in situ polymerization [33, 60-62], and deposition methods such as chemical/physical vapor deposition [63], electrochemical deposition [64], and atomic layer deposition [65].

By controlling suspension components and subsequent processing, as discussed earlier, freeze casting proves to be a versatile and cost-effective approach to materials fabrication. It can be adapted to a wide range of material combinations involving different building blocks and provides valuable avenues for developing high-performance materials for applications in energy dissipation, storage and conversion, environmental remediation, thermal insulation, and biological applications.

2.2 Review of the Direct Ink Writing (DIW) - An Extrusion-based 3D Printing Technique

2.2.1 Introduction of Direct Ink Writing (DIW)

Additive Manufacturing (AM) represents one of the latest manufacturing strategies with the potential not only to surpass traditional manufacturing limitations in efficiency and design but also to drive the next generation of cultural and technological development [66]. One of the

unique strengths of AM is its design freedom, which can propel advancements in biology, chemistry, materials science, and physics. Within AM, researchers have explored various printing techniques that enable the rapid and precise fabrication of materials across customizable build volumes. Among these techniques, DIW has emerged as a highly versatile AM method capable of utilizing a wide range of materials to create complex and/or periodic 3D structures.

DIW operates as an extrusion-based AM technique that allows for the creation of intricate architectures and compositions at the meso- and microscale. During this process, a viscoelastic ink material is extruded through a deposition nozzle layer by layer to construct scaffolds and other 3D geometries on a computer-controlled translational stage [67]. Upon extrusion, the 3D construct solidifies, yielding a structure with desired features and properties [68]. DIW, also known as Robocasting, can generally be categorized into two classes: droplet and continuous ink extrusion. The cost-effectiveness, simplicity, and ability to blend different materials in a single processing step in DIW have attracted numerous research organizations and universities worldwide to engage in cutting-edge developments using this technique.

First patented by Cesarano and Calvert at Sandia National Laboratory in 1997, DIW initially gained recognition as a method for fabricating complex ceramic structures. Since then, its utilization has expanded globally across a multitude of fields beyond structural ceramics. The body of literature on DIW has also experienced exponential growth since 2006, with significant engineering and scientific contributions originating from diverse disciplines.

DIW stands out among other Additive Manufacturing (AM) technologies due to its versatility across material classes, provided the precursor ink exhibits appropriate rheological behavior such as apparent viscosity, yield stress under shear and compression, and viscoelastic properties (i.e., loss and elastic moduli) [70]. This flexibility allows virtually any ink to be

printed effectively as a 3D structure with high-resolution patterning, architectural freedom, and intended material properties. In contrast, other AM technologies like fused filament fabrication (FFF), digital light processing (DLP), stereolithography (SLA), and powder bed fusion (PBF) are more limited in terms of printable materials. For example, FFF excels in printing thermoplastic polymers, while DLP and SLA are suitable primarily for photopolymer resins, and PBF is mostly used for metals, alloys, ceramics, and some thermoplastic polymers.

DIW's versatility is further highlighted by its unique ability to create novel multimaterial structures through separate and simultaneous extrusion of different ink materials [71]. This capability streamlines manufacturing processes by achieving multimaterial structures in a single step, reducing overall time, energy consumption, cost, and waste generation while preserving critical material properties. Additionally, DIW offers promising avenues for 4D printing, enabling the development of shape-changing smart materials responsive to external stimuli [72, 73].

As a manufacturing process, DIW is highly customizable, allowing easy modification of the print setup using interchangeable low-cost components such as the three-axis platform, computer, and dispenser. Moreover, incorporating external stimuli like magnetic fields [74], electromagnetic waves [75], acoustic waves [76], and cooling sources [77] enables the fabrication of 3D structures with controlled microstructures. This versatility has spurred extensive research into DIW across various material domains, including polymers [78-81], metals [82-84], ceramics [77, 85-87], and living materials [88-90], tailoring their mechanical, electrical, thermal, chemical, and biological properties.

The breadth of DIW's potential is evident in its applications across a wide range of fields, including biomedical devices [91], artificial organs [92], tissue engineering [93], energy storage

platforms [94], optoelectronic components [95], metamaterials [96], soft robotics [97], electronics [98], sensors [99], and even food printing [100]. While primarily used in research labs for small-scale fabrication and prototyping, DIW holds promise for rapid and straightforward fabrication of industrial-level prototypes. With ongoing development and versatility, DIW is poised to expand its impact and adoption across various industries in the future.

2.2.2 Rheology of Inks

The foundational capability of DIW to create self-supporting extruded layers directly stems from the printability and shape fidelity of the ink [101]. In essence, an ink is deemed printable if it can be extruded as a continuous filament through a specific nozzle, accurately translating the digital model into physical structures. Shape fidelity of the ink refers to its ability to maintain the intended morphology after deposition, drying, and subsequent post-processing steps [102]. Moreover, the ink must exhibit smooth flow without discontinuities or particle jamming that could lead to nozzle clogging. Rheologically, the ink should demonstrate shear-thinning behavior across varying flow rates, where its viscosity decreases with increasing shear rate. This property facilitates ink flow through nozzles even at lower extrusion pressures, ensuring extrudability. Typically, DIW inks possess viscosities ranging between 10^2 and 10^6 mPa·s at a shear rate of approximately 0.1 s^{-1}, ensuring their printability.

The DIW deposition process can be delineated into three distinct steps (Fig. 2-4): (1) ink flow through the syringe barrel and printing nozzle, (2) ink ejection from the nozzle, and (3) ink deposition onto the underlying printed layers. Each of these steps demands specific ink characteristics to maintain printability. It is crucial to note that the concept of printability is not

universally applicable and is intricately tied to the intended use and application of the printed object [103].

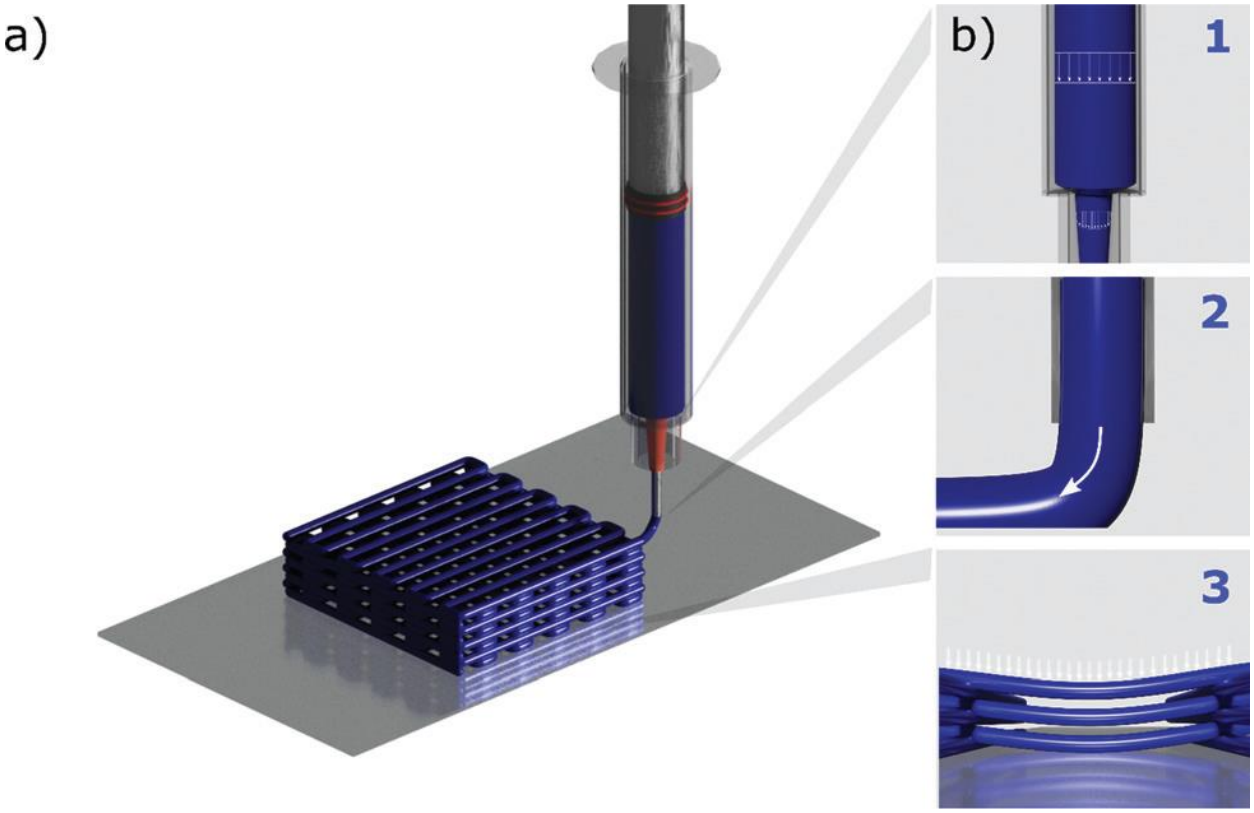

Figure 2-4(a and b) Schematic showing the main steps of the printing process: flow of the ink inside the syringe barrel and nozzle (1), ejection of the ink from the nozzle (2) and deposition onto the substrate to form a self-standing structure (3) [94].

After being discharged from the printing head, the ink must promptly transition from a shear-thinning fluid to a solid-like substance to preserve its shape fidelity. An essential metric for evaluating the ink's ability to maintain this fidelity is the ratio of loss modulus (G″) to storage modulus (G′). Figure 2-5 illustrates the ideal rheological response of a printable ink during DIW, showcasing different shear stress levels experienced by the ink during extrusion through the micronozzle, depicted with varying colors. Inside the nozzle (Region 1), the shear stress

exceeds the yield stress, causing the material to yield and flow. Outside the nozzle (Region 2), stress dissipates, and the material transitions to a viscoelastic solid state. Subsequently, once the deposition process concludes, the printed structure must retain its shape until fully solidified.

Maintaining appropriate rheological properties after printing is crucial to prevent stacked filaments from sagging under their weight and to minimize bending in spanning parts. Achieving this entails ensuring that the storage modulus (G') remains higher than the loss modulus (G'') of the suspended ink. Additionally, for DIW inks, it is vital for G' to remain relatively constant over low shear stress levels, as depicted in Figure 2-5, representing the linear viscoelastic region (LVR). Further insights into ink behavior during the writing process can be gained by optimizing two yield stress parameters: σ_1, indicating the onset of deviation of G'

from the LVR, and σ 2, marking the transition from solid-like to liquid-like behavior (crossover of G′ and G′′) [104].

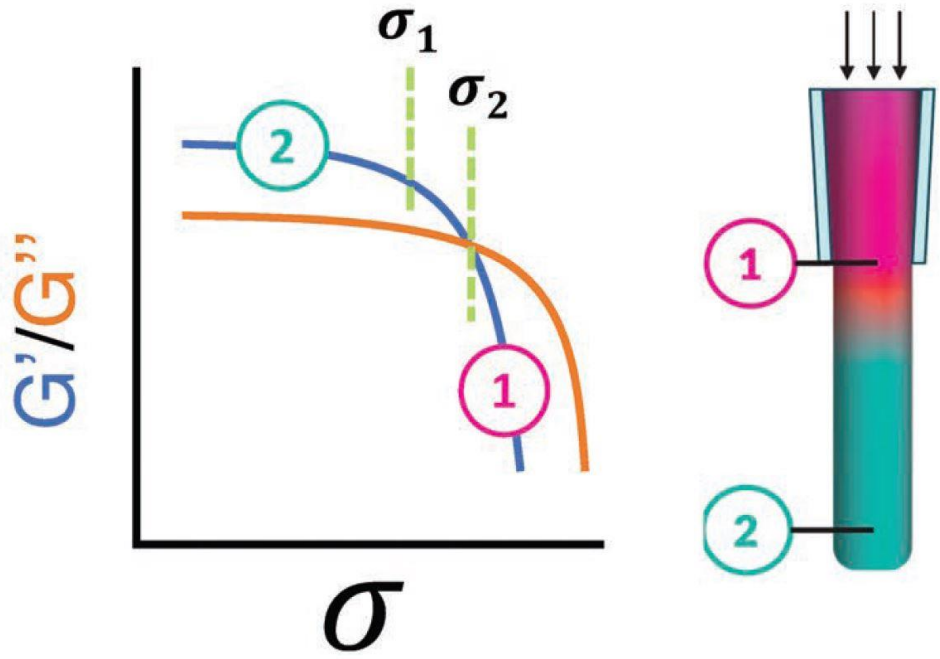

Figure 2-5 Schematic showing the ideal rheological response (storage modulus (G′)/loss modulus (G″) vs shear rate (σ)) of a printable ink and pressure-induced flow for a conventional ink that has bulk non-Newtonian properties [104].

Several mathematical models have been developed to quantify the printability and shape fidelity parameters. The power law viscosity model is generally used to represent the nonlinear relationship between shear stress and viscosity and is described by,

$$\eta = K\dot{\gamma}^{n-1} \quad (1)$$

where η is the viscosity, K is the flow consistency index, $\dot{\gamma}$ is the shear rate, and n is the power law index. For shear-thinning fluids, n fits the following parameter, $0 < n < 1$, while for shear-thickening, $n > 1$.

However, when yield stress is also considered, the power law is adapted with an additional term and mathematically represented by the Herschel-Bulkley (HB) model. Hence the flow behavior of ink for DIW is usually described using this model given by,

$$\tau = \tau_y + K\dot{\gamma}^n \quad (2)$$

where τ is the shear stress and as described previously, K is the flow consistency index, $\dot{\gamma}$ is the shear rate, and n is the flow index[102]. It is required that the shear stress applied by the nozzle must exceed the yield shear stress so that the ink acts as a fluid and flows easily. Furthermore, when the shear stresses in the form of $(\tau - \tau_y)$ are plotted with respect to the estimated shear rates on a log–log graph, the values of n and K from the HB model can be determined. These values distinguish and optimize ink compositions based on their shear-thinning capability and viscosity and thus help to determine the ideal ink for DIW [105].

Ideally, the ink's characteristics should be solely determined by the shear rate, such that its structural integrity can be quickly restored when it stops flowing. However, for thixotropic materials, ink characteristics are affected by shear history and shear rate [103]. For these materials, the HB model can be modified to the following:

$$\tau = K|\dot{\gamma}|^n t^{-m} + \tau_0 \quad (3)$$

where t is shearing time and m is a dimensionless thixotropic index. However, the accuracy of this equation is limited when estimating large values of time and when considering the recovery of the ink's viscosity once shear stress is removed [106].

The maximum shear stress rate and the shear stress can also be estimated. For example, the maximum shear stress rate can be approximated by,

$$\dot{\gamma}_{max} = \frac{4\dot{Q}}{\pi r^3} \quad (4)$$

where r is the nozzle radius and Q is the volumetric flow rate, calculated as $Q = Sr^2$, with S as the printing speed [97]. And estimation of the shear stress (τ), assuming radial nozzle, is obtained through the following calculation:

$$\tau = \frac{\Delta P}{2L} r \quad (5)$$

where ΔP is the pressure applied at the nozzle, r is the radial position from the center to the edge of the nozzle, and L is the nozzle length [107].

A mathematical relationship had also been proposed to calculate the minimum yield stress required to avoid sagging due to self-weight and capillary forces. M'Barki et al [101] expressed it as:

$$\sigma_y^{dyn} \geq \gamma R^{-1} + \rho g h \quad (6)$$

where σ_y^{dyn} is the dynamic yield stress, γ is the suspension surface tension, R is the nozzle diameter, and ρgh denotes the self-weight of the material.

Smay et al. [70] applied elastic beam theory on spanning ink filaments to calculate the minimum storage modulus required to mitigate deflection:

$$G' \geq 1.4\gamma \left(\frac{L}{D}\right)^4 D \quad (7)$$

where, γ is the ink's specific weight, L is the length of the spanning element, and D is its diameter. The ink's Poisson ratio was assumed to be 0.5 (incompressible).

It is crucial to recognize that while mathematically derived models exist, they do not provide absolute solutions and pose challenges in establishing a universal rheological model for DIW. Consequently, the rheological properties of ink are typically evaluated experimentally using a rotational rheometer. Common rheological tests such as flow ramps are utilized to assess the extent of shear-thinning behavior in inks, while oscillatory tests offer insights into their viscoelastic properties. Furthermore, extensional rheology and three-interval thixotropy tests are

conducted to evaluate ink printability [103]. The determination of yield stress often stems from oscillatory tests, identifying the stress level at which the storage modulus equals the loss modulus (crossover point).

These empirically derived physical parameters can be fine-tuned through modifications in material chemistry (e.g., advanced polymer design) or the incorporation of plasticizers and/or rheology modifiers (e.g., silica) in ink formulations. Given that DIW printability and shape fidelity hinge significantly on these parameters, their accurate determination and control are crucial for the successful execution of any DIW process.

2.2.3 Rheological characterization

The rheological properties of inks for DIW are typically evaluated using a rotational rheometer, as depicted in Figure 2-6 [108]. Shear rheology is commonly assessed through flow ramps, providing insights into the degree of shear thinning exhibited by inks [70]. Oscillatory tests, on the other hand, offer information about the viscoelastic properties of inks at rest [109]. Yield stress determination, crucial in publications on printed energy materials, is often derived from oscillatory tests, where the stress level at which the storage modulus equals the loss modulus is identified [110, 111]. Although this method is considered quick and reliable, it tends to yield higher values compared to Herschel–Bulkley fitting, primarily because the yielding process and subsequent departure from linear response begin when the storage modulus equals the loss modulus [112]. Furthermore, the crossover between G' and G" occurs outside the linear region, with the viscoelastic moduli representing only the fundamental harmonic of the oscillatory response [108].

Corker et al. [103] introduced two distinct characteristic stress values in the oscillatory response of GO pastes: the yield stress and the flow stress. Their ratio provides insights into ink brittleness and relates to ink printability. Three-interval thixotropy tests (3ITT) offer a straightforward method to study ink thixotropy [94]. During these tests, the ink undergoes low-stress shearing initially to stabilize its microstructure. Subsequently, a high-stress interval disrupts the ink's microstructure, simulating flow inside the nozzle. Finally, a low shear stress is applied again, measuring the material's recovery kinetics.

Extensional rheology has also been employed to assess printability, although such tests are more complex than shear rheology for yield stress fluids [103]. For instance, in capillary break-up extensional tests, yield-stress fluids do not form cylindrical filaments, and filament thinning heavily depends on the initial deformation applied to the material [114, 115].

.

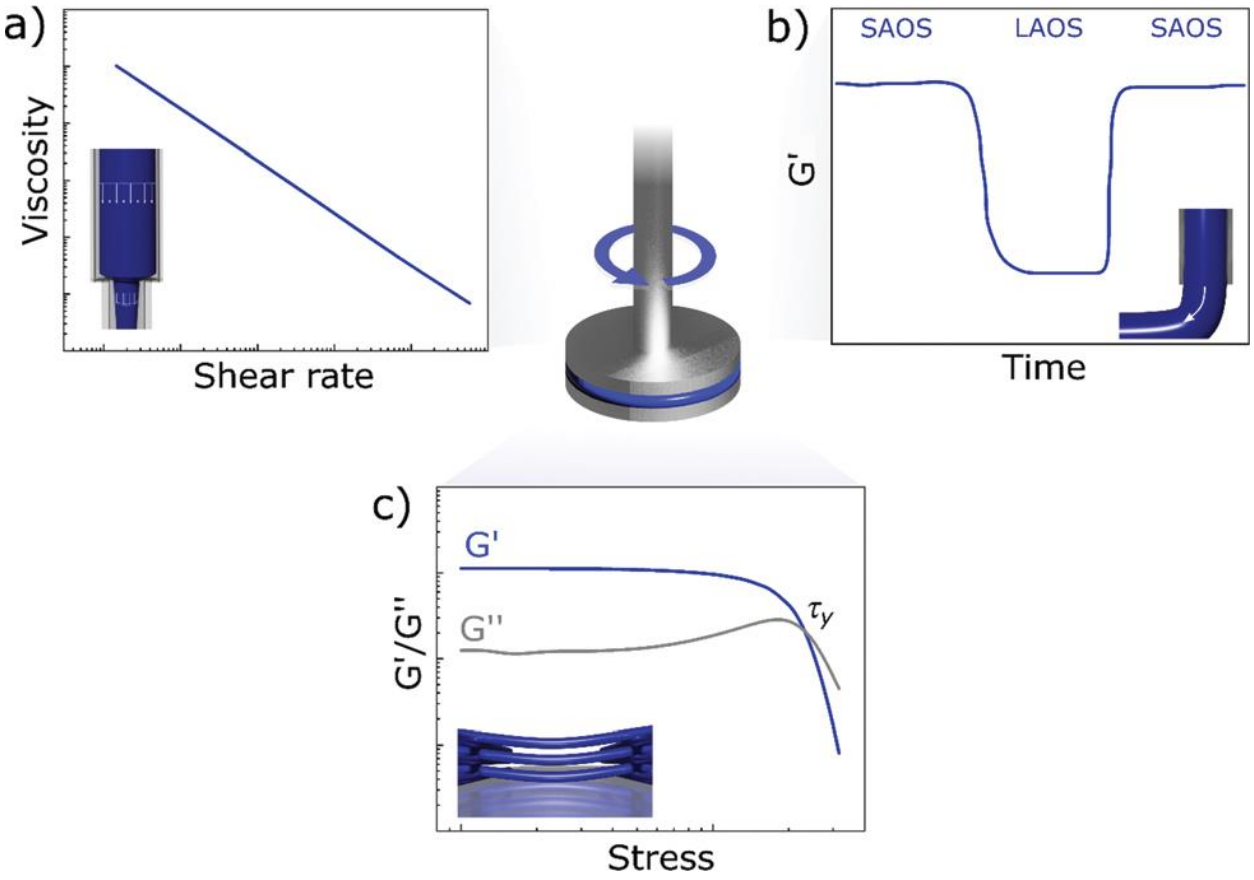

Figure 2-6 Schematic showing the ideal rheological response of a printable ink, as determined through shear rheology: (a) flow curve showing a highly shear-thinning behavior; (b) rapid recovery of the elastic modulus during 3ITT tests, after large amplitude oscillatory shear (LAOS); (c) solid-like behavior below the yield stress [94].

Summary

Freeze casting and direct ink writing are the foundational components of the extrusion-based 3D freeze printing (3DFP) method, each with its own set of advantages and limitations. While freeze casting offers effective control over the microstructure of aerogels, the macrostructure heavily depends on the mold geometry, leading to limitations in the achievable structures, mechanical properties, and applications of these aerogels. On the other hand, direct

ink writing allows for customization of aerogel geometries and controlled microstructures, combining the strengths of additive manufacturing techniques with freeze casting.

The integration of freeze casting and additive manufacturing in 3DFP represents a significant advancement, enabling the fabrication of aerogels with tailored geometries and microstructures. However, there are ongoing challenges that must be addressed to fully realize the potential of 3DFP in aerogel fabrication. The forthcoming chapters will delve into our fundamental exploration of the extrusion-based 3DFP method using advanced X-ray synchrotron radiography techniques. Additionally, we will introduce new materials and advanced applications for 3DFP aerogels, unlocking their full capabilities in this domain. These advancements mark an exciting new phase in aerogel research and application, promising novel solutions and opportunities across various industries.

References

[1] S. Deville, E. Saiz, R.K. Nalla, A.P. Tomsia, Freezing as a path to build complex composites, Science 311(5760) (2006) 515-518.

[2] H. Zhang, I. Hussain, M. BRUST, MF BUTLER, SP RANNARD, AND AI COOPER," Aligned two-and three-dimensional structures by directional freezing of polymers and nanoparticles." Nature Materials 4(10) (2005) 787-93.

[3] S. Deville, The lure of ice-templating: Recent trends and opportunities for porous materials, Scripta Materialia 147 (2018) 119-124.

[4] G. Shao, D.A. Hanaor, X. Shen, A. Gurlo, Freeze casting: from low‐dimensional building blocks to aligned porous structures—a review of novel materials, methods, and applications, Advanced Materials 32(17) (2020) 1907176.

[5] U. Wegst, M. Schecter, A. Donius, P. Hunger, Philos. Trans. R. Soc. A-Math Phys, Eng. Sci. 368 (2010) 2099.

[6] B. Saint-Michel, M. Georgelin, S. Deville, A. Pocheau, Interaction of multiple particles with a solidification front: From compacted particle layer to particle trapping, Langmuir 33(23) (2017) 5617-5627.

[7] B. Saint-Michel, M. Georgelin, S. Deville, A. Pocheau, Boundary-induced inhomogeneity of particle layers in the solidification of suspensions, Physical Review E 99(5) (2019) 052601.

[8] M.C. Gutiérrez, M.J. Hortigüela, J.M. Amarilla, R. Jiménez, M.L. Ferrer, F. Del Monte, Macroporous 3D architectures of self-assembled MWCNT surface decorated with Pt nanoparticles as anodes for a direct methanol fuel cell, The Journal of Physical Chemistry C 111(15) (2007) 5557-5560.

[9] C. Ferraro, E. Garcia‐Tuñon, V.G. Rocha, S. Barg, M.D. Fariñas, T.E.G. Alvarez‐Arenas, G. Sernicola, F. Giuliani, E. Saiz, Light and strong SiC networks, Advanced Functional Materials 26(10) (2016) 1636-1645.

[10] F. Qian, P.C. Lan, M.C. Freyman, W. Chen, T. Kou, T.Y. Olson, C. Zhu, M.A. Worsley, E.B. Duoss, C.M. Spadaccini, Ultralight conductive silver nanowire aerogels, Nano letters 17(12) (2017) 7171-7176.

[11] Y. Hu, H. Zhuo, Q. Luo, Y. Wu, R. Wen, Z. Chen, L. Liu, L. Zhong, X. Peng, R. Sun, Biomass polymer-assisted fabrication of aerogels from MXenes with ultrahigh compression elasticity and pressure sensitivity, Journal of Materials Chemistry A 7(17) (2019) 10273-10281.

[12] H.E. Romeo, C.E. Hoppe, M.A. Lopez-Quintela, R.J. Williams, Y. Minaberry, M. Jobbágy, Directional freezing of liquid crystalline systems: from silver nanowire/PVA aqueous dispersions to highly ordered and electrically conductive macroporous scaffolds, Journal of Materials Chemistry 22(18) (2012) 9195-9201.

[13] S. Barg, F.M. Perez, N. Ni, P. do Vale Pereira, R.C. Maher, E. Garcia-Tunon, S. Eslava, S. Agnoli, C. Mattevi, E. Saiz, Mesoscale assembly of chemically modified graphene into complex cellular networks, Nature Communications 5(1) (2014) 1-10.

[14] M. Yang, N. Zhao, Y. Cui, W. Gao, Q. Zhao, C. Gao, H. Bai, T. Xie, Biomimetic architectured graphene aerogel with exceptional strength and resilience, ACS nano 11(7) (2017) 6817-6824.

[15] Z.-Z. Pan, H. Nishihara, S. Iwamura, T. Sekiguchi, A. Sato, A. Isogai, F. Kang, T. Kyotani, Q.-H. Yang, Cellulose nanofiber as a distinct structure-directing agent for xylem-like microhoneycomb monoliths by unidirectional freeze-drying, ACS nano 10(12) (2016) 10689-10697.

[16] M. Han, X. Yin, K. Hantanasirisakul, X. Li, A. Iqbal, C.B. Hatter, B. Anasori, C.M. Koo, T. Torita, Y. Soda, Anisotropic MXene aerogels with a mechanically tunable ratio of electromagnetic wave reflection to absorption, Advanced Optical Materials 7(10) (2019) 1900267.

[17] S. Deville, C. Viazzi, C. Guizard, Ice-structuring mechanism for zirconium acetate, Langmuir 28(42) (2012) 14892-14898.

[18] S. Wu, L. Li, H. Xue, K. Liu, Q. Fan, G. Bai, J. Wang, Size controllable, transparent, and flexible 2D silver meshes using recrystallized ice crystals as templates, ACS nano 11(10) (2017) 9898-9905.

[19] P. Zhang, J. Li, L. Lv, Y. Zhao, L. Qu, Vertically aligned graphene sheets membrane for highly efficient solar thermal generation of clean water, ACS nano 11(5) (2017) 5087-5093.

[20] S. Wu, C. Zhu, Z. He, H. Xue, Q. Fan, Y. Song, J.S. Francisco, X.C. Zeng, J. Wang, Ion-specific ice recrystallization provides a facile approach for the fabrication of porous materials, Nature communications 8(1) (2017) 1-8.

[21] A. Bahrami, U. Simon, N. Soltani, S. Zavareh, J. Schmidt, M.I. Pech-Canul, A. Gurlo, Eco-fabrication of hierarchical porous silica monoliths by ice-templating of rice husk ash, Green Chemistry 19(1) (2017) 188-195.

[22] H. Bai, Y. Chen, B. Delattre, A.P. Tomsia, R.O. Ritchie, Bioinspired large-scale aligned porous materials assembled with dual temperature gradients, Science advances 1(11) (2015) e1500849.

[23] J. Han, G. Du, W. Gao, H. Bai, An anisotropically high thermal conductive boron nitride/epoxy composite based on nacre‐mimetic 3D network, Advanced Functional Materials 29(13) (2019) 1900412.

[24] P. Niksiar, F.Y. Su, M.B. Frank, T.A. Ogden, S.E. Naleway, M.A. Meyers, J. McKittrick, M.M. Porter, External field assisted freeze casting, Ceramics 2(1) (2019) 208-234.

[25] K. Yin, P. Divakar, U.G. Wegst, Plant-derived nanocellulose as structural and mechanical reinforcement of freeze-cast chitosan scaffolds for biomedical applications, Biomacromolecules 20(10) (2019) 3733-3745.

[26] L. Fan, J.-L. Li, Z. Cai, X. Wang, Creating biomimetic anisotropic architectures with co-aligned nanofibers and macrochannels by manipulating ice crystallization, ACS nano 12(6) (2018) 5780-5790.

[27] C. Wang, X. Chen, B. Wang, M. Huang, B. Wang, Y. Jiang, R.S. Ruoff, Freeze-casting produces a graphene oxide aerogel with a radial and centrosymmetric structure, ACS nano 12(6) (2018) 5816-5825.

[28] F.Y. Su, J.R. Mok, J. McKittrick, Radial-concentric freeze casting inspired by porcupine fish spines, Ceramics 2(1) (2019) 15.

[29] F. Bouville, E. Maire, S. Meille, B. Van de Moortèle, A.J. Stevenson, S. Deville, Strong, tough and stiff bioinspired ceramics from brittle constituents, Nature materials 13(5) (2014) 508-514.

[30] H.-D. Jung, S.-W. Yook, T.-S. Jang, Y. Li, H.-E. Kim, Y.-H. Koh, Dynamic freeze casting for the production of porous titanium (Ti) scaffolds, Materials Science and Engineering: C 33(1) (2013) 59-63.

[31] Y. Tang, K.L. Yeo, Y. Chen, L.W. Yap, W. Xiong, W. Cheng, Ultralow-density copper nanowire aerogel monoliths with tunable mechanical and electrical properties, Journal of Materials Chemistry A 1(23) (2013) 6723-6726.

[32] L. Lewis, S.G. Hatzikiriakos, W.Y. Hamad, M.J. MacLachlan, Freeze–thaw gelation of cellulose nanocrystals, ACS Macro Letters 8(5) (2019) 486-491.

[33] G. Du, A. Mao, J. Yu, J. Hou, N. Zhao, J. Han, Q. Zhao, W. Gao, T. Xie, H. Bai, Nacre-mimetic composite with intrinsic self-healing and shape-programming capability, Nature communications 10(1) (2019) 1-8.

[34] H.-L. Gao, Y.-B. Zhu, L.-B. Mao, F.-C. Wang, X.-S. Luo, Y.-Y. Liu, Y. Lu, Z. Pan, J. Ge, W. Shen, Super-elastic and fatigue resistant carbon material with lamellar multi-arch microstructure, Nature communications 7(1) (2016) 1-8.

[35] W. Xu, Y. Xing, J. Liu, H. Wu, Y. Cui, D. Li, D. Guo, C. Li, A. Liu, H. Bai, Efficient water transport and solar steam generation via radially, hierarchically structured aerogels, ACS nano 13(7) (2019) 7930-7938.

[36] M.M. Porter, P. Niksiar, J. McKittrick, Microstructural control of colloidal‐based ceramics by directional solidification under weak magnetic fields, Journal of the American Ceramic Society 99(6) (2016) 1917-1926.

[37] M.M. Porter, M. Yeh, J. Strawson, T. Goehring, S. Lujan, P. Siripasopsotorn, M.A. Meyers, J. McKittrick, Magnetic freeze casting inspired by nature, Materials Science and Engineering: A 556 (2012) 741-750.

[38] I. Nelson, L. Gardner, K. Carlson, S.E. Naleway, Freeze casting of iron oxide subject to a tri-axial nested Helmholtz-coils driven uniform magnetic field for tailored porous scaffolds, Acta Materialia 173 (2019) 106-116.

[39] Y. Tang, S. Qiu, Q. Miao, C. Wu, Fabrication of lamellar porous alumina with axisymmetric structure by directional solidification with applied electric and magnetic fields, Journal of the European Ceramic Society 36(5) (2016) 1233-1240.

[40] Y. Zhang, L. Hu, J. Han, Preparation of a dense/porous bilayered ceramic by applying an electric field during freeze casting, Journal of the American Ceramic Society 92(8) (2009) 1874-1876.

[41] Y. Tang, K. Zhao, J. Wei, Y. Qin, Fabrication of aligned lamellar porous alumina using directional solidification of aqueous slurries with an applied electrostatic field, Journal of the European Ceramic Society 30(9) (2010) 1963-1965.

[42] T.A. Ogden, M. Prisbrey, I. Nelson, B. Raeymaekers, S.E. Naleway, Ultrasound freeze casting: Fabricating bioinspired porous scaffolds through combining freeze casting and ultrasound directed self-assembly, Materials & Design 164 (2019) 107561.

[43] R. Obmann, S. Schörpf, C. Gorsche, R. Liska, T. Fey, T. Konegger, Porous polysilazane-derived ceramic structures generated through photopolymerization-assisted solidification templating, Journal of the European Ceramic Society 39(4) (2019) 838-845.

[44] M. Barrow, H. Zhang, Aligned porous stimuli-responsive hydrogels via directional freezing and frozen UV initiated polymerization, Soft Matter 9(9) (2013) 2723-2729.

[45] D. Chen, Y. Zhang, C. Ni, C. Ma, J. Yin, H. Bai, Y. Luo, F. Huang, T. Xie, Q. Zhao, Drilling by light: Ice-templated photo-patterning enabled by a dynamically crosslinked hydrogel, Materials Horizons 6(5) (2019) 1013-1019.

[46] W.F. Schroeder, R.J. Williams, C.E. Hoppe, H.E. Romeo, Unidirectional freezing as a tool for tailoring air permeability in macroporous poly (ethylene glycol)-based cross-linked networks, Journal of Materials Science 52(23) (2017) 13669-13680.

[47] Z. He, K. Liu, J. Wang, Bioinspired materials for controlling ice nucleation, growth, and recrystallization, Accounts of chemical research 51(5) (2018) 1082-1091.

[48] H. Geng, X. Liu, G. Shi, G. Bai, J. Ma, J. Chen, Z. Wu, Y. Song, H. Fang, J. Wang, Graphene oxide restricts growth and recrystallization of ice crystals, Angewandte Chemie 129(4) (2017) 1017-1021.

[49] T.M. Fears, J.A. Hammons, J.D. Sain, M.H. Nielsen, T. Braun, S.O. Kucheyev, Ultra-low-density silver aerogels via freeze-substitution, APL Materials 6(9) (2018) 091103.

[50] Y. Si, X. Wang, L. Dou, J. Yu, B. Ding, Ultralight and fire-resistant ceramic nanofibrous aerogels with temperature-invariant superelasticity, Science advances 4(4) (2018) eaas8925.

[51] O.T. Picot, V.G. Rocha, C. Ferraro, N. Ni, E. D'elia, S. Meille, J. Chevalier, T. Saunders, T. Peijs, M.J. Reece, Using graphene networks to build bioinspired self-monitoring ceramics, Nature communications 8(1) (2017) 1-11.

[52] F. An, X. Li, P. Min, P. Liu, Z.-G. Jiang, Z.-Z. Yu, Vertically aligned high-quality graphene foams for anisotropically conductive polymer composites with ultrahigh through-plane thermal conductivities, ACS applied materials & interfaces 10(20) (2018) 17383-17392.

[53] Y. Si, X. Wang, C. Yan, L. Yang, J. Yu, B. Ding, Ultralight biomass‐derived carbonaceous nanofibrous aerogels with superelasticity and high pressure‐sensitivity, Advanced materials 28(43) (2016) 9512-9518.

[54] C. Li, Z.Y. Wu, H.W. Liang, J.F. Chen, S.H. Yu, Ultralight Multifunctional Carbon‐Based Aerogels by Combining Graphene Oxide and Bacterial Cellulose, Small 13(25) (2017) 1700453.

[55] Z. Zeng, C. Wang, Y. Zhang, P. Wang, S.I. Seyed Shahabadi, Y. Pei, M. Chen, X. Lu, Ultralight and highly elastic graphene/lignin-derived carbon nanocomposite aerogels with ultrahigh electromagnetic interference shielding performance, ACS applied materials & interfaces 10(9) (2018) 8205-8213.

[56] Z. Zeng, Y. Zhang, X.Y.D. Ma, S.I.S. Shahabadi, B. Che, P. Wang, X. Lu, Biomass-based honeycomb-like architectures for preparation of robust carbon foams with high electromagnetic interference shielding performance, Carbon 140 (2018) 227-236.

[57] Z. Zeng, X.Y.D. Ma, Y. Zhang, Z. Wang, B.F. Ng, M.P. Wan, X. Lu, Robust lignin-based aerogel filters: High-efficiency capture of ultrafine airborne particulates and the mechanism, ACS Sustainable Chemistry & Engineering 7(7) (2019) 6959-6968.

[58] Y. Yao, J. Sun, X. Zeng, R. Sun, J.B. Xu, C.P. Wong, Construction of 3D skeleton for polymer composites achieving a high thermal conductivity, Small 14(13) (2018) 1704044.

[59] A. Wat, J.I. Lee, C.W. Ryu, B. Gludovatz, J. Kim, A.P. Tomsia, T. Ishikawa, J. Schmitz, A. Meyer, M. Alfreider, Bioinspired nacre-like alumina with a bulk-metallic glass-forming alloy as a compliant phase, Nature communications 10(1) (2019) 1-12.

[60] E. D'Elia, S. Barg, N. Ni, V.G. Rocha, E. Saiz, Self‐healing graphene‐based composites with sensing capabilities, Advanced Materials 27(32) (2015) 4788-4794.

[61] H. Bai, F. Walsh, B. Gludovatz, B. Delattre, C. Huang, Y. Chen, A.P. Tomsia, R.O. Ritchie, Bioinspired hydroxyapatite/poly (methyl methacrylate) composite with a nacre‐mimetic architecture by a bidirectional freezing method, Advanced Materials 28(1) (2016) 50-56.

[62] E. Munch, M.E. Launey, D.H. Alsem, E. Saiz, A.P. Tomsia, R.O. Ritchie, Tough, bio-inspired hybrid materials, Science 322(5907) (2008) 1516-1520.

[63] P. Gannon, S. Sofie, M. Deibert, R. Smith, V. Gorokhovsky, Thin film YSZ coatings on functionally graded freeze cast NiO/YSZ SOFC anode supports, Journal of applied electrochemistry 39(4) (2009) 497-502.

[64] S. Nardecchia, M.C. Serrano, M.C. Gutiérrez, M.T. Portolés, M.L. Ferrer, F. del Monte, Osteoconductive Performance of Carbon Nanotube Scaffolds Homogeneously Mineralized by Flow‐Through Electrodeposition, Advanced Functional Materials 22(21) (2012) 4411-4420.

[65] M. Klotz, M. Weber, S. Deville, D. Oison, I. Iatsunskyi, E. Coy, M. Bechelany, Synthesis of functional ceramic supports by ice templating and atomic layer deposition, Frontiers in Materials 5 (2018) 28.

[66] S.H. Huang, P. Liu, A. Mokasdar, L. Hou, Additive manufacturing and its societal impact: a literature review, The International Journal of Advanced Manufacturing Technology 67(5) (2013) 1191-1203.

[67] J.A. Lewis, J.E. Smay, J. Stuecker, J. Cesarano, Direct ink writing of three‐dimensional ceramic structures, Journal of the American Ceramic Society 89(12) (2006) 3599-3609.

[68] J.A. Lewis, Direct ink writing of 3D functional materials, Advanced Functional Materials 16(17) (2006) 2193-2204.

[69] J. Cesarano, S. Grieco, Robocasting: a new technique for the freeform fabrication of near-net-shape ceramics, Materials Technology 12(3-4) (1997) 98-100.

[70] J.E. Smay, J. Cesarano, J.A. Lewis, Colloidal inks for directed assembly of 3-D periodic structures, Langmuir 18(14) (2002) 5429-5437.

[71] V.G. Rocha, E. Saiz, I.S. Tirichenko, E. García-Tuñón, Direct ink writing advances in multi-material structures for a sustainable future, Journal of Materials Chemistry A 8(31) (2020) 15646-15657.

[72] A. Sydney Gladman, E.A. Matsumoto, R.G. Nuzzo, L. Mahadevan, J.A. Lewis, Biomimetic 4D printing, Nature materials 15(4) (2016) 413-418.

[73] G. Liu, Y. Zhao, G. Wu, J. Lu, Origami and 4D printing of elastomer-derived ceramic structures, Science Advances 4(8) (2018) eaat0641.

[74] D. Kokkinis, M. Schaffner, A.R. Studart, Multimaterial magnetically assisted 3D printing of composite materials, Nature communications 6(1) (2015) 1-10.

[75] K. Chen, X. Kuang, V. Li, G. Kang, H.J. Qi, Fabrication of tough epoxy with shape memory effects by UV-assisted direct-ink write printing, Soft Matter 14(10) (2018) 1879-1886.

[76] R.R. Collino, T.R. Ray, R.C. Fleming, J.D. Cornell, B.G. Compton, M.R. Begley, Deposition of ordered two-phase materials using microfluidic print nozzles with acoustic focusing, Extreme Mechanics Letters 8 (2016) 96-106.

[77] X. Song, H. Tetik, T. Jirakittsonthon, P. Parandoush, G. Yang, D. Lee, S. Ryu, S. Lei, M.L. Weiss, D. Lin, Biomimetic 3D printing of hierarchical and interconnected porous hydroxyapatite structures with high mechanical strength for bone cell culture, Advanced Engineering Materials 21(1) (2019) 1800678.

[78] E. Arzt, A. del Campo, Generating micro-and nanopatterns on polymeric materials, John Wiley & Sons2011.

[79] S. Chandrasekaran, E.B. Duoss, M.A. Worsley, J.P. Lewicki, 3D printing of high performance cyanate ester thermoset polymers, Journal of Materials Chemistry A 6(3) (2018) 853-858.

[80] I.D. Robertson, M. Yourdkhani, P.J. Centellas, J.E. Aw, D.G. Ivanoff, E. Goli, E.M. Lloyd, L.M. Dean, N.R. Sottos, P.H. Geubelle, Rapid energy-efficient manufacturing of polymers and composites via frontal polymerization, Nature 557(7704) (2018) 223-227.

[81] A. Maguire, N. Pottackal, M. Saadi, M.M. Rahman, P.M. Ajayan, Additive manufacturing of polymer-based structures by extrusion technologies, Oxford Open Materials Science 1(1) (2021) itaa004.

[82] C. Zhu, Z. Qi, V.A. Beck, M. Luneau, J. Lattimer, W. Chen, M.A. Worsley, J. Ye, E.B. Duoss, C.M. Spadaccini, Toward digitally controlled catalyst architectures: Hierarchical nanoporous gold via 3D printing, Science advances 4(8) (2018) eaas9459.

[83] H. Wang, C. Chen, F. Yang, Y. Shao, Z. Guo, Direct ink writing of metal parts with curing by UV light irradiation, Materials Today Communications 26 (2021) 102037.

[84] B.Y. Ahn, D. Shoji, C.J. Hansen, E. Hong, D.C. Dunand, J.A. Lewis, Printed origami structures, Advanced Materials 22(20) (2010) 2251-2254.

[85] Z. Guo, R. Yang, T. Wang, L. An, S. Ren, C. Zhou, Cost-effective additive manufacturing of ambient pressure-dried silica aerogel, Journal of Manufacturing Science and Engineering 143(1) (2021).

[86] Z. Guo, L. An, S. Lakshmanan, J.N. Armstrong, S. Ren, C. Zhou, Additive Manufacturing of Porous Ceramics With Foaming Agent, Journal of Manufacturing Science and Engineering 144(2) (2022).

[87] Z. Guo, L. An, S. Khuje, A. Chivate, J. Li, Y. Wu, Y. Hu, J. Armstrong, S. Ren, C. Zhou, 3D-printed electrically conductive silicon carbide, Additive Manufacturing 59 (2022) 103109.

[88] M. Schaffner, P.A. Rühs, F. Coulter, S. Kilcher, A.R. Studart, 3D printing of bacteria into functional complex materials, Science advances 3(12) (2017) eaao6804.

[89] D.B. Kolesky, R.L. Truby, A.S. Gladman, T.A. Busbee, K.A. Homan, J.A. Lewis, 3D bioprinting of vascularized, heterogeneous cell‐laden tissue constructs, Advanced materials 26(19) (2014) 3124-3130.

[90] D.B. Kolesky, K.A. Homan, M.A. Skylar-Scott, J.A. Lewis, Three-dimensional bioprinting of thick vascularized tissues, Proceedings of the national academy of sciences 113(12) (2016) 3179-3184.

[91] A.E. Jakus, E.B. Secor, A.L. Rutz, S.W. Jordan, M.C. Hersam, R.N. Shah, Three-dimensional printing of high-content graphene scaffolds for electronic and biomedical applications, ACS nano 9(4) (2015) 4636-4648.

[92] M.A. Skylar-Scott, S.G. Uzel, L.L. Nam, J.H. Ahrens, R.L. Truby, S. Damaraju, J.A. Lewis, Biomanufacturing of organ-specific tissues with high cellular density and embedded vascular channels, Science advances 5(9) (2019) eaaw2459.

[93] S. Ghosh, S.T. Parker, X. Wang, D.L. Kaplan, J.A. Lewis, Direct‐write assembly of microperiodic silk fibroin scaffolds for tissue engineering applications, Advanced Functional Materials 18(13) (2008) 1883-1889.

[94] S. Tagliaferri, A. Panagiotopoulos, C. Mattevi, Direct ink writing of energy materials, Materials Advances 2(2) (2021) 540-563.

[95] J. Chen, L. Xu, M. Yang, X. Chen, X. Chen, W. Hong, Highly stretchable photonic crystal hydrogels for a sensitive mechanochromic sensor and direct ink writing, Chemistry of Materials 31(21) (2019) 8918-8926.

[96] E.B. Duoss, T.H. Weisgraber, K. Hearon, C. Zhu, W. Small IV, T.R. Metz, J.J. Vericella, H.D. Barth, J.D. Kuntz, R.S. Maxwell, Three‐dimensional printing of elastomeric, cellular architectures with negative stiffness, Advanced Functional Materials 24(31) (2014) 4905-4913.

[97] M. Schaffner, J.A. Faber, L. Pianegonda, P.A. Rühs, F. Coulter, A.R. Studart, 3D printing of robotic soft actuators with programmable bioinspired architectures, Nature communications 9(1) (2018) 1-9.

[98] L. Yang, J. Feng, Z. Liu, Y. Duan, S. Zhan, S. Yang, K. He, Y. Li, Y. Zhou, N. Yuan, Record‐Efficiency Flexible Perovskite Solar Cells Enabled by Multifunctional Organic Ions Interface Passivation, Advanced Materials (2022) 2201681.

[99] P. Wei, H. Leng, Q. Chen, R.C. Advincula, E.B. Pentzer, Reprocessable 3D-printed conductive elastomeric composite foams for strain and gas sensing, ACS Applied Polymer Materials 1(4) (2019) 885-892.

[100] G.H.C. Wong, A. Pant, Y. Zhang, C.K. Chua, M. Hashimoto, C.H. Leo, U.-X. Tan, 3D food printing–sustainability through food waste upcycling, Materials Today: Proceedings (2022).

[101] A. M'barki, L. Bocquet, A. Stevenson, Linking rheology and printability for dense and strong ceramics by direct ink writing, Scientific reports 7(1) (2017) 1-10.

[102] M. Champeau, D.A. Heinze, T.N. Viana, E.R. de Souza, A.C. Chinellato, S. Titotto, 4D printing of hydrogels: a review, Advanced Functional Materials 30(31) (2020) 1910606.

[103] A. Corker, H.C.-H. Ng, R.J. Poole, E. García-Tuñón, 3D printing with 2D colloids: Designing rheology protocols to predict 'printability'of soft-materials, Soft Matter 15(6) (2019) 1444-1456.

[104] T.V. Neumann, M.D. Dickey, Liquid metal direct write and 3D printing: a review, Advanced Materials Technologies 5(9) (2020) 2000070.

[105] R. Karyappa, M. Hashimoto, Chocolate-based ink three-dimensional printing (Ci3DP), Scientific reports 9(1) (2019) 1-11.

[106] X. Chen, Modeling and control of fluid dispensing processes: a state-of-the-art review, The International Journal of Advanced Manufacturing Technology 43(3) (2009) 276-286.

[107] Siqueira, G., Kokkinis, D., Libanori, R., Hausmann, M.K., Gladman, A.S., Neels, A., Tingaut, P., Zimmermann, T., Lewis, J.A. and Studart, A.R., 2017. Cellulose nanocrystal inks for 3D printing of textured cellular architectures. Advanced Functional Materials, 27(12), p.1604619..

[108] J. Mewis, N.J. Wagner, Colloidal suspension rheology, Cambridge university press2012.

[109] G.M. Gratson, J.A. Lewis, Phase behavior and rheological properties of polyelectrolyte inks for direct-write assembly, Langmuir 21(1) (2005) 457-464.

[110] K. Le, Z. Wang, F. Wang, Q. Wang, Q. Shao, V. Murugadoss, S. Wu, W. Liu, J. Liu, Q. Gao, Sandwich-like NiCo layered double hydroxide/reduced graphene oxide nanocomposite cathodes for high energy density asymmetric supercapacitors, Dalton Transactions 48(16) (2019) 5193-5202.

[111] K. Lu, Y. Wang, Z. Liu, L. Han, G. Shi, H. Fang, J. Chen, X. Ye, S. Chen, F. Yang, High‐Efficiency PbS Quantum‐Dot Solar Cells with Greatly Simplified Fabrication Processing via “Solvent‐Curing”, Advanced Materials 30(25) (2018) 1707572.

[112] M. Dinkgreve, J. Paredes, M.M. Denn, D. Bonn, On different ways of measuring “the” yield stress, Journal of non-Newtonian fluid mechanics 238 (2016) 233-241.

[113] Y. Eom, F. Kim, S.E. Yang, J.S. Son, H.G. Chae, Rheological design of 3D printable all-inorganic inks using BiSbTe-based thermoelectric materials, Journal of Rheology 63(2) (2019) 291-304.

[114] L. Martinie, H. Buggisch, N. Willenbacher, Apparent elongational yield stress of soft matter, Journal of rheology 57(2) (2013) 627-646.

[115] N. Louvet, D. Bonn, H. Kellay, Nonuniversality in the pinch-off of yield stress fluids: role of nonlocal rheology, Physical review letters 113(21) (2014) 218302.

Chapter 3 - In-situ X-Ray Observations of Freeze Casting Process

Paper title:

In-situ X-Ray observations and thermal modeling of unidirectional and bidirectional freeze casting

Published in:

Ceramics International, Volume 47, Issue 9, 1 May 2021, Pages 12234-12243

Authors' names:

Guang Yang[1], Fangzhou Li[2], Junfeng Xiao[3], Halil Tetik[1], Nasrullah Shah[4], Xianghui Xiao[5], Jingjing Li[6], Yiliang Liao[7], Shuting Lei[1], Wenda Tan[2], Dong Lin[1]

Authors' affiliations:

1. Department of Industrial and Manufacturing Systems Engineering, Kansas State University, Manhattan, KS 66506, USA
2. Department of Mechanical Engineering, The University of Utah, UT, 84112, USA
3. School of Mechanical Science and Engineering, Huazhong University of Science and Technology, Wuhan, 430074, China
4. Department of Chemistry, Abdul Wali Khan University Mardan, Mardan, KP, Pakistan
5. Brookhaven National Lab, Upton, NY, 11973, USA
6. Department of Industrial and Manufacturing Engineering, The Pennsylvania State University, University Park, PA, 16802, USA
7. Industrial & Manufacturing Systems Engineering, Iowa State University, Ames, IA, 50011, USA

Abstract

Freeze casting is a cost effective, efficient, and versatile technique capable of producing 3D structures with controlled pore shapes, orientation of crystals and components' geometries in many porous materials. Freeze casting of hydroxyapatite (HAP) has been widely applied to bone tissue engineering due to HAP's biodegradable, biocompatible, and osteoconductive properties. It provides interconnected porous structures with a relatively high mechanical strength. However, there are still many unexplained phenomena and features because of the complexity of the process and indirect observation methods. This study demonstrates the use of X-ray synchrotron micro-radiography for providing time-resolved, in-situ imaging of ice crystal growth in the HAP suspensions. The experimental results show the ice crystal growth behavior under unidirectional and bidirectional freeze casting conditions. The finite element modeling (FEM) of the freeze casting process has been generated to predict the development of ice front position and temperature gradient in the suspensions during the freeze casting.

3.1 Introduction

Freeze casting is an environmentally-friendly material processing technique which has been widely applied in different areas, such as energy storage applications [1-2], thermal insulators [3-6], and biomaterials [7]. Hydroxyapatite (HAP), known as human bone mineral, has been used in fabrication of ceramic scaffolds for osseous tissue regeneration for a long time. Recently, freeze-casting-based biomimetic 3D printing of porous HAP has been applied in bone cell cultures [8-11]. The phenomenon of freeze casting is described as a solidification of a water/ice interface propagating through a colloidal suspension of HAP particles [8, 12]. However, the characteristics of the suspension during the freeze casting process are hard to analyze and understand.

Current approaches such as optical microscopy, X-ray radiography or Scanning Electron Microscope (SEM) only provide partial or indirect observations. The freeze casting samples need to be stored at very low temperature conditions. In order to observe the internal structure, the samples need to be freeze-dried to sublimate the ice and sintered at 1300 °C for consolidation. During the sintering process, the internal structure may change due to shrinkage. Such observations are therefore indirect and cannot provide kinetic information. The information during the freeze casting process such as ice crystal growth direction and speed, and the real size of ice crystals is not able to be observed by these methods.

In recent years, X-ray synchrotron radiography became more and more popular due to its in-situ, real-time and direct observation features. Compared to the normal laboratory-based X-ray CT imaging, synchrotron-based X-ray has 3-5 orders of magnitude higher photon flux which allows for shorter imaging time. This technique has been applied to various areas, such as studying mechanical properties and microstructural characteristics [13,14], behaviors of material during metal 3D printing [15], and solidification of colloidal silica aqueous suspension during the freeze casting process [12].

In this work, the X-ray synchrotron radiography has been introduced to observe the ice crystal growth behavior during uni/bidirectional freeze casting. A finite-element modeling (FEM) method has also been developed to predict the ice front position and temperature gradient in the suspension during the freeze casting process. Unidirectional freeze casting indicates that the temperature gradient is only generated in the vertical direction. The growth of ice crystals is only along the vertical direction which is shown in Fig. 3-1b. However, with a combined assembly of a polydimethylsiloxane (PDMS) wedge and an aluminum wedge, the temperature gradients can be generated in both vertical and horizontal directions. At this bidirectional freeze casting

condition, the growth of ice crystals is oriented in a certain angle which is shown in Fig. 3-1d. In order to study the behavior of ice crystal growth under these two conditions, the X-ray synchrotron radiography is introduced for monitoring the freeze casting process. As shown in Fig. 3-1a, while the X-ray beam penetrating the freeze casting sample, some of the energy is absorbed by the sample. Since different materials have different absorption rates of the X-ray, the camera can detect the energy difference and convert the absorption signal into a visible light image which is shown in Fig. 3-1c and Fig. 3-1e. The white and black stripes indicate the ice crystals and HAP particles, respectively. The ice crystal growth behavior can be tracked during the unidirectional and bidirectional freeze casting processes. The phenomenon of freeze casting of HAP suspensions is analyzed and studied.

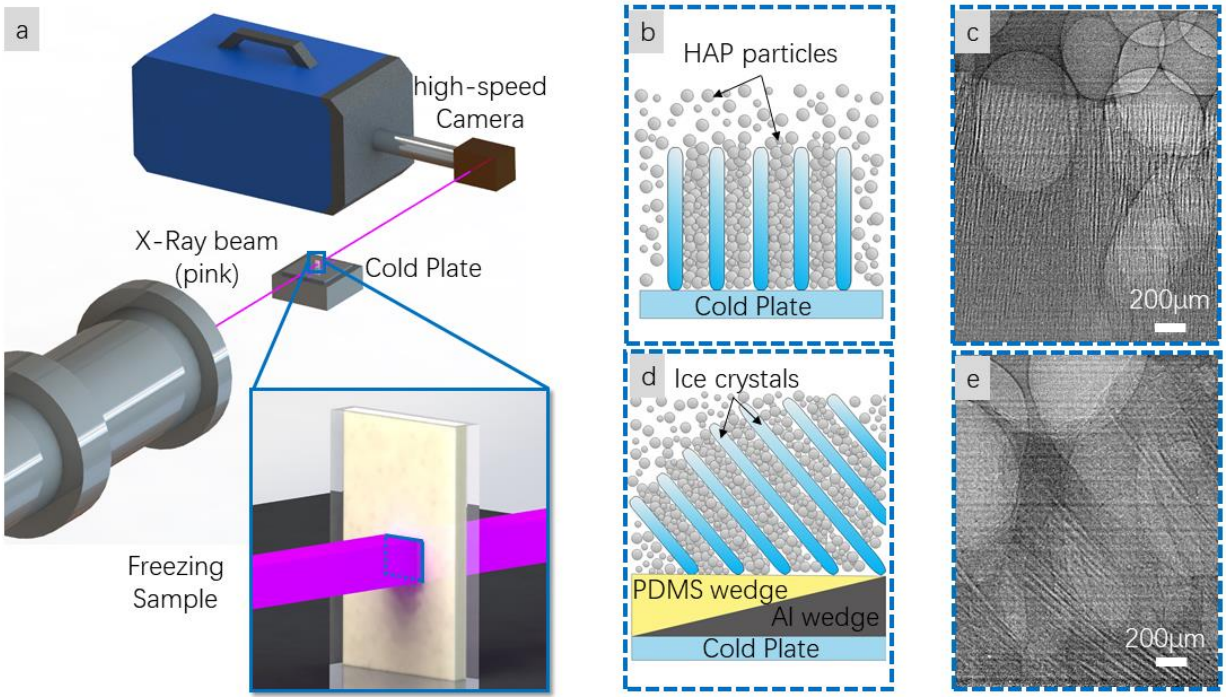

Figure 3-1 In-situ X-ray observation of unidirectional and bidirectional freeze casting: (a) X-ray and freeze casting setup, (b, d) schematic diagram of unidirectional and bidirectional freeze casting, and (c, e) X-ray images of unidirectional and bidirectional freeze casting.

3.2 Experimental Procedures

3.2.1 Suspension preparation

Hydroxyapatite (HAP) suspension was prepared by mixing commercial HAP powders (d50=1-3 micrometer, Trans-Tech, Adamstown, MD) in deionized (DI) water at a concentration of 60 wt%. Darvan C-N (Vanderbilt Minerals, Norwalk, CT) was added by 0.8 wt. % based on the HAP solid to disperse the HAP powder. The suspension was mixed homogenously for 5 hours by magnetic stirring. Thereafter, hydroxypropyl methyl cellulose (H7509, Sigma-Aldrich, Saint Louis, MO), as a viscosifier, was added by 9 mg/mL in the DI water, followed by stirring for 12 hours to dissolve fully. During this step, 1-octonal (112615, Sigma-Aldrich, Saint Louis, MO) was also added by 0.5 vol. % of the distilled water as a defoamer.

3.2.2 Freezing setup and X-ray synchrotron radiography

The well mixed suspension was loaded into a polymer mold with 10 mm length, 21 mm height, and 2mm thickness. As shown in Fig. 3-1a, while the sample was undergoing the freeze casting process, the X-ray beam was penetrating the sample. A high-resolution imaging detector was located at the back of the sample and detected the energy differences. It was then able to convert the absorption signal into visible light images during the freeze casting process which was shown in Fig. 3-1c&e.

For unidirectional freeze casting, the mold was directly put on the cold plate (TP294, Sigma Systems, El Cajon, CA) at -30°C which is presented in Fig. 3-1a. The schematic of unidirectional freeze casting is shown in Fig. 3-1b. For bidirectional freeze casting, a PDMS wedge and an aluminum wedge, both with a 20-degree angle and the same size (90 mm in length, 50 mm in width, and 18.2 mm in height), were assembled to a thick plate. The aluminum

wedge was located at the bottom, which was directly attached to the -30°C cold plate, and the PDMS wedge was on the top side. Since the difference of thermal conductivity between the aluminum wedge and the PDMS wedge is very large, it is able to generate an extra temperature gradient along the horizontal direction. The schematic of bidirectional freeze casting is shown in Fig. 3-1d. The cold plate was cooled using liquid nitrogen with a controller which was used to maintain the temperature of the cold plate at a steady state.

Synchrotron absorption micro-radiography measurements were performed at 2-BM beam line of Advanced Photon Source (APS) at Argonne National Laboratory. The schematic of the X-ray setup is shown in Fig. 3-1a. An X-ray beam with 1.5 mrad incident angle to the beamline mirror was used as light source. A high-resolution imaging detector was used to perform the fast radiography scans. The detector consists of a 100-μm-thick LuAG:Ce scintillator, which converts the X-ray absorption signal into a visible light image. Then the image was magnified by a 2x optic lens and captured by a high-speed camera. The raw reconstructed images were adjusted for brightness and contrast and then cropped to the final size using ImageJ.

3.2.3 Post-processing

The samples frozen on the cold plate were then moved to a -70ºC freezer and kept for 12 hours for further freezing. Next, the samples were loaded into a freeze-drying system (Labconco, Kansas City, MO) under 200mPa vacuum to fully sublimate the ice for 48 hours. After the freeze drying, the dried samples were transferred to a furnace (Kejia, Zhengzhou, China), where the temperature was increased to 500ºC and held there for 2 hours to remove the polymers, and then the temperature was raised to 1300ºC and held there for 3 hours to sinter the samples, both with a ramp rate of 2ºC/min.

3.2.4 optical and Scanning Electron Microscopy(SEM) characterization

A charge-coupled device (CCD) camera (Sentech STC, MB22USB) was used to track the ice front development during the unidirectional and bidirectional freeze casting. The freeze casting conditions were exactly the same as illustrated in section 2.2.

SEM images were taken on a FEI Helios NanoLab 660 (FEI, Hillsboro, OR). The samples were attached to SEM sample holders with conductive double-sided tape and sputter coated with gold before SEM was performed at 10 kV accelerating voltage.

3.3 Finite-Element Modeling(FEM)

In order to quantify the solidification conditions for the ice crystal growth behavior during the uni/bidirectional freeze casting process, the FEM simulations have been performed to simulate the heat transfer in the process using the COMSOL Multiphysics® simulation software. The predicted temperature distribution near the freezing front will provide quantitative information for the understanding of the kinetics of the ice crystal growth

3.3.1 FEM Model Configuration

The unidirectional and bidirectional freeze casting processes are simulated with a model as represented in Fig. 3-2a and Fig. 3-2b. All the geometries are based on the information from the experiments, which is mentioned in the experimental section. The freezing samples are surrounded by the polymer mold, as shown in Fig. 3-2c. For the unidirectional case, the freezing sample, with polymer mold, is at the center of the cold plate which is indicated in Fig. 3-2a. For the bidirectional case, the freezing sample with polymer mold is at the right side of the assembled wedges, as revealed in Fig. 3-2b. In this case, the aluminum wedge is at the bottom, which is directly attached to the cold plate, and the PDMS wedge is on top of the aluminum wedge.

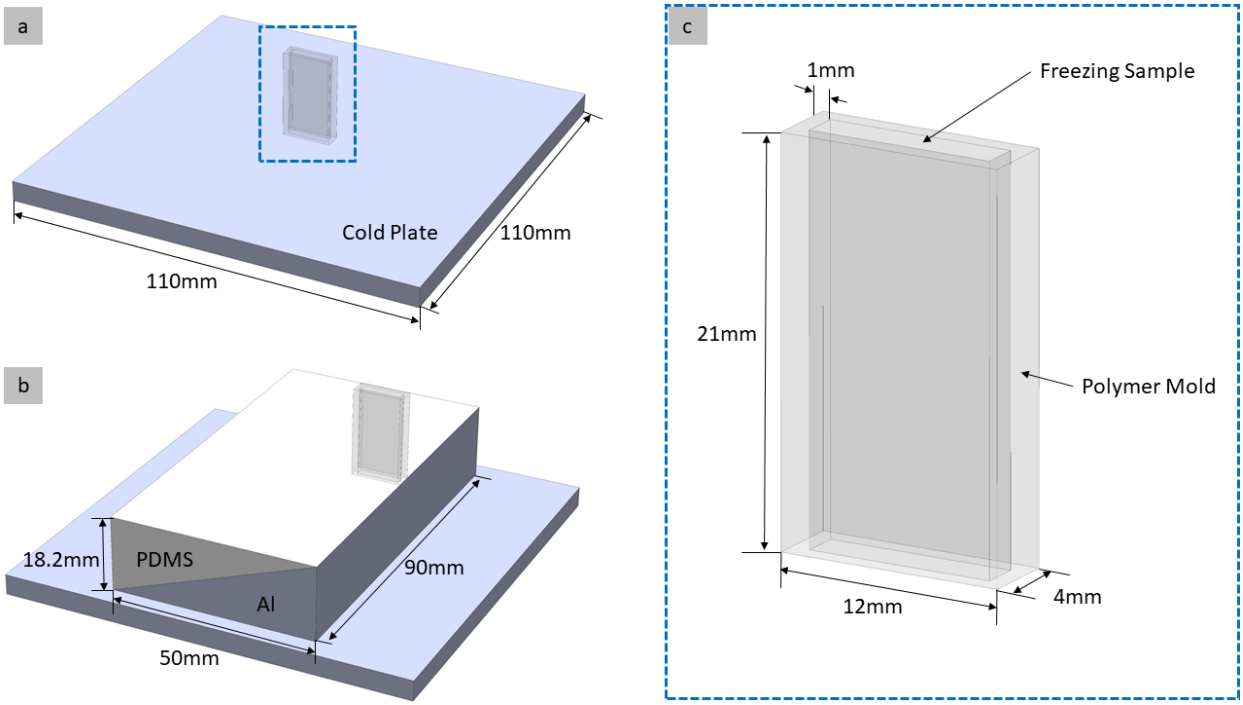

Figure 3-2 Finite element method simulation model configuration: (a) unidirectional freeze casting model description, (b) bidirectional freeze casting model description, and (c) dimension of the freezing sample with polymer mold.

3.3.2 Governing Equations

Convective effect in fluids is neglected in the simulation. The governing equation for the freeze casting process can be simplified as the basic heat transfer equation in fluids and solids:

$$\rho C_p \frac{\partial T}{\partial t} = \nabla \cdot (k \nabla T) + Q_{LH} \quad (1)$$

where ρ is the density, C_p is the heat capacity at constant pressure, T is the temperature, and k is the thermal conductivity. In the simulation for the fluids, only the volumetric latent heat generation between water and ice Q_{LH} is considered.

3.3.3 Boundary/Initial Conditions and Mesh Properties

For both cases, the top surface of the cold plate is fixed at -30°C, shown in Fig. 3-3a. Thermal insulation is set on the front and back faces of the wedges, represented in Fig. 3-3a. Natural heat convection is set for all the other boundaries with a heat transfer coefficient *h* around 1~10Wm-2·K^{-1}. Initially, except the top surface of the cold plate (-30°C), all the domains are given at the room temperature (23°C).

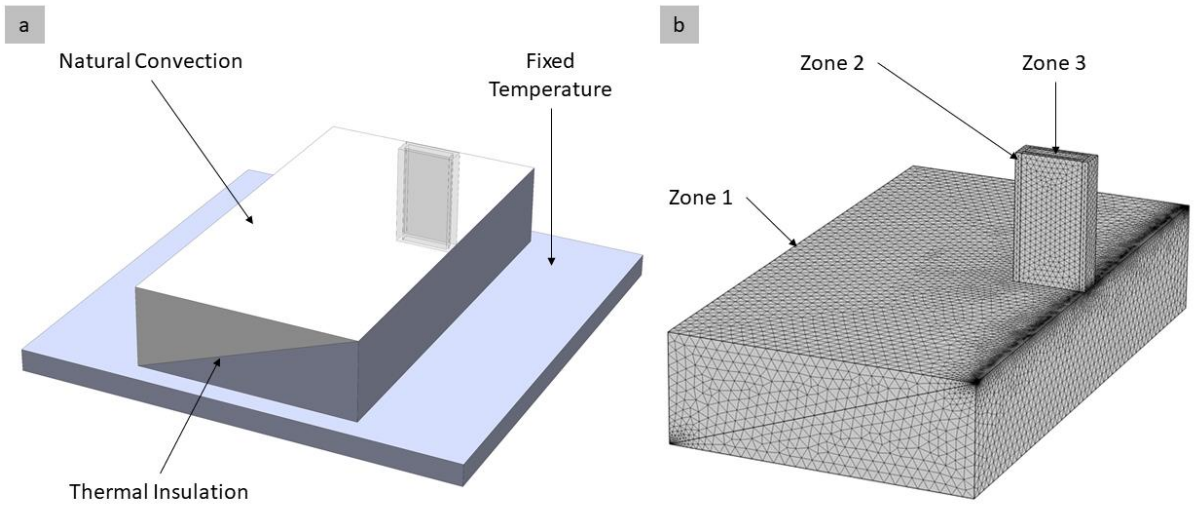

Figure 3-3 Boundary conditions and mesh properties of the model: (a) boundary conditions for different regions and (b) mesh properties for different zones.

As shown in Fig. 3-3b, free tetrahedral elements are used in the whole calculation domain. The maximum element size is 0.0018[m] and the minimum element size is 1.8×10^{-5}[m]. The average mesh size in zone 1 (wedges) is relatively large, which is around 1.5×10^{-3} [m]. The average mesh size in zones 2 and 3 is relatively small, which is around 5×10^{-4}[m]. The mesh size at the lower left corner and the upper right corner of zone 1 is the smallest, where the mesh size is around the minimum mesh size 1.8×10^{-5}[m]. The total number of elements is 367560.

3.3.4 Material Properties

The thermal properties for water (ice) (around 0°C) and HAP are shown in Table 3-1. The real material properties for water and ice are interpolated by the values at different temperatures. The material properties for HAP are calculated by the analytical formula based on the curve fitting from others' work [16]:

$$k_{HAP} = (-3 \times 10^{-14}) \times T^4 + (3 \times 10^{-10}) \times T^3 - (1 \times 10^{-6}) \times T^2 + .0017 \times T + 1.0112 \quad (2)$$

$$C_{p_{HAP}} = 269.55 \times ln(T) - 748.22 \quad (3)$$

$$\rho_{HAP} = 3181.4 - 0.1121 \times T \quad (4)$$

Table 3 - 1 Material properties of water, ice and HAP.

Name	Symbol	Value	Unit
Transition temperature	T_{trans}	273.15	K
Latent heat of fusion	Lm	1.3×10^5	J/kg
Thermal conductivity (HAP)	k_{HAP}	Calculated by (3)	W/(m·K)
Heat capacity (HAP)	$C_{p_{HAP}}$	Calculated by (4)	J/(kg·K)
Density (HAP)	ρ_{HAP}	Calculated by (5)	Kg/m^3
Thermal conductivity(water)	k_{water}	0.56	W/(m·K)
Heat capacity (water)	$C_{p_{water}}$	4220	J/(kg·K)
Density(water)	ρ_{water}	1000	Kg/m^3
Thermal conductivity(ice)	k_{ice}	2.22	W/(m·K)
Heat capacity (ice)	$C_{p_{ice}}$	2050	J/(kg·K)
Density(ice)	ρ_{ice}	916.2	Kg/m^3

The material properties used in the simulation are the mixture of water and HAP. As mentioned previously, water is at a concentration of 60 wt.% of HAP. For any thermal properties, the real value is given by this equation:

$$P_{effective} = 40\% \times P_{water(ice)} + 60\% \times P_{HAP} \quad (5)$$

where *P* represents any kind of thermal property of the mixture.

3.4 Results and discussion

3.4.1 Unidirectional Freeze Casting

In order to generate the unidirectional temperature gradients, the sample holder is directly attached to the -30°C cold plate. The ice crystals only grow along the vertical direction. Since the freezing speed is too fast at the bottom region and the window size is limited, the result captured is located 7mm above the bottom of the sample. The X-ray image of unidirectional freeze casting is shown in Fig. 3-4a. Since the window size of the scanned region is smaller than the freezing sample, only part of the sample was able to be captured (3.26mm x 2.2mm). We can see there are some circular objects within the captured region, which are air bubbles. They were generated during suspension preparation and loading of the suspension to the plastic mold. Since the viscosity of the suspension was quite high, those air bubbles were trapped there and not able to move. As the sample was continuously exposed to the x-ray, the air bubbles became larger due to the heating effect.

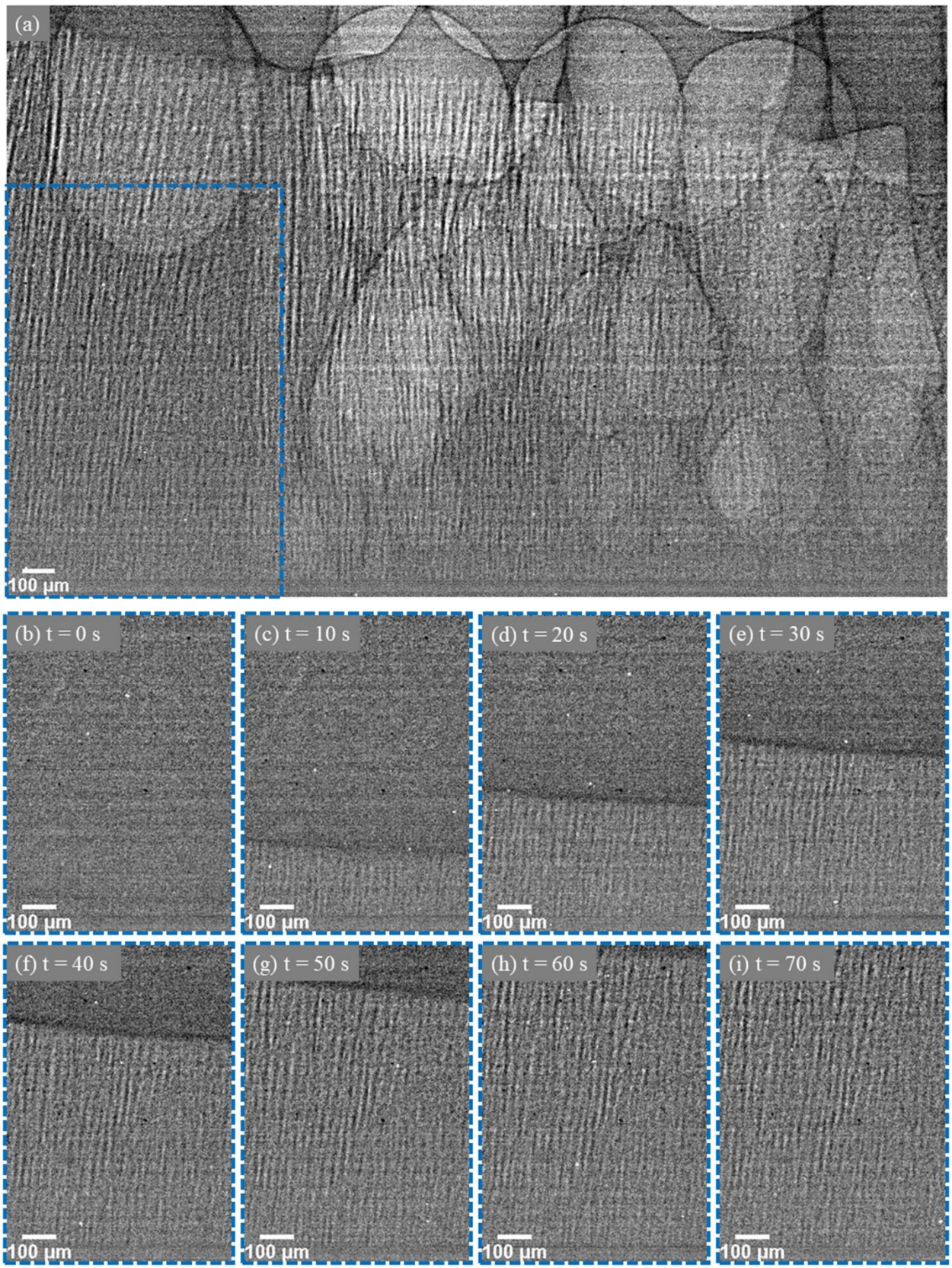
(a)
100 µm
(b) t = 0 s
100 µm
(c) t = 10 s
100 µm
(d) t = 20 s
100 µm
(e) t = 30 s
100 µm
(f) t = 40 s
100 µm
(g) t = 50 s
100 µm
(h) t = 60 s
100 µm
(i) t = 70 s
100 µm

Figure 3-4 In-situ X-ray images of unidirectional freeze casting: (a) X-ray image of the full window, and (b-i) image sequence for the selected part of unidirectional freeze casting.

In order to avoid the interference of air bubbles, a region without air bubbles can be observed to provide a good overview of the progressive growth of the ice crystals along the vertical direction. This region is shown in Fig. 3-4b - Fig. 3-4i. The ice front can be clearly identified during the freeze casting process. The region above the ice front is the unfrozen region, which is the homogeneous unfrozen suspension, so there is no contrast shown in this region. Below the ice front, the well-oriented and well-defined lamellar structures can be observed. These structures indicate the typical ice crystal growth during the unidirectional freeze casting process. Due to the unidirectional ice crystal growth, the HAP particles are pushed in between the growing ice crystals, which formed the lamellar structures. We also notice that the ice crystals growing at the center part of the sample are faster than those growing at the boundary region (ice crystals are higher at the left side which can be observed in fig. 3-4). This phenomenon is due to the low conductivity of the mold, which generates some heat effect to the suspension located at the boundary region.

Since the freeze casting process is highly related to the thermal conditions, the thermal modeling the freeze casting process can help us understand the kinematics of this process. In order to locate the region of ice crystal growth, the FEM simulation was introduced to model the freeze casting process. The simulation results show the temperature distribution change during the freeze casting process. The 0°C line is considered as the interface between the solid and the liquid. The model can provide us with the position of 0°C line with respect of time, which is shown in Fig. 3-5a - Fig. 3-5d.

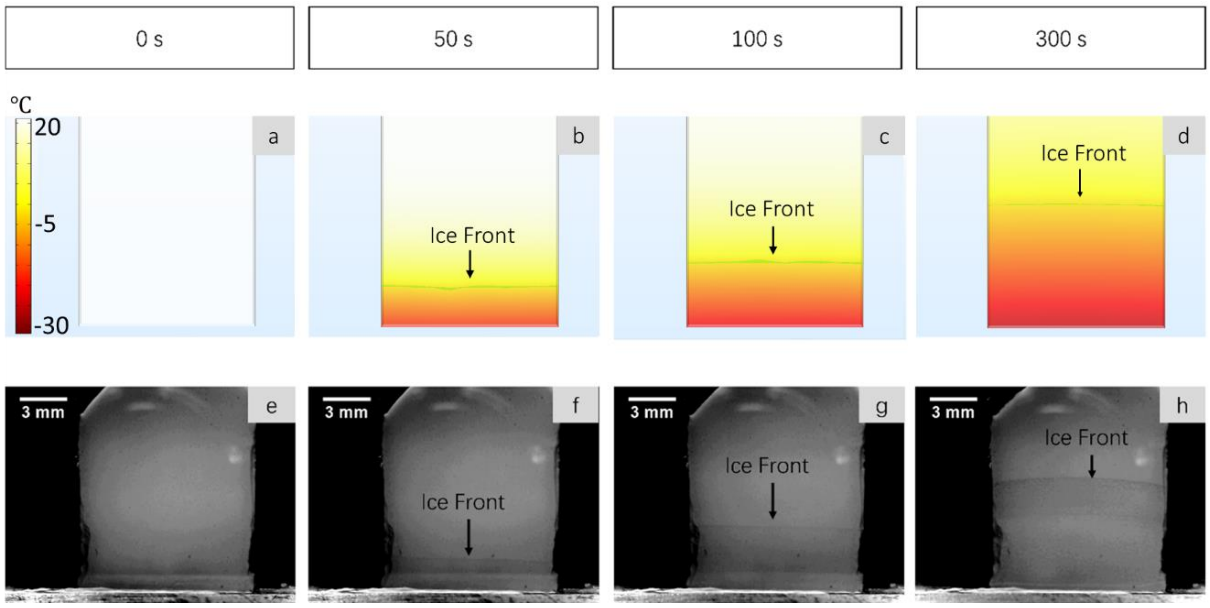

Figure 3-5 Ice-profile propagation during the unidirectional freeze casting. (a-d) FEM simulation of unidirectional freeze casting. (e-h) Optical image sequences of unidirectional freeze casting.

In order to validate the simulation results, the unidirectional freeze casting experiment was recorded using a charge-coupled-device (CCD) camera. The image sequences are shown in Fig. 3-5e - Fig. 3-5i. The experiment was performed with the exact same conditions as before. The reason for using the CCD camera is to capture the whole area of the sample and make accurate measurements. The image sequences show that the ice front propagation speed is fast at the beginning, and gradually slow down as the ice crystals propagate further. We can also notice that the ice growing speed is faster at the center and slower at the boundary, which can also be observed from the x-ray images.

The ice front positions are recorded through the unidirectional freeze casting process for both FEM simulation and optical image sequences. In order to avoid the boundary heat effect, the ice front positions at the center of the mold were measured. Both the FEM simulation and the

optical imaging results are plotted in Fig. 3-6a and 3-6b. The in-situ x-ray results started from 7mm height are also plotted in Fig. 3-6a and 3-6b. The FEM simulation, optical image, and in-situ X-ray image all show similar trends regarding the height and velocity for the freezing front. It is found that the freezing front starts with a rather high velocity, which gradually approaches to a quasi-steady value in the later stage of the process, this is consistent with the experimental observation in [17] and the analytical prediction in [18]. The temperature gradient on the freezing front cannot be directly measured from the experiments, but can be evaluated based on the FEM simulation as shown in Fig.3-6c. Similar to the trends for the freezing front velocity, the temperature gradient starts with a high value and gradually approach to a constant.

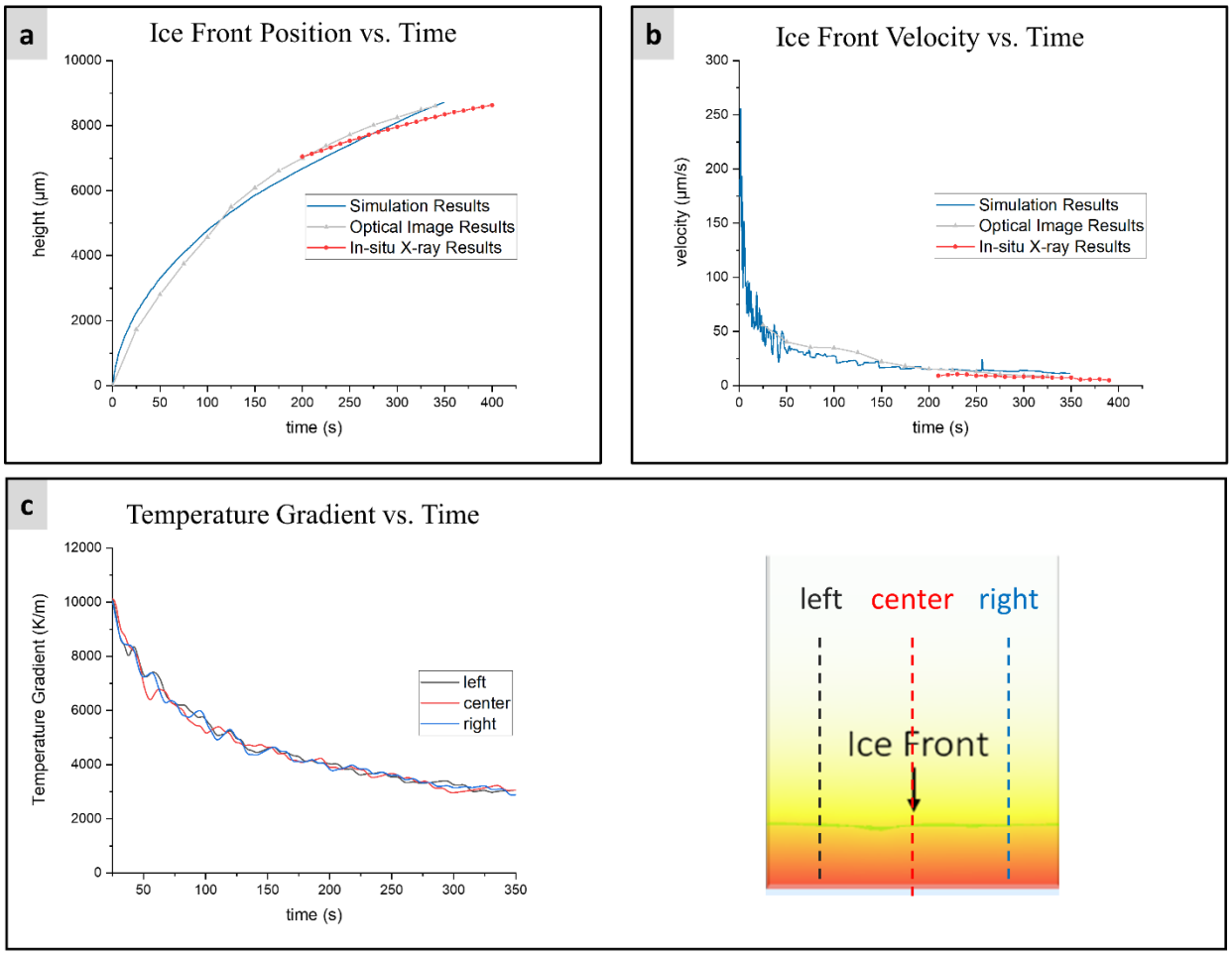

Figure 3-6 Ice front position, velocity, and temperature gradient vs. the time of unidirectional freeze casting. (a) Ice front position vs. the time. (b) Ice front moving velocity vs. the time. (c) Temperature Gradient vs. the time.

3.4.2 Bidirectional Freeze Casting

The idea for bidirectional freeze casting is to modify the geometry of the cooling source. Instead of directly attaching the sample to the -30°C flat cold plate, a combination of a PDMS wedge and an aluminum wedge is developed to create the temperature gradients in both the vertical and horizontal directions. Due to the large difference of thermal conductivity for aluminum and PDMS, the cooling speed is much faster at the side close to the aluminum wedge.

The X-ray image of bidirectional freeze casting is shown in Fig. 3-7a. Compared to the vertical aligned ice crystals for unidirectional freeze casting, the bidirectional freeze casting is able to orientate the ice crystal growing direction to a certain angle. In order to identify the ice crystal growth behavior during the bidirectional freeze casting, an area initially without ice crystals has been monitored with respect to time which is shown in Fig. 3-7e- Fig. 3-7i. The ice crystals initiate from the lower right region and propagate along the temperature gradient to the upper left region, which is exactly the same as we proposed for ice crystalizing behavior of bidirectional freeze casting.

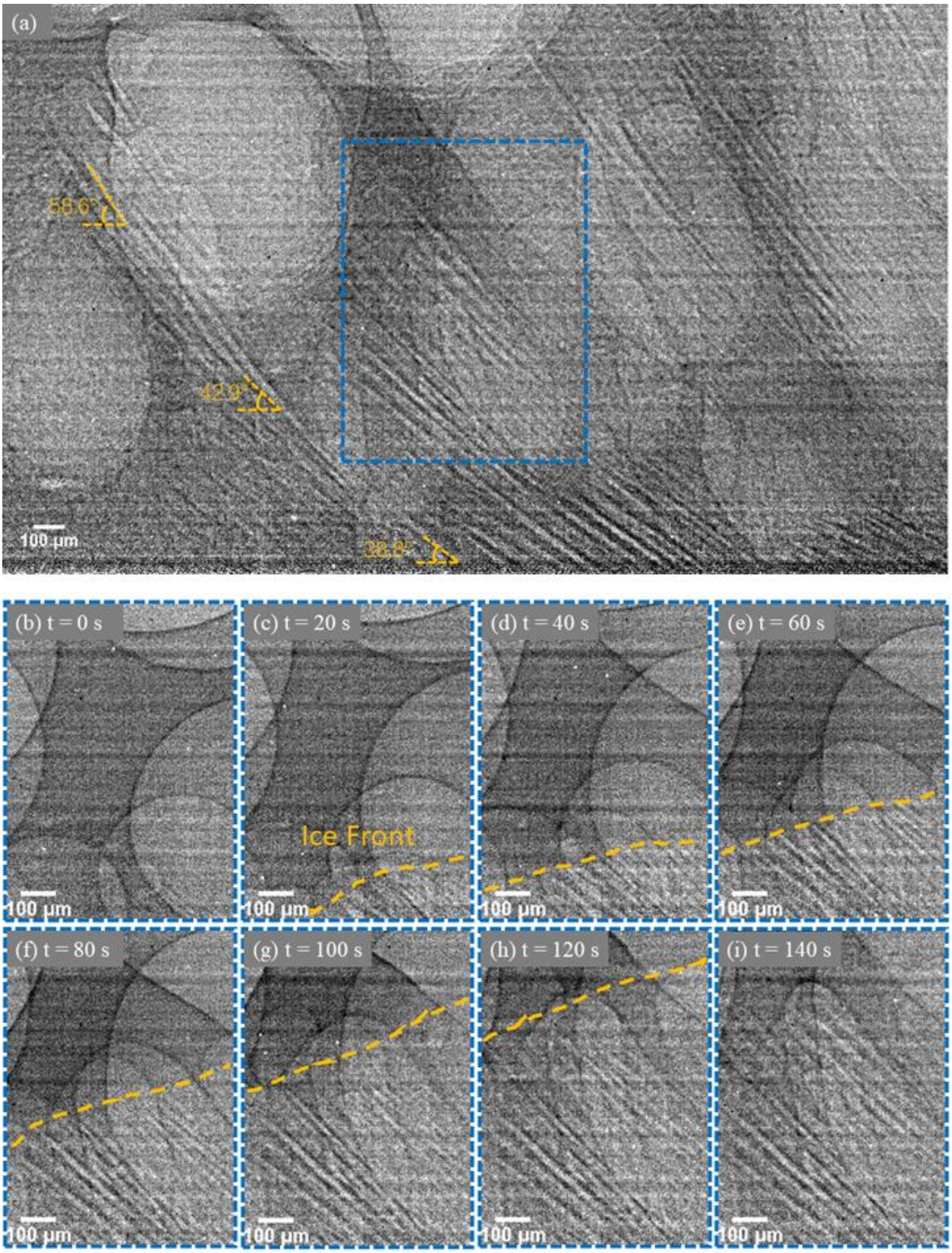
(a)
58.6°
42.9°
38.8°
100 µm
(b) t = 0 s
(c) t = 20 s
Ice Front
(d) t = 40 s
(e) t = 60 s
(f) t = 80 s
(g) t = 100 s
(h) t = 120 s
(i) t = 140 s

Figure 3-7 In-situ X-ray images of bidirectional freeze casting: (a) X-ray image of the full window, and (b-i) image sequence for the selected part of bidirectional freeze casting.

Also, it is noted that the ice crystals are not growing in a straight line during the whole process. The angle between the ice crystals and the horizontal line is small at the beginning and keeps increasing during the bidirectional freeze casting process. As we can see from fig. 3-7a, if we track the growth of a single ice crystal, the angle is 38.8° at the beginning, then increases to 42.9°, and finally to 58.6°. That means the ratio of ice crystal growing speed in the vertical direction/horizontal direction is not a constant value. In order to study the kinematics of the ice crystals' growth behavior under the bidirectional freeze casting process, the FEM model is also conducted to simulate this process. Fig. 3-8a - Fig. 3-8d shows the simulation results for the ice front positions with respect of time. The bidirectional freeze casing experiment is also recorded by a CCD camera which is shown in Fig. 3-8e - Fig. 3-8h. The results show that the ice front is exactly following the temperature gradient during the freeze casting process. Since the mold was thin, there is some heat effect at the boundary which slows down the freezing. Both CDD images and FEM simulation validate this observation.

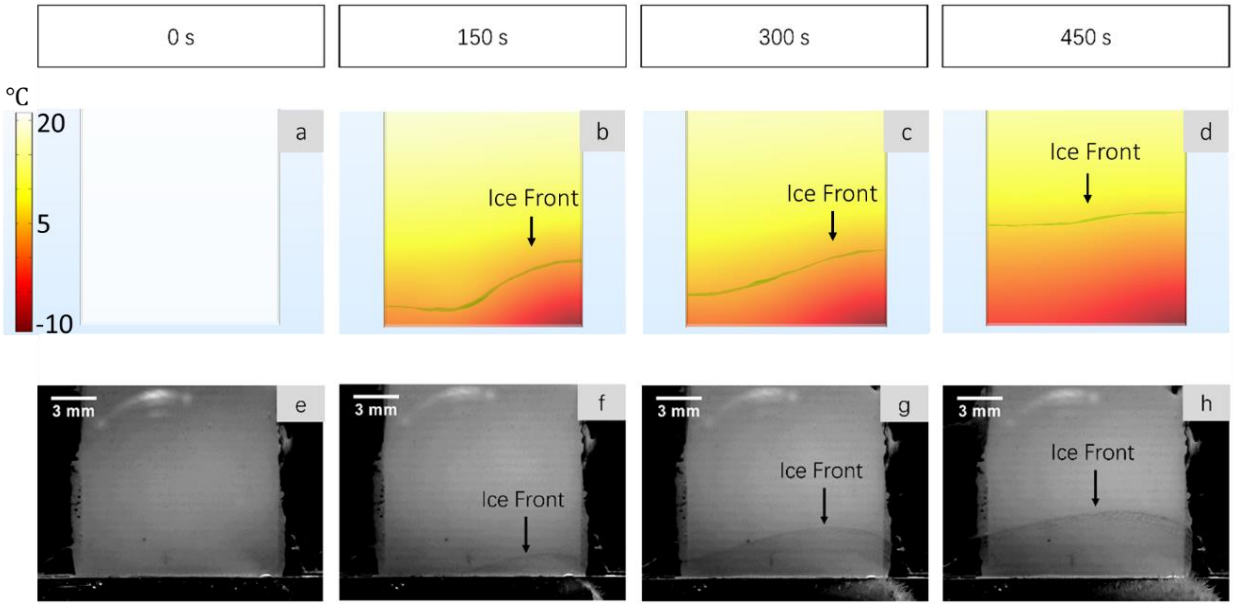

Figure 3-8 Ice-profile propagation during the bidirectional freeze casting. (a-d) FEM simulation of bidirectional freeze casting. (e-h) Optical image sequences of bidirectional freeze casting.

The ice front positions and velocity at the centerline of the mold are recorded through the bidirectional freeze casting process for both the FEM simulation and optical image sequences. The simulation and the experimental results are plotted in Fig. 3-9a and 3-9b, which shows a good agreement. The temperature gradient along the normal direction of the solidification front is also plotted in Fig. 3-9c.

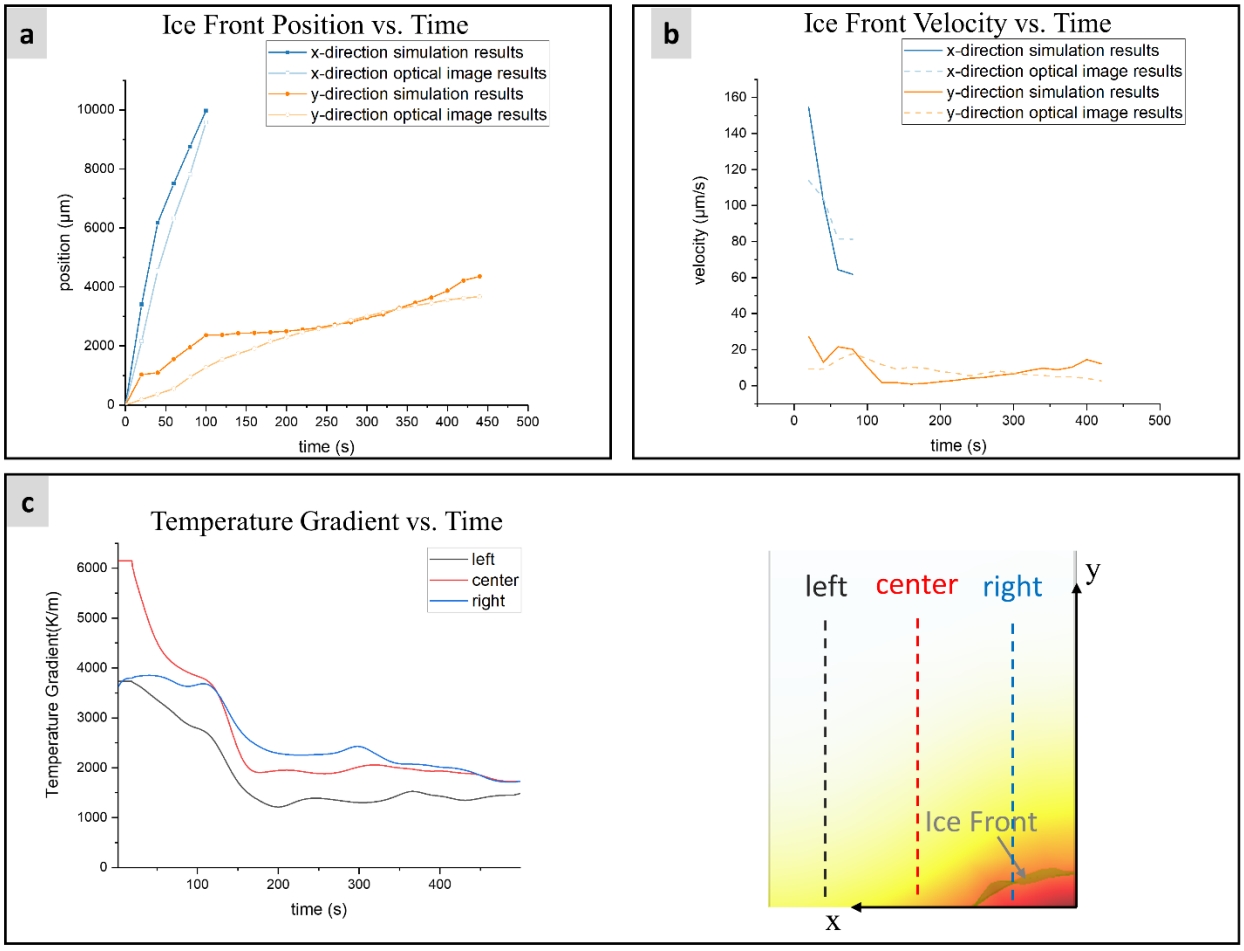

Figure 3-9 Ice front position, velocity, and temperature gradient vs. the time of bidirectional freeze casting. (a) Ice front position vs. the time. (b) Ice front moving velocity vs. the time. (c) Temperature Gradient vs. the time.

To compare the unidirectional and bidirectional processes, obvious differences in the solidification conditions can be found for the two cases. At their quasi-stead states, the front velocity and temperature gradient are about 20μm/s and 3000K/m for the unidirectional case, and are about 10μm/s and 1650K/m for the bidirectional case. These differences may explain the different pore sizes that will be discussed later.

3.4.3 SEM Results

After the unidirectional and bidirectional freeze casing of the HAP suspension, the frozen samples are loaded into a freeze drying system for 48 hours to fully sublimate the ice. After freeze-drying, the samples were heated up to 500°C to remove the polymers and sintered at 1300°C to produce the strengthened HAP scaffold.

The SEM images of the top and cross-sectional view of the sintered samples are shown in Fig. 3-10. Fig. 3-10a and Fig. 3-10b show the top surface of the unidirectional freeze casting sample, where the pores are randomly aligned at the horizontal direction because the temperature gradient only has one direction (from bottom to top). However, with the bidirectional freeze casting, the pores are also oriented along the second temperature gradient, which can be seen in Fig. 3-10e and Fig. 3-10f. (Fig. 3-10 c and d) and (Fig. 3-10 g and h) show the cross-sectional view of the unidirectional and bidirectional freeze casting samples. Since the sample shrinks during the sintering process, the interconnected pores are smaller than those observed from the X-ray images. However, the SEM image can still validate the X-ray images which clearly identify the direction of ice crystals growth and wall-ice distributions during the freeze casting process. Also, we can find out that the bidirectional samples have larger pores than the unidirectional samples, which is also can be identified from the X-ray image. The X-ray images shows that the ice crystals are relatively larger because the freezing speed is much slower during the bidirectional freeze casing.

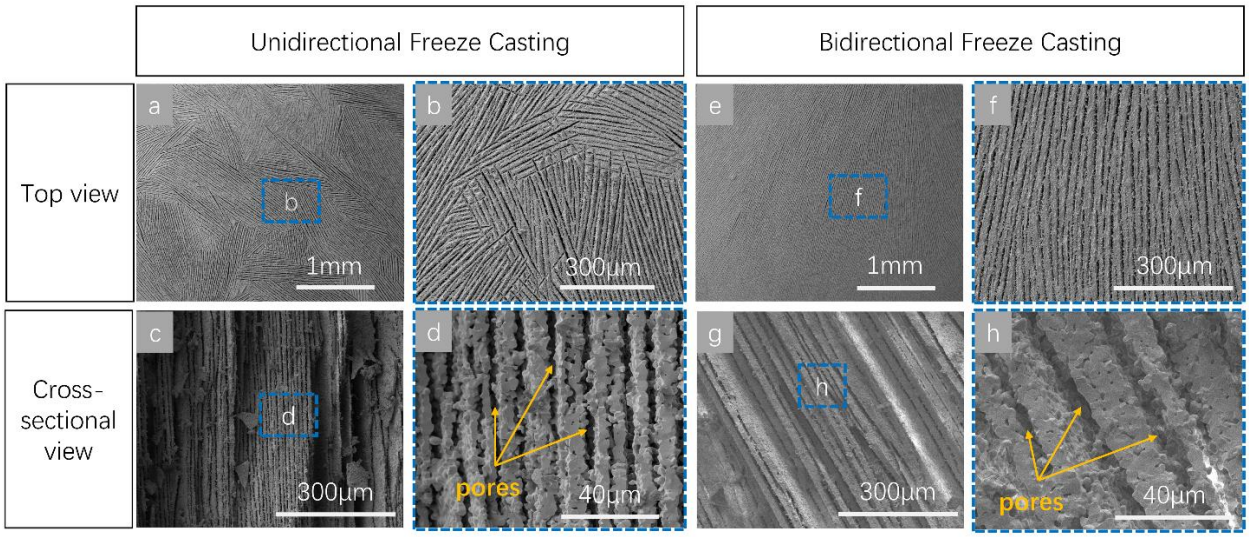

Figure 3-10 SEM images of sintered HAP samples: (a, b) top view of the unidirectional freeze casting samples, (c, d) cross sectional view of unidirectional freeze casting samples, (e, f) top view of bidirectional freeze casting samples, and (g, h) cross sectional view of bidirectional freeze casting samples.

3.5 Conclusion

In conclusion, a new method utilizing X-ray synchrotron radiography to observe and FEM thermal modeling to predict uni/bidirectional freeze casting HAP suspensions has been developed in this work. The ice crystal growth with its unique structures can be in-situ observed during the uni/bidirectional freeze casting processes. With the help of FEM thermal modeling, we are also able to predict the development of the ice front position and temperature gradient in the suspensions during the freeze casting process. The results have also been validated through the CCD and SEM images. The bidirectional freeze casting method with PDMS/Al wedges can generate the second temperature gradient and result in larger pores. By manipulating the cooling speed and directions, we can potentially control the internal structures of freeze casting samples

which can be in-situ observed using X-ray synchrotron radiography. It provided a new method to observe the internal structures during the experiment and increase the efficiency while conducting the experiments.

Acknowledgement

This work is supported by the Johnson Cancer Research Center. This research used resources of the Advanced Photon Source, a U.S. Department of Energy (DOE) Office of Science User Facility operated for the DOE Office of Science by Argonne National Laboratory under Contract No. DE-AC02-06CH11357.

References

[1] U.S. Energy Information Administration, 2017, "Monthly Energy Review," http://www.eia.gov/totalenergy/data/monthly/pdf/mer.pdf.

[2] BP, "BP Statistical Review of World Energy," 2016, https://www.bp.com/content/dam/bp/pdf/energy-economics/statistical-review-2016/bp-statistical-review-of-world-energy-2016-full-report.pdf.

[3] Huber, G.W., 2008, "Breaking the Chemical and Engineering Barriers to Lignocellulosic Biofuels: Next Generation Hydrocarbon Biorefineries" Based on the June 25-26, 2007 Workshop, Washington, DC: National Science Foundation, Chemical, Biogengineering, Environmental and Transport Systems Division.

[4] U.S. Energy Information Administration, 2013, "How Much Petroleum Does the United States Import and from Where?" http://www.eia.gov/tools/faqs/faq.cfm?id=727&t=6.

[5] Bastani, P., Heywood, J.B., and Hope, C.,2012, "Fuel Use and CO2 Emissions Under Uncertainty From Light-Duty Vehicles in the U.S. to 2050," Journal of Energy Resources Technology, 134(4):042202-042202-10.

[6] Zhang. C., Ge, Y., Tan, J., li, L., Peng, Z., and Wang, X., 2017, "Emissions From Light-Duty Passenger Cars Fueled With Ternary Blend of Gasoline, Methanol, and Ethanol,"Journal of Energy Resources Technology, 139(6):062202-062202-8.

[7] Bracmort, K., 2015, "The Renewable Fuel Standard (RFS): Cellulosic Biofuels," R41106, Congressional Research Service, http://nationalaglawcenter.org/wp-content/uploads/assets/crs/R41106.pdf.

[8] Gouli, S.S., Serdari, A.A., Stournas, S.S., and Lois, E.E., 2000, "Transportation Fuel Substitutes Derived From Biomass," Journal of Energy Resources Technology, 123(1):39-43.

[9] U.S. Department of Transportation, 2010, “Transportation’s Role in Reducing U.S. Greenhouse Gas Emissions, http://ntl.bts.gov/lib/32000/32700/32779/DOT_Climate_Change_Report_-_April_2010_-_Volume_1_and_2.pdf.

[10] Brenes, M.D., 2006. “Biomass and Bioenergy: New Research,” Nova Science Publishers, Inc., ISBN: 1-59454-865-X.

[11] Wei, L., Pordesimo, L.O., Igathinathane, C. and Batchelor, W.D., 2009. “Process Engineering Evaluation of Ethanol Production from Wood through Bioprocessing and Chemical Catalysis,” Biomass and Bioenergy, 33(2), pp.255-266.

[12] Kumar, P., Barrett, D.M., Delwiche, M.J. and Stroeve, P., 2009. “Methods for pretreatment of lignocellulosic biomass for efficient hydrolysis and biofuel production,” Industrial & engineering chemistry research, 48(8), pp.3713-3729.

[13] Zhu, W., Zhu, J.Y., Gleisner, R. and Pan, X.J., 2010. “On Energy Consumption for Size-reduction and Yields from Subsequent Enzymatic Saccharification of Pretreated Lodgepole Pine,” Bioresource Technology, 101(8), pp.2782-2792.

[14] Bergman, P.C.A., 2005. “Combined Torrefaction and Pelletisation. the TOP Process,” Energy Centre of Netherlands, Report No. ECN-C-05-073.

[15] Bergman, P.C., Boersma, A.R., Zwart, R.W.R. and Kiel, J.H.A., 2005. “Torrefaction for Biomass Co-Firing in Existing Coal-fired Power Stations,” Energy Centre of Netherlands, Report No. ECN-C-05-013.

[16] Zhang, M., Song, X., Deines, T.W., Pei, Z.J. and Wang, D., 2012, “Biofuel Manufacturing from Woody Biomass: Effects of Sieve Size Used in Biomass Size Reduction.” BioMed Research International, 2012 (2012), pp. 581039.

[17] Miao, Z., Grift, T.E., Hansen, A.C., and Ting, K.C., 2010, "Specific Energy Consumption of Biomass Particle Production and Particle Physical Property," The ASABE Annual International Meeting, Pittsburgh, PA; 20-23 June 2010, Paper Number: 1008497.

[18] Miao, Z., Grift, T.E., Hansen, A.C., and Ting, K.C., 2011 "Energy Requirement for Comminution of Biomass in Relation to Particle Physical Properties," Industrial Crops and Products, 33, pp. 504-513.

[19] Deines, T.W., and Pei, Z.J., 2010, "Power Consumption Study in Knife Milling of Wheat Straw," Transactions of the North American Manufacturing Research Institution of SME, 38, pp. 191-196.

[20] Deines, T.W., Nottingham, D., Pei, Z.J., 2010, "Effects of Biomass Type and Sieve Size on Power Consumption in Knife Milling," Proceedings of the IIE Annual Conference and Expo 2010, Cancun, Mexico, June 5-9, 2010.

[21] Vidal, B.C., Dien, B.S., Ting, K.C. and Singh, V., 2011. "Influence of Feedstock Particle Size on Lignocellulose Conversion-A Review." Applied Biochemistry and Biotechnology, 164(8), pp.1405-1421.

[22] Cadoche, L. and López, G.D., 1989, "Assessment of Size Reduction as a Preliminary Step in the Production of Ethanol from Lignocellulosic Wastes," Biological Wastes, 30(2), pp.153-157.

[23] Schell, D.J. and Harwood, C., 1994, "Milling of Lignocellulosic Biomass," Applied Biochemistry and Biotechnology, 45(1), pp.159-168.

[24] Mani, S., Tabil, L.G. and Sokhansanj, S., 2004, "Grinding Performance and Physical Properties of Wheat and Barley Straws, Corn Stover and Switchgrass," Biomass and Bioenergy, 27(4), pp.339-352.

[25] Bitra, V.S., Womac, A.R., Chevanan, N., Miu, P.I., Igathinathane, C., Sokhansanj, S. and Smith, D.R., 2009, "Direct Mechanical Energy Measures of Hammer Mill Comminution of Switchgrass, Wheat straw, and Corn Stover and Analysis of their Particle Size Sistributions," Powder Technology, 193(1), pp.32-45.

[26]Wright, C.T., Pryfogle, P.A., Stevens, N.A., Hess, J.R., and Radtke, C.W., 2006, "Value of Distributed Preprocessing of Biomass Feedstocks to a Bioenergy Industry," Proceedings of the 2006 ASABE Annual International Meeting, Portland, OR, July 9-12, Paper number 066151

[27] Arthur, J.F., Kepner, R.A., Dobie, J.B., Miller, G.E., and Parsons, P.S., 1982, "Tub Grinder Performance with Crop and Forest Residues," Transactions of the ASABE. 25(6), pp. 1488-1494.

[28] Himmel, M., Tucker, M., Baker, J., Rivard, C., Oh, K., and Grohmann, K., 1985, "Comminution of Biomass: Hammer and Knife Mills," Biotechnology and Bioengineering Symposium, 15, pp. 39-58.

[29] Ghorbani, Z., Masoumi, A.A., and Hemmat, A., 2010, "Specific Energy Consumption for Reduction the Size of Alfalfa Chops Using a Hammer Mill," Biosystems Engineering, 105, pp. 34-40.

[30] Womac, A.R., Igathinathane, C., Bitra, P., Miu, P., Sokhansanj, S., and Narayan, S., 2007, "Biomass Pre-processing Size Reduction with Instrumental Mills," Proceedings of

[31] Yancey, N.A., Wright, C.T., Conner, C.C., and Hess, J. R., 2009, "Preprocessing Moist Lignocellulosic Biomass for Biorefinery Feedstocks," Proceedings of the 2009 ASABE Annual International Meeting, Reno, NV, June 21-24, No.08-14983

[32] Song, X.X., Zhang, M., Pei, Z.J., and Wang, D.H., 2014, "Ultrasonic Vibration-assisted Pelleting of Wheat Straw: A Predictive Model for Energy Consumption Using Response Surface Methodology," Ultrasonics, 54(1), pp. 305-311.

[33] Song, X.X., Zhang, M., Deines, T.W., Zhang, P.F., and Pei, Z.J., 2013, "Energy Consumption Study in Ultrasonic Vibration-assisted Pelleting Of Wheat Straw for Cellulosic Biofuel Manufacturing," International Journal of Manufacturing Research, 8(2), pp. 135-149.

[34] Svihus, B., Kløvstad, K.H., Perez, V., Zimonja, O., Sahlström, S., Schüller, R.B., Jeksrud, W.K. and Prestløkken, E., 2004. "Physical and Nutritional Effects of Pelleting of Broiler Chicken Diets Made from Wheat Ground to Different Coarsenesses by the Use of Roller Mill and Hammer Mill," Animal Feed Science and Technology, 117(3), pp.281-293.

[35] Zhang, Q., Zhang, P., Pei, Z.J., Wilson, J., McKinney, L. and Pritchett, G., 2011, "Ultrasonic-vibration assisted Pelleting for Cellulosic Ethanol Manufacturing: An Experimental Investigation of Power Consumption," ASME 2011 International Mechanical Engineering Congress and Exposition, Denver, Colorado, November 11-17, 2011, IMECE 2011-64307.

[36] Mani, S., Tabil, L.G., Sokhansanj, S., 2006. "Effects of Compressive Force, Particle Size and Moisture Content on Mechanical Properties of Biomass Pellets from Grasses," Biomass Bioenergy 30 (7), 648–654.

[37] Mani, S., Tabil, L.G. and Sokhansanj, S., 2003. "Compaction of Biomass Grinds-an Overview of Compaction of Biomass Grinds," Powder Handling and Processing, 15(3), pp.160-168.

[38] Song, X.X., Zhang, M., Pei, Z.J., and Wang, D.H., 2015, "Ultrasonic Vibration-assisted (UV-A) Pelleting of Wheat Straw: a Constitutive Model for Pellet Density," Ultrasonics, 60, pp. 117-125.

[39] Song, X.X., Yu, X.M., Zhang, M., Pei, Z.J., and Wang, D.H., 2014, "A Physics-based Temperature Model for Ultrasonic Vibration-assisted Pelleting of Cellulosic Biomass," Ultrasonics,54(7), pp. 2042-2049.

[40] McBain, R., 1966, “Pelleting Animal Feed,” American Feed Manufacturers Association. Arlington, VA, USA.

[41] Chundawat, S.P., Venkatesh, B. and Dale, B.E., 2007. “Effect of Particle Size Based Separation of Milled Corn Stover on AFEX Pretreatment and Enzymatic Digestibility,” Biotechnology and bioengineering, 96(2), pp.219-231.

[42] Singh, D., & Kashyap, M. M. 1985. “Mechanical and Combustion Characteristics of Paddy Husk Briquettes,” Agricultural Wastes, 13(3), 189-196.

[43] Franke, M., & Rey, A. 2006. “Pelleting Quality,” World Grain, 24(5), 78-79.

[44] Hoover, A.N., Tumuluru, J.S., Teymouri, F., Moore, J. and Gresham, G., 2014. “Effect of Pelleting Process Variables on Physical Properties and Sugar Yields of Ammonia Fiber Expansion Pretreated Corn Stover,” Bioresource technology, 164, pp.128-135.

[45] HILL, B., AND D.A. PULKINEN,1988 “A Study of the Factors Affecting Pellet Durability and Pelleting Efficiency in the Production of Dehydrated Alfalfa Pellets,” A Special Report, 25; Saskatchewan Dehydrators Association, Tisdale, SK, Canada.

[46] PAYNE, J.D. 1978 “Improving Quality of Pelleted Feeds;” Milling Feed and Fertilizer, 161(5), pp.34-41.

Chapter 4 - In-situ X-Ray Observations of 3D Freeze Printing

Paper title:

In-situ Imaging of Three Dimensional Freeze Printing Process using Rapid X-Ray Synchrotron Radiography

Published in:

Review of Scientific Instruments, Volume 93, Issue 1, 13 January 2022, Pages 013703

Authors' names:

Guang Yang[1], Halil Tetik[1], Johanna Nelson Weker[2], Xianghui Xiao[3], Shuting Lei[1], Dong Lin[1]

Authors' affiliations:

1. Department of Industrial and Manufacturing Systems Engineering, Kansas State University, Manhattan, KS 66506, USA
2. Stanford Synchrotron Radiation Lightsource, SLAC National Accelerator Laboratory, Menlo Park, CA 94025
3. Brookhaven National Lab, Upton, NY 11973, USA

Abstract

Three dimensional freeze printing (3DFP) combines the advantages of freeze casting and additive manufacturing to fabricate multifunctional aerogels. Freeze casting is a cost-effective, efficient, and versatile method capable of fabricating micro-scale porous structures inside the aerogels for many different applications. The 3DFP provided the capability of fabricating highly customized geometries with controlled microporous structures as well. However, there are still many unexplained phenomena and features because of the complexity of post-processes and indirect observation methods. This study demonstrates the design and construction of the in-situ imaging systems which use the X-ray synchrotron radiography to observe freeze casting and 3DFP processes. With the advantages provided by the in-situ X-ray imaging techniques, the ice crystal growth with its unique lamellar structures can be observed during the freeze casting process. The movement of freeze front, material deposition, and growing of ice crystals can also be visualized during the inkjet-based 3DFP process.

4.1 Introduction

Freeze casting is a well-known method for developing porous structures, including from ceramics [1-5], metals [6-10], carbon-based materials [11-13], nanocomposites [14-17], and so on, which showed promising properties for many different applications such as energy storage and conversion [18-20], photo catalysis [21], liquid chromatography [22], sensors [23-25], and bioengineering [26, 27]. The freeze casting method has a simple procedure, an environmental-friendly nature, and the ability to tailor the microstructure of the final product [28]. In this method, the precursor slurry, which is composed of a liquid solvent and solute particles, is solidified (frozen) inside a thermally insulating mold to obtain the desired shape. Then solidified

solvent is sublimated under low pressure and low-temperature conditions (freeze-drying) [29-32]. During freeze casting, the solute particles are rejected by growing crystals of solvent, which results in a tightly packed network of solute particles. Once the solvent crystals are sublimated by freeze drying, a porous structure whose morphology is a replica of the solvent ice crystals is obtained [29].

Even though the freeze casting provides a variety of tools (e.g., solidification rate, solid content in the precursor slurry, using chemical additives in the formulation of precursor slurry, etc.) to manipulate the microstructure of the object, the macrostructure of the fabricated body is highly limited by the shape of the mold during the freeze casting process. To eliminate the dependency on the mold and achieve porous structures with complex macro geometries, our group developed the Three Dimensional Freeze Printing (3DFP) technique which combined the advantages of freeze casting process and additive manufacturing techniques. The 3DFP technique provides a way to fabricate objects with both desired micro/macro-structures. Accordingly, Song et al. fabricated 3D hydroxyapatite (HAP) scaffold which was used for bone cell culture and Dasyam et al. proposed the 3DFP of Cellulose Nano Crystal (CNC) aerogel as ultra-lightweight sound absorbers[33, 34]. The ink was synthesized and extruded through a microneedle by applied pressure. A cold plate was used as a substrate for deposition of the ink layer by layer and to freeze the ink in order to maintain the 3D structure. Once the complete structure was formed, the final structure was obtained by subsequent freeze-drying and sintering processes. Instead of using extrusion for depositing the ink, the inkjet method can deposit the ink with a very low concentration solution which can fabricate ultra-light and multifunctional aerogels, such as nano cellulose[35], MXene[36], and graphene composite[37].

The microstructure of 3D freeze printed objects can be manipulated by different freeze casting conditions, however, it's quite difficult to directly observe such process. Current approaches such as optical microscopy, computed tomography (CT) scan, or Scanning Electron Microscope (SEM) only provide indirect or partial observations. In order to observe the internal structure, the 3D freeze-printed samples need post-processing after printing. First, the 3D freeze-printed samples need to be stored at very low-temperature conditions (-30°C to -70°C) after printing. Then, they need to be freeze-dried to sublimate the ice, some metal or ceramic samples need an additional sintering process for consolidation. During the freeze-drying or sintering process, the internal structure may change due to shrinkage. Such observations are therefore indirect and cannot provide kinetic information such as the real size of ice crystals and their growth speed.

In recent years, X-ray synchrotron radiography has been used due to its in-situ, real-time, and direct observation features. Compared to the normal laboratory-based X-ray CT imaging, synchrotron-based X-ray has 3-5 orders of magnitude higher photon flux which allows for shorter imaging time. Therefore, in-situ X-ray imaging techniques have been used to investigate the process dynamics of several 3D printing processes including laser powder bed fusion[38-40], powder-blown laser-additive manufacturing[41], and binder jetting-additive manufacturing[41]. Since 3DFP is a hybrid process, understanding the relation between the substrate temperature and ice crystal growth mechanism is very crucial for printing quality.

In order to observe the ice crystals' growth behavior during the 3DFP process, we proposed a real-time x-ray imaging system that combined X-ray synchrotron-based radiography and the 3DFP technique. Due to the limited availabilities of the X-ray synchrotron facilities, equipment and materials, we performed our experiments in two separate stages. In the first stage,

we performed an initial experiment which focused on only freeze casting process, since the 3DPF is a hybrid process which combines the freeze casting and additive manufacturing techniques. We developed the method utilizing synchrotron-based radiography to observe the ice crystallization of HAP slurry under the freeze casting process. The ice crystal growth behavior was tracked during the unidirectional freeze casting process. This experiment, which required a relatively simple experimental setup and less control, was conducted at the Advanced Photon Source (APS) at Argonne National Laboratory. With the gained experience from the initial study, we further performed experiments for in-situ x-ray imaging of inkjet 3D freeze printing process in Stanford Synchrotron Radiation Lightsource (SSRL) at SLAC National Accelerator Laboratory. The inkjet deposition of colloidal silica was monitored by X-ray imaging during the 3DFP process. Considering the complexity of the experimental setup, achieving a remote control on the experimental setup required serious effort and time. With the advantages provided by the X-ray imaging techniques, we were able to observe the freezing front, deposited material, and growing ice crystals simultaneously.

4.2 System Design and Experiment Result

4.2.1 In-situ X-ray imaging of Freeze Casting process

(a) Material preparation

The material for freeze casting experiment was hydroxyapatite (HAP) slurry. It was prepared by mixing commercial HAP powders (d50=1-3 micrometer, Trans-Tech, Adamstown, MD) in deionized (DI) water at a concentration of 60 wt. %. Darvan C-N (Vanderbilt Minerals, Norwalk, CT) was added by 0.8 wt. % based on the HAP solid to disperse the HAP powder. The suspension was mixed homogeneously for 5 hours by magnetic stirring. Thereafter, hydroxypropyl methyl cellulose (H7509, Sigma-Aldrich, Saint Louis, MO), as a viscosifier, was

added by 9 mg/mL in the DI water, followed by stirring for 12 hours to dissolve fully. During this step, 1-octanol (112615, Sigma-Aldrich, Saint Louis, MO) was also added by 0.5 vol. % of the distilled water as a defoamer.

(b) X-ray synchrotron radiography and freeze casting setup

Synchrotron absorption micro-radiography measurements were performed at the beamline 2-BM of the Advanced Photon Source (APS) at Argonne National Laboratory. The schematic experiment setup is shown in Fig. 4-1. The x-ray beam at 2-BM is from a bending magnet source. 2-BM can operate in monochromatic beam mode in which X-ray energy is selectable between 10 and 45keV, pink beam mode in which there is only an X-ray mirror in the beam to cut off high-energy X-rays, and white beam mode in which there is no any X-ray optics in the beam[42]. In this study, we used pink beam mode with 1.5 mrad incident angle to the beamline mirror. The X-ray cut-off energy was about 45keV. A 1-mm carbon and 2-mm Si filters were used to reduce the low-energy x-rays. The X-ray beam delivered to the sample had its average energy around 35-40keV. The freeze casting equipment was placed in the middle of X-ray beam such that the transmitted beam reached the high-resolution imaging camera which was used to record the radiography images. The detector consisted of a 100-μm-thick LuAG:Ce scintillator, which converted the X-ray absorption signal into a visible light image. Then the image was magnified by a 2x Mitutoyo long-working distance optic lens and captured by a high-speed CMOS camera (Adimec Q-12A180, Woburn, MA). The image size was 3256 μm x 2200 μm, and the effective pixel size in the acquired images was 2.75 μm x 2.75 μm.

The schematics of the freeze casting setup are given in Fig. 4-1. As shown in Fig . 4-1a, the well mixed HAP slurry was loaded into a polymer mold with 10-mm length, 21-mm height, and 2-mm thickness. The mold was directly placed on the cold plate (TP294, Sigma Systems, El

Cajon, CA), which was set at a constant temperature of -30 °C. The controller of the cold plate used a proportional–integral–derivative (PID) algorithm to adjust heating power and cooling pumping flow to maintain the constant temperature. The liquid nitrogen cooling system was integrated with the cold plate, which is consisted of a pump, a Dewar, and a lid with a stoppered port for refilling during operation. Since there was only one temperature gradient which was along the vertical direction, the ice crystals only propagated along the vertical direction as the schematic shown in Fig. 4-1b. The x-ray beam was perpendicular with the freeze casting sample which left a rectangular region to be captured during the freeze casting process.

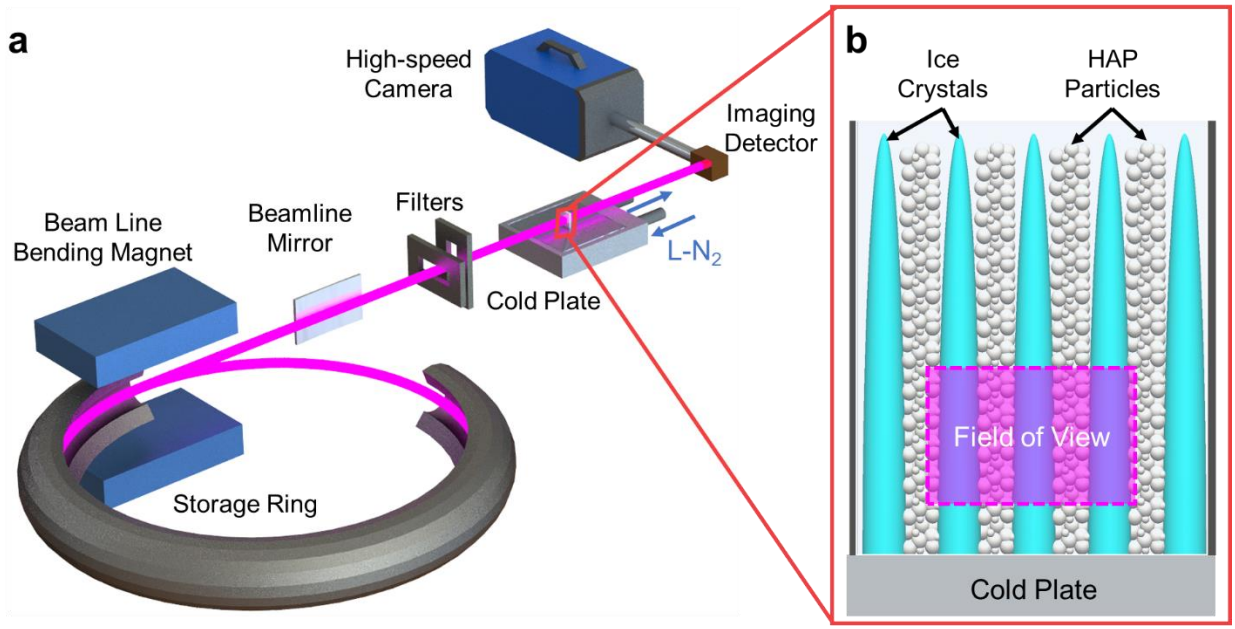

Figure 4-1 Schematic of X-ray and freeze casting setup. (a) Design of the freeze casting setup. (b) Growth of ice crystals along the temperature gradient in freeze casting process

(c) X-ray imaging results

In order to generate the unidirectional temperature gradients, the polymer mold was directly attached to the -30°C cold plate. The ice crystals only grew along the vertical direction, which is also the temperature gradient direction. Since the freezing speed was fast at the bottom

region and the field of view was limited, the images captured were located 7 mm above the top surface of the cold plate. The X-ray images of unidirectional freeze casting are shown in Fig. 4-2. Since the imaged region was smaller than the freezing sample, only part of the sample was able to be visualized (3.256 mm x 2.2 mm). We can see some circular objects (circles with black outlines) within the captured region, which are air bubbles. They were generated during slurry preparation and loading of the slurry to the plastic mold. Since the viscosity of the slurry was quite high, air bubbles were trapped and not easy to move. As the sample was continuously exposed to the x-ray, the size of some air bubbles expanded due to the heating effect which is marked by blue circles in Fig. 4-2a and 4-2b. We also noticed that the air bubble was able to be pushed by the propagating of ice front and combined with other air bubbles (as marked by yellow ellipses in Fig. 4-2b and 4-2c). This phenomenon can also result in the formation of larger air bubbles.

The ice front propagating along the temperature gradient (vertical direction) is shown in Fig. 4-2a - Fig. 4-2d. The ice front can be clearly identified during the freeze casting process. The unfrozen slurry is located above the ice front. Since the slurry was well mixed, no contrast can be identified within the unfrozen slurry. Below the ice front, the well-oriented and well-defined lamellar structures can be observed. These structures indicate the typical ice crystal growth during the unidirectional freeze casting process. Due to the unidirectional ice crystal growth, the HAP particles were pushed in between the growing ice crystals, which formed the lamellar structures. We also noticed that the ice crystals growing at the center part of the sample was faster than those growing at the boundary region (ice crystals are higher at the left side which can be observed in Fig. 4-2d). This phenomenon was due to the low conductivity of the mold, which generated certain heat effects to the slurry located at the boundary region.

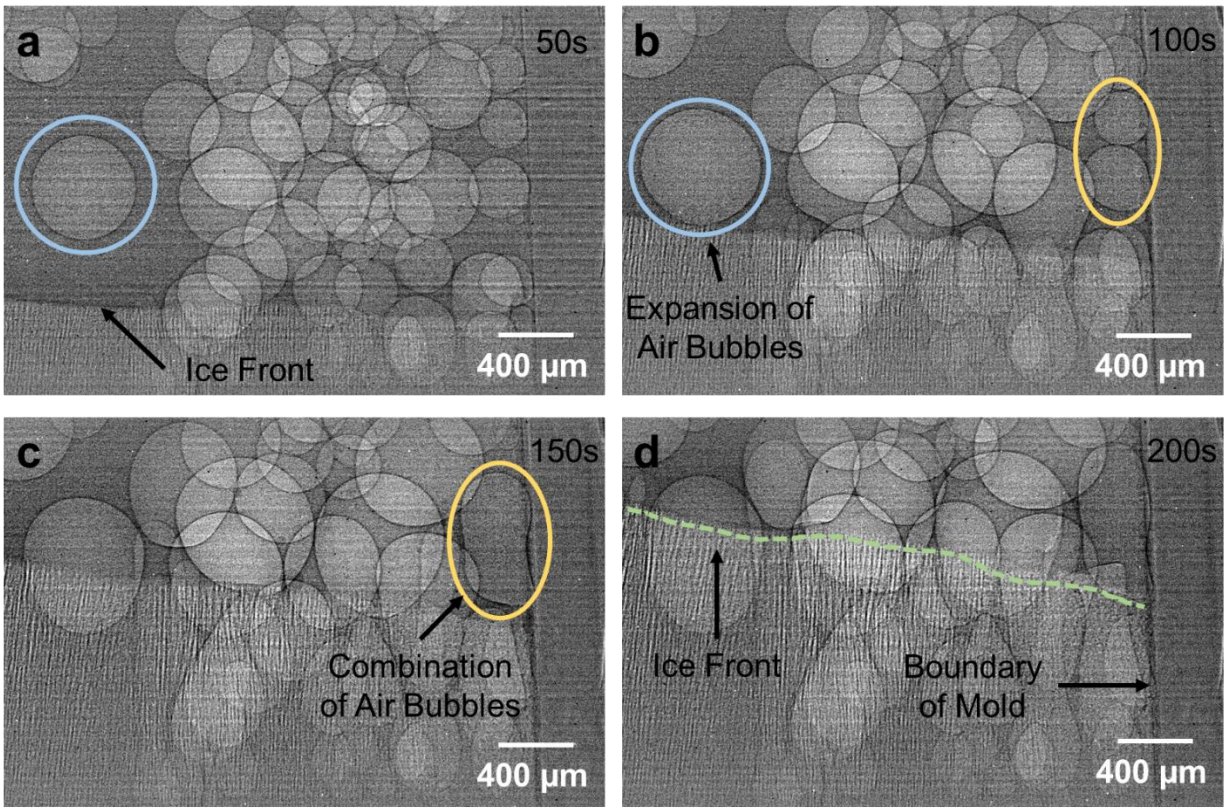

Figure 4-2 In-situ X-ray image sequences of unidirectional freeze casting. (a) Ice front under the unfrozen slurry. (b) Expansion of air bubbles. (c) Combination of air bubbles. (d) The growth of Ice crystals in different regions.

4.2.2 In-situ X-ray imaging of Inkjet 3DFP process

3DFP is a hybrid process based on drop-on-demand (DOD) inkjet printing and unidirectional freeze casting. Most commonly water-based, Newtonian inks with low-viscosity values are used as starting material. Using a commercial micro-dispenser (The Lee Co, CT, USA), spherical droplets are generated. For the satellite-free droplet formation, the pressure inside the syringe barrel on which the micro-dispenser is attached needs to be well-adjusted. For that purpose, a pneumatic fluid dispenser (Nordson EFD, RI, USA) is used. The spherical droplets are deposited onto a pre-cooled substrate by a liquid nitrogen operated cold plate

(Instec, CO, USA). After the impact of the droplets on the substrate, they immediately freeze and protect their shapes. As in the unidirectional freeze casting process, ice crystals nucleate on the substrate surface, and grow along the temperature gradient from bottom to top. The position and the velocity of the micro-dispenser are controlled by a customized 3-axis motion stage made from commercially available ball screw driven linear actuators (Panowin Technologies, Shanghai, China). By adjusting the distance and time lapse between successive droplets, coalescence of the droplets is achieved, and uniform lines are obtained. Depositing uniform lines layer-by-layer, frozen structures with complex 3D shapes are obtained. Following, to obtain the 3D printed aerogel, the frozen structure is freeze dried at -35° C and 0.2 mbar using a benchtop freeze dryer (Labconco, MO, USA) for at least 48 h. Freeze drying sublimates the ice crystal in the frozen structure and yields to aerogels whose porosity is a replica of the sublimated ice crystal. Depending on the nature of the material used in the ink formulation, further thermal or chemical treatments can be applied to enhance the integrity and/or provide the functionality to the 3D printed aerogel.

Since the 3DFP process requires post-printing processes such as freeze drying and thermal/chemical treatment (when required), investigation of final products thereafter the complete process does not provide quality information regarding the "3DFP" part of the process. To understand the effects of substrate temperature and deposition rate of the material on the quality of the printed lines, we prepared the setup provided in Fig. 4-3a and performed the in-situ investigation of the process using X-ray imaging techniques at bending magnet beamline 2−2 of Stanford Synchrotron Radiation Lightsource, SLAC National Accelerator Laboratory in CA, USA. More detailed information about the experimental setup and conclusions drawn from the experiments can be found elsewhere[43]. To be able to observe the solidification and material

deposition simultaneously, we used a commercially available colloidal silica suspension (15 wt. %) with an average particle size of 4−6 nm (Nyacol, MA, USA). We investigated separate droplets and uniform lines obtained after coalescence of separate droplets and tested different substrate temperature, inter-droplet distance and time lapse values to perform a systematic study for developing a fundamental understanding of the process dynamics. We further deposited three consecutive lines on top of each other to investigate the adhesion and the ice crystal growth mechanism along the successive layers (see Fig. 4-3b). To collect the X-ray images, we used a scintillator-based optical system with a 100-μm YAG:Ce scintillator crystal (Crytur Ltd.) coated in 120 nm of Al on the upstream side. A high reflectance mirror (Thorlabs) was used to bend the visible light 90˚ off-axis to the X-rays into a 4x long working distance infinity-corrected objective lens (Nikon), infinity-corrected tube lens (Thorlabs), and high-speed CMOS camera pco.dimax S4 (PCO). Using this optical setup, we obtained an effective pixel size of 2.4 μm for a field of view of 4.8 mm x 2.4 mm, and images were captured at 500 Hz. As presented in Fig. 4-4, we were able to observe the deposited material along with the ice (solidification) front simultaneously. This capability of in-situ X-ray imaging helped us to understand the effect of 3D printing parameters such as printing speed, material jetting frequency, and substrate temperature on the final product quality. Furthermore, with the help of the different x-ray absorptivity of silica and water (ice), we observed the growth of the ice crystals, which showed the freezing direction and interlayer fusion of the deposited material[43].

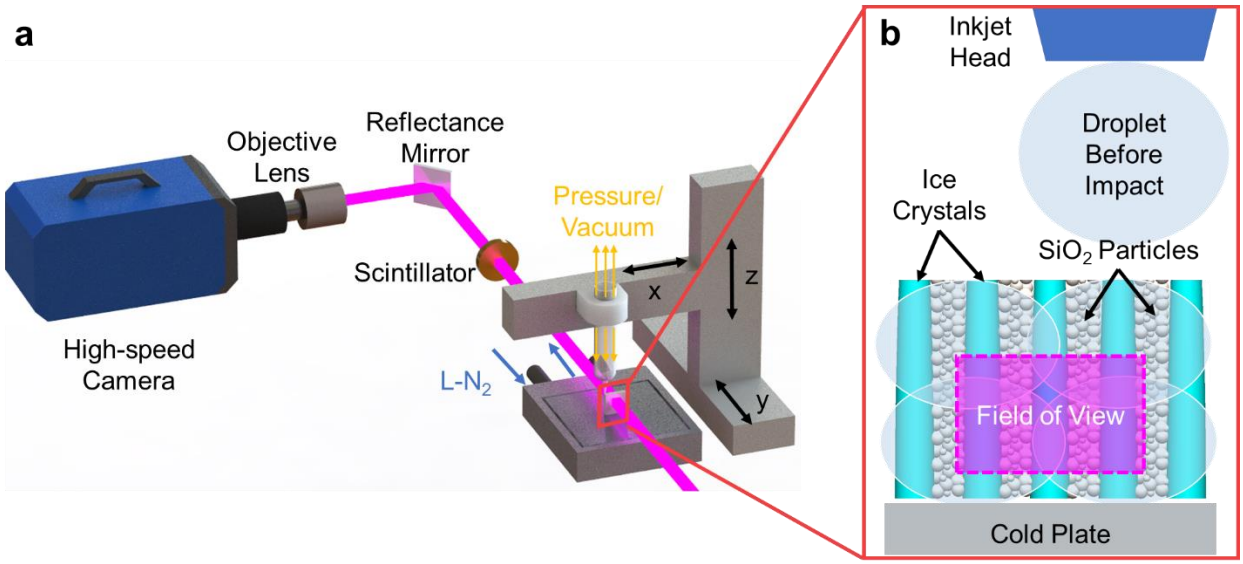

Figure 4-3 Schematic of X-ray and inkjet 3D Freeze Printing system setup. (a) Design of the Inkjet 3D freeze printing system. (b) Growth of ice crystals along the temperature gradient during inkjet 3DFP process.

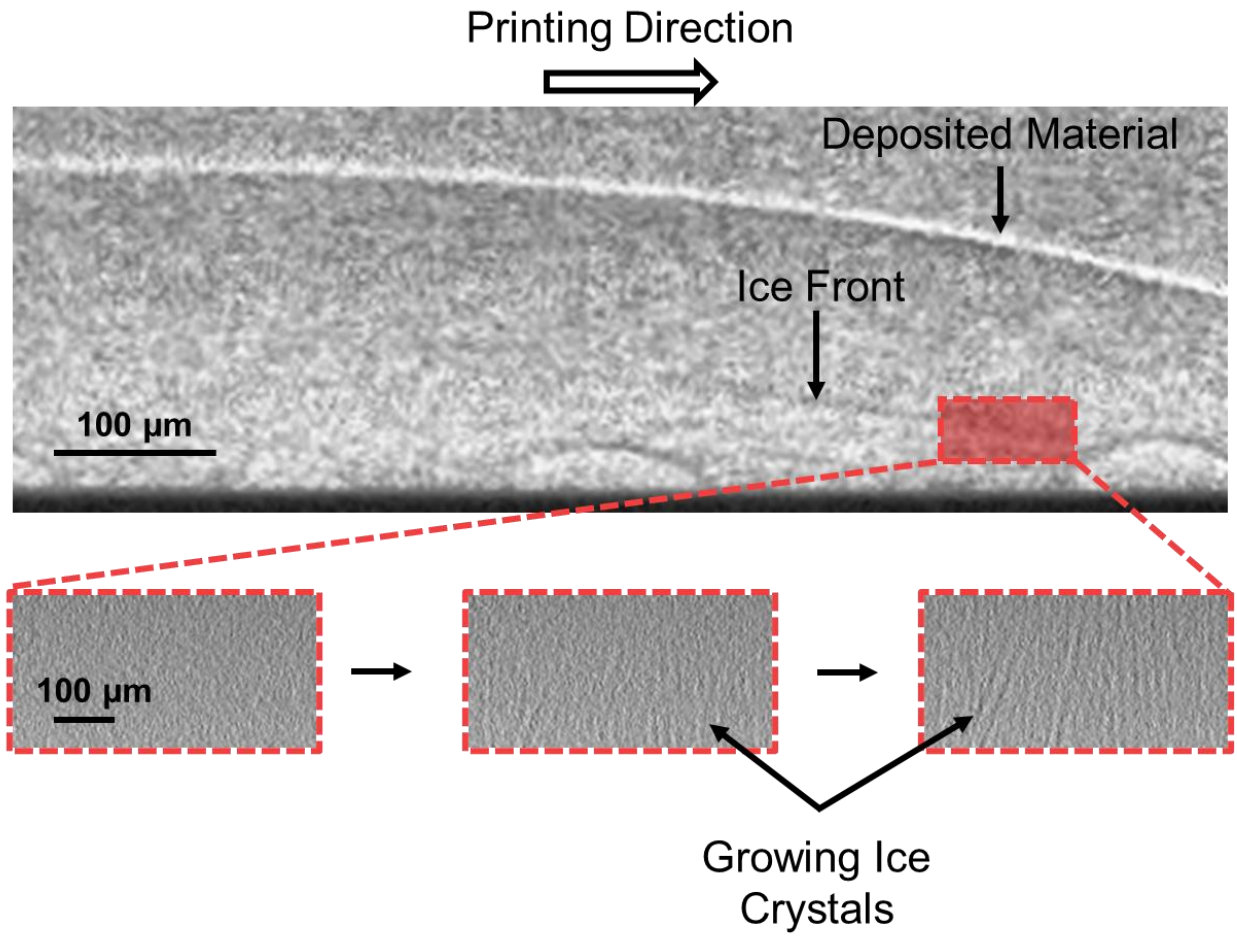

Figure 4-4 In-situ X-ray images of inkjet-based 3D freeze printing process showing the material deposition along with the ice front and growing ice crystals.

4.3 Conclusion

The water-to-ice phase transformation is probably one of the trickiest phenomena to investigate among solidification studies. The microstructural characteristics of freeze casting materials are determined by the morphology of the frozen fluid, which depends largely on the nature of the interactions between the particles within the suspension and the solid/liquid interface. As a result of the complex and interdependent relationships in the freeze casting process, material properties can vary widely even within similar systems. In addition, the 3D

Freeze Printing combines additive manufacturing and freeze casting processes, which enables the dynamic deposition of the material during the freeze casting, making the system even more complex. Therefore, a theoretical understanding is necessary to gain predictive control of such complex system.

In this study, we developed a method which utilizing in-situ X-ray synchrotron-based radiography to observe the freeze casting and 3DFP processes. The following conclusions are obtained from this study:

- The system we build provided a new method to in-situ observe the formation of internal structures during the freeze casting and 3DFP processes.
- The ice crystal growth with its unique, well-oriented, and well-defined lamellar structures can be observed during the freeze casting process.
- With the advantages provided by the rapid X-ray imaging, we were able to observe freeze front, deposited material, and growing ice crystals simultaneously during the inkjet 3DFP process.
- With the help of rapid X-ray synchrotron radiography/ tomography and the development of imaging techniques, we will be able to generate more fundamental understandings of the physics behind the 3D freeze printing process in the future.

Acknowledgement

This work is supported by the National Science Foundation (Award No. 1943445) and the NASA EPSCoR Cooperative Agreement Notice Grant (Award No. 80NSSC19M0153) and Johnson Cancer Center. This research used resources of the Advanced Photon Source (APS), a U.S. Department of Energy (DOE) Office of Science User Facility operated for the DOE Office of Science by Argonne National Laboratory under Contract No. DE-AC02-06CH11357. Use of

the Stanford Synchrotron Radiation Lightsource (SSRL), SLAC National Accelerator Laboratory, is supported by the U.S. Department of Energy, Office of Science, Office of Basic Energy Sciences under Contract No. DE-AC02-76SF00515.

References

[1] K. Araki, J.W.J.J.o.t.A.C.S. Halloran, New freeze‐casting technique for ceramics with sublimable vehicles, 87(10) (2004) 1859-1863.

[2] S.W. Sofie, F. Dogan, Freeze casting of aqueous alumina slurries with glycerol, Journal of the American Ceramic Society 84(7) (2001) 1459-1464.

[3] T. Waschkies, R. Oberacker, M.J. Hoffmann, Control of lamellae spacing during freeze casting of ceramics using double‐side cooling as a novel processing route, Journal of the American Ceramic Society 92 (2009) S79-S84.

[4] J. Han, C. Hong, X. Zhang, J. Du, W. Zhang, Highly porous ZrO2 ceramics fabricated by a camphene-based freeze-casting route: Microstructure and properties, Journal of the European Ceramic Society 30(1) (2010) 53-60.

[5] L. Hu, C.-A. Wang, Y. Huang, C. Sun, S. Lu, Z. Hu, Control of pore channel size during freeze casting of porous YSZ ceramics with unidirectionally aligned channels using different freezing temperatures, Journal of the European Ceramic Society 30(16) (2010) 3389-3396.

[6] H.-D. Jung, S.-W. Yook, H.-E. Kim, Y.-H. Koh, Fabrication of titanium scaffolds with porosity and pore size gradients by sequential freeze casting, Materials letters 17(63) (2009) 1545-1547.

[7] G. Gouws, N. Shortt, Microstructured silver surfaces produced by freeze casting for enhanced phase change heat transfer, Journal of Physics: Conference Series, IOP Publishing, 2015, p. 012045.

[8] F. Qian, P.C. Lan, M.C. Freyman, W. Chen, T. Kou, T.Y. Olson, C. Zhu, M.A. Worsley, E.B. Duoss, C.M. Spadaccini, Ultralight conductive silver nanowire aerogels, Nano letters 17(12) (2017) 7171-7176.

[9] Y. Tang, K.L. Yeo, Y. Chen, L.W. Yap, W. Xiong, W. Cheng, Ultralow-density copper nanowire aerogel monoliths with tunable mechanical and electrical properties, Journal of Materials Chemistry A 1(23) (2013) 6723-6726.

[10] A.I. Ramos, D.C. Dunand, Preparation and characterization of directionally freeze-cast copper foams, Metals 2(3) (2012) 265-273.

[11] C. Wang, X. Chen, B. Wang, M. Huang, B. Wang, Y. Jiang, R.S. Ruoff, Freeze-casting produces a graphene oxide aerogel with a radial and centrosymmetric structure, ACS nano 12(6) (2018) 5816-5825.

[12] W. Gao, N. Zhao, W. Yao, Z. Xu, H. Bai, C. Gao, Effect of flake size on the mechanical properties of graphene aerogels prepared by freeze casting, RSC advances 7(53) (2017) 33600-33605.

[13] J. Bai, Y. Huang, Q. Gong, X. Liu, Y. Li, J. Gan, M. Zhao, Y. Shao, D. Zhuang, J. Liang, Preparation of porous carbon nanotube/carbon composite spheres and their adsorption properties, Carbon 137 (2018) 493-501.

[14] B. Wicklein, A. Kocjan, G. Salazar-Alvarez, F. Carosio, G. Camino, M. Antonietti, L. Bergström, Thermally insulating and fire-retardant lightweight anisotropic foams based on nanocellulose and graphene oxide, Nature nanotechnology 10(3) (2015) 277.

[15] P.K. Sahoo, N. Kumar, S. Thiyagarajan, D. Thakur, H.S. Panda, Freeze-Casting of multifunctional cellular 3D-graphene/Ag nanocomposites: synergistically affect supercapacitor, catalytic, and antibacterial properties, ACS Sustainable Chemistry & Engineering 6(6) (2018) 7475-7487.

[16] S.M.H. Ghazanfari, A. Zamanian, Phase transformation, microstructural and mechanical properties of hydroxyapatite/alumina nanocomposite scaffolds produced by freeze casting, Ceramics International 39(8) (2013) 9835-9844.

[17] W. Li, K. Lu, J.Y. Walz, Formation, Structure and Properties of Freeze‐Cast Kaolinite–Silica Nanocomposites, Journal of the American Ceramic Society 94(4) (2011) 1256-1264.

[18] C.-C. Ji, M.-W. Xu, S.-J. Bao, C.-J. Cai, Z.-J. Lu, H. Chai, F. Yang, H. Wei, Self-assembly of three-dimensional interconnected graphene-based aerogels and its application in supercapacitors, Journal of colloid and interface science 407 (2013) 416-424.

[19] P. Zuo, W. Zhang, J. Hua, Y. Ma, C. Du, X. Cheng, Y. Gao, G. Yin, A novel one-dimensional reduced graphene oxide/sulfur nanoscroll material and its application in lithium sulfur batteries, Electrochimica Acta 222 (2016) 1861-1869.

[20] C. Stolze, T. Janoschka, S. Flauder, F.A. Müller, M.D. Hager, U.S. Schubert, Investigation of ice-templated porous electrodes for application in organic batteries, ACS applied materials & interfaces 8(36) (2016) 23614-23623.

[21] C. Suwanchawalit, A.J. Patil, R.K. Kumar, S. Wongnawa, S. Mann, Fabrication of ice-templated macroporous TiO 2–chitosan scaffolds for photocatalytic applications, Journal of Materials Chemistry 19(44) (2009) 8478-8483.

[22] M. Barrow, A. Eltmimi, A. Ahmed, P. Myers, H. Zhang, Frozen polymerization for aligned porous structures with enhanced mechanical stability, conductivity, and as stationary phase for HPLC, Journal of Materials Chemistry 22(23) (2012) 11615-11620.

[23] J. Kuang, L. Liu, Y. Gao, D. Zhou, Z. Chen, B. Han, Z. Zhang, A hierarchically structured graphene foam and its potential as a large-scale strain-gauge sensor, Nanoscale 5(24) (2013) 12171-12177.

[24] C. Hou, H. Wang, Q. Zhang, Y. Li, M. Zhu, Highly conductive, flexible, and compressible all‐graphene passive electronic skin for sensing human touch, Advanced Materials 26(29) (2014) 5018-5024.

[25] J. Kuang, Z. Dai, L. Liu, Z. Yang, M. Jin, Z. Zhang, Synergistic effects from graphene and carbon nanotubes endow ordered hierarchical structure foams with a combination of compressibility, super-elasticity and stability and potential application as pressure sensors, Nanoscale 7(20) (2015) 9252-9260.

[26] J.J. Campbell, A. Husmann, R.D. Hume, C.J. Watson, R.E. Cameron, Development of three-dimensional collagen scaffolds with controlled architecture for cell migration studies using breast cancer cell lines, Biomaterials 114 (2017) 34-43.

[27] Y. Zhu, K. Song, S. Jiang, J. Chen, L. Tang, S. Li, J. Fan, Y. Wang, J. Zhao, T. Liu, Numerical simulation of mass transfer and three-dimensional fabrication of tissue-engineered cartilages based on chitosan/gelatin hybrid hydrogel scaffold in a rotating bioreactor, Applied biochemistry and biotechnology 181(1) (2017) 250-266.

[28] T. Fukasawa, M. Ando, T. Ohji, S. Kanzaki, Synthesis of porous ceramics with complex pore structure by freeze‐dry processing, Journal of the American Ceramic Society 84(1) (2001) 230-232.

[29] S. Deville, Freeze‐casting of porous ceramics: a review of current achievements and issues, Advanced Engineering Materials 10(3) (2008) 155-169.

[30] M. Naviroj, S. Miller, P. Colombo, K. Faber, Directionally aligned macroporous SiOC via freeze casting of preceramic polymers, Journal of the European Ceramic Society 35(8) (2015) 2225-2232.

[31] A. Macchetta, I.G. Turner, C.R. Bowen, Fabrication of HA/TCP scaffolds with a graded and porous structure using a camphene-based freeze-casting method, Acta Biomaterialia 5(4) (2009) 1319-1327.

[32] R. Dash, Y. Li, A.J. Ragauskas, Cellulose nanowhisker foams by freeze casting, Carbohydrate polymers 88(2) (2012) 789-792.

[33] X. Song, H. Tetik, T. Jirakittsonthon, P. Parandoush, G. Yang, D. Lee, S. Ryu, S. Lei, M.L. Weiss, D.J.A.E.M. Lin, Biomimetic 3D printing of hierarchical and interconnected porous hydroxyapatite structures with high mechanical strength for bone cell culture, 21(1) (2019) 1800678.

[34] A. Dasyam, B. Sharma, G. Yang, D. Lin, S. Lei, Design and 3D Printing of Aerogel-based Ultra-lightweight Sound Absorbers, INTER-NOISE and NOISE-CON Congress and Conference Proceedings, Institute of Noise Control Engineering, 2020, pp. 309-314.

[35] H. Tetik, K. Zhao, N. Shah, D. Lin, 3D freeze-printed cellulose-based aerogels: Obtaining truly 3D shapes, and functionalization with cross-linking and conductive additives, Journal of Manufacturing Processes 68 (2021) 445-453.

[36] J. Orangi, H. Tetik, P. Parandoush, E. Kayali, D. Lin, M. Beidaghi, Conductive and highly compressible MXene aerogels with ordered microstructures as high-capacity electrodes for Li-ion capacitors, Materials Today Advances 9 (2021) 100135.

[37] E. Brown, P. Yan, H. Tekik, A. Elangovan, J. Wang, D. Lin, J. Li, 3D printing of hybrid MoS2-graphene aerogels as highly porous electrode materials for sodium ion battery anodes, Materials & Design 170 (2019) 107689.

[38] N.P. Calta, J. Wang, A.M. Kiss, A.A. Martin, P.J. Depond, G.M. Guss, V. Thampy, A.Y. Fong, J.N. Weker, K.H. Stone, An instrument for in situ time-resolved X-ray imaging and

diffraction of laser powder bed fusion additive manufacturing processes, Review of Scientific Instruments 89(5) (2018) 055101.

[39] C. Zhao, K. Fezzaa, R.W. Cunningham, H. Wen, F. De Carlo, L. Chen, A.D. Rollett, T. Sun, Real-time monitoring of laser powder bed fusion process using high-speed X-ray imaging and diffraction, Scientific reports 7(1) (2017) 1-11.

[40] N.D. Parab, C. Zhao, R. Cunningham, L.I. Escano, K. Fezzaa, W. Everhart, A.D. Rollett, L. Chen, T. Sun, Ultrafast X-ray imaging of laser–metal additive manufacturing processes, Journal of synchrotron radiation 25(5) (2018) 1467-1477.

[41] S.J. Wolff, H. Wu, N. Parab, C. Zhao, K.F. Ehmann, T. Sun, J. Cao, In-situ high-speed X-ray imaging of piezo-driven directed energy deposition additive manufacturing, Scientific reports 9(1) (2019) 1-14.

[42] Y. Wang, F. De Carlo, D.C. Mancini, I. McNulty, B. Tieman, J. Bresnahan, I. Foster, J. Insley, P. Lane, G. von Laszewski, A high-throughput x-ray microtomography system at the Advanced Photon Source, Review of Scientific Instruments 72(4) (2001) 2062-2068.

[43] H. Tetik, G. Yang, W. Tan, A. Fong, S. Lei, J.N. Weker, D. Lin, High Speed In-situ X-ray Imaging of 3D Freeze Printing of Aerogels, Additive Manufacturing 36 (2020) 101513.

Chapter 5 - 3D Freeze Printing of Nano-Cellulose Aerogel

Paper title:

Sustainable Multifunctionality: Bio-inspired Printing of Nanocellulose Aerogel Acoustical Materials

Submitted in:

Advanced Materials Technologies

Authors' names:

Guang Yang[1], Amulya Lomte[2], Bhisham Sharma[3], Shuting Lei[1], Dong Lin[4]

Authors' affiliations:

1. Department of Industrial and Manufacturing Systems Engineering, Kansas State University, Manhattan, KS 66506, USA
2. Department of Aerospace Engineering, Wichita State University, Wichita, KS, 67260, USA
3. Mechanical Engineering-Engineering Mechanics, Michigan Technological University, Houghton, MI 49931, USA
4. School of Mechanical, Industrial & Manufacturing Engineering, Oregon State University, Corvallis, OR 97331, USA

Abstract

We demonstrate the three-dimensional freeze printing (3DFP) of nanocellulose aerogels with large-scale aligned pore orientations as a sustainable alternative to current acoustical materials. In contrast with the unidirectional pore network orientations obtained from current 3DFP techniques, we achieve a bidirectional orientation by using an inhomogeneous printing substrate to alter the thermal gradient within the print volume. The microstructural morphology shows that bidirectional printing results in a two-dimensional pore orientation, with comparatively thinner pore walls and larger pore widths. Acoustic measurements reveal that altering the pore network characteristics significantly affects the acoustical behavior of the printed CNC aerogels; the wider pores allow the bidirectional CNC aerogels to provide higher sound absorption performance at lower frequencies than the unidirectional samples. Notably, both 3D Freeze printed CNC aerogels provide substantially higher sound transmission loss performance as compared to current acoustical materials. The unidirectional pore structure results in CNC aerogels with higher stiffness and improved energy absorption performance, with both 3D freeze printed CNC aerogels outperforming other CNC aerogel materials in their stiffness-to-density ratios. The ability to simultaneously control their pore orientation and macrostructural geometry paves the way for printing complex shaped CNC aerogel structures for multifunctional noise control applications.

Keywords

3D freeze printing, nanocellulose, noise control, bidirectional pore orientation, multifunctional materials

5.1 Introduction

Noise pollution is a pressing societal concern, both for human health and the environment. Health effects stemming from daily noise exposure include hearing loss and

tinnitus [1], [1] sleep disturbance [2], heightened stress [3], mental health disorders [4], cardiovascular diseases [5], and impaired cognitive development in children [6]. According to a World Health Organization summary report [7], daily noise exposure results in an annual loss of at least one million healthy life years. Excessive noise is also an ecological concern [8]: it jeopardizes habitats, interferes with wildlife communication, shifts predatory-prey dynamics, and alters long established migration routes. These concerns are reflected in the increasingly stringent noise regulations and certification requirements being issued by regulatory bodies throughout the world [9].

Current noise abatement technologies can be classified into active and passive systems. Active noise reduction systems use electronic methods to cancel noise by generating sound waves with an inverted phase relative to the unwanted waves [10]. Such systems are highly effective for attenuating noise with narrow banded frequency profiles; however, their constant power supply requirement limits their use for applications requiring energy and cost efficiency. Therefore, passive noise control methods continue to be the predominant method for most applications. Passive techniques may be further subclassified into reactive and resistive systems [11]. Reactive systems, such as automotive silences, bass traps, and duct mufflers, rely on the energy losses occurring due to Helmholtz resonances or impedance discontinuities to attenuate sound waves. On the other hand, resistive systems are primarily comprised of porous materials that absorb incident sound waves by dissipating their acoustic energy via viscous and thermal losses [12]. This loss mechanism, coupled with their easier implementation and lower operational costs, makes them the preferred noise control solution for a majority of applications. However, state-of-the-art porous materials [13], such as acoustic foams and glass fiber sheets, offer low mechanical stiffness and are highly compliant. This compliance limits their use for

structural applications and makes it difficult to accurately characterize their acoustical properties - unintentional compression or aeration can skew the measured impedances and transport properties [14]. The traditional methods used to manufacture these materials cause additional uncertainties: they result in a stochastic pore architecture, which introduces batch-to-batch property variations and restricts the deliberate engineering of pore shapes to attain optimal performance for targeted uses [15]. Currently, acoustic foams are predominantly made from polyurethane or other synthetic polymers that are derived from fossil fuels. The flammability characteristics of such materials preclude their use for high temperature applications typically encountered in aerospace and other engineering domains. Their manufacturing processes often involve chemicals and processes that are harmful to the environment. Importantly, these materials are not biodegradable and can be difficult to recycle-their durability allows them to persist in landfills for many years after their disposal.

Cellulose, found in plant cell walls and among the earth's most abundantly available biopolymers, is a potential sustainable alternative [16]. Historically used in the production of paper and textiles, the recent necessity for sustainability has spurred researchers to explore the use of cellulose-based materials for a broader range of applications [17]. However, their broader engineering use is hindered by their limited durability and uniformity. The advent of nanocellulose provides a way to overcome these barriers by introducing superior characteristics, such as improved mechanical stiffness, decreased thermal expansion, and lower density [18]. Notably, recent research shows that deriving aerogels using nanocellulose can provide unique combinations of ultralow density and exceptional mechanical properties [19]. Consequently, nanocellulose aerogels are a subject of growing research interest across diverse fields, including their use in energy storage devices [20], thermal insulation materials [21], and biomedical

scaffolds [22]. Similar to other aerogels, nanocellulose aerogels are currently fabricated using either supercritical drying or freeze-drying to avoid surface tension issues damaging the solid pore network [19]; the specific process choice typically depends on the material and application requirements. While both processes result in aerogels with stochastic pore networks, their network can be more precisely controlled using the freeze-drying method by preceding the drying step with freeze-casting or ice-templating [23], wherein the aerogel precursor's colloidal suspension is frozen under controlled thermal conditions into the desired macrostructural shape using a thermally insulated mold. As the suspension freezes, the precursor molecules infiltrate the gaps between the growing solvent crystals, creating a densely packed pore network whose structural characteristics are governed by the surrounding thermal conditions [24]. The solvent ice crystals are then sublimated during the subsequent freeze-drying step to obtain the desired porous microstructure. This technique has been used to produce aerogels from ceramics [23, 25], metals [26], polymers [27], and carbon nanomaterials [28].

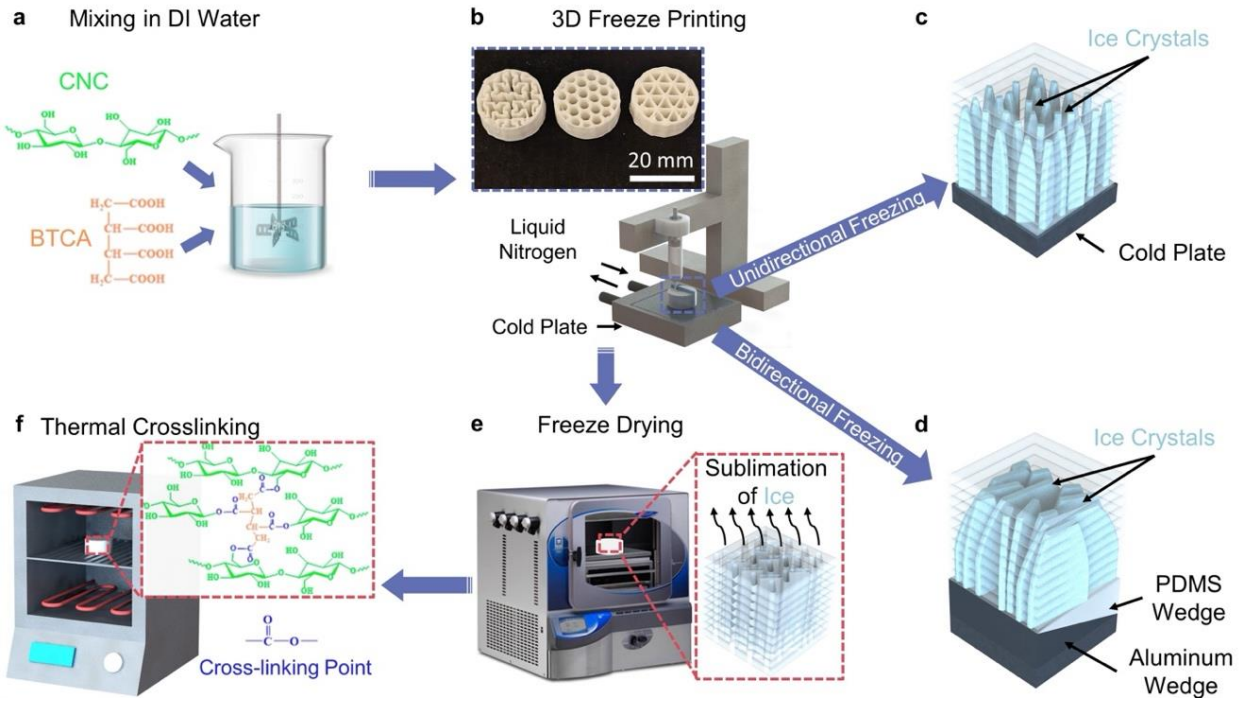

Figure 5-1 Schematic of the 3D Freeze Printing(3DFP) and post processing. a) Ink preparation. b) 3DFP setup. c) Unidirectional freezing setup. d) Bidirectional freezing setup. e) Freeze-drying process. f) Crosslinking process.

The requirement of a mold to obtain the desired macrostructural geometries constrains the feasibility of using freeze-casting to fabricate complex three-dimensional aerogel structures. Our recent efforts show that this mold constraint can be eliminated by combining freeze-casting with extrusion-based additive manufacturing, termed three-dimensional freeze printing (3DFP) [24,19]. As illustrated in Figure 5-1, in 3DFP, the aerogel ink is extruded from a printing nozzle and deposited layer-by-layer onto a chilled print bed with precisely controlled temperature (from -180°C-120°C). As the ink is deposited on the cold print bed, the solvent crystallizes, allowing the precursor molecules to create a densely packed pore network by infiltrating the gaps between the growing crystals [24]. During the subsequent freeze-drying step, the solvent crystals are sublimated, and the precursor molecules thermally crosslink to form the final aerogel with the desired macrostructure. Similar to other extrusion-based 3D printing processes, this method allows the fabrication of complex macrostructural geometries without the constraints associated with a traditional molding process, as shown in Figure 5-1b insert. For aerogel structures fabricated using 3DFP, the pore network characteristics are determined by the solvent ice crystal growth dynamics and the resultant inter-crystal gap geometry [30]. As depicted in Figure 5-1c, in traditional 3DFP, the use of a uniform flat plate results in a unidirectional thermal gradient orthogonal to the print bed, restricting the crystal align along the vertical direction and resulting in a corresponding unidirectional pore network. In this method, the pore widths can be controlled by controlling the temperature gradient of the uniform print bed. However, our unidirectional freeze casting based printing is limited to aligning pores solely in the orthogonal direction. This

limitation in controlling pore orientation hinders the capability of fabricating aerogel architectures with optimized microporous network properties s for application-specific characteristics.

Here, we overcome this limitation and demonstrate the fabrication of CNC aerogels with a two-dimensional, laminated pore orientation control for multifunctional noise reduction applications. We achieve this by replacing the uniform print bed with a print substrate that combines a polydimethylsiloxane (PDMS) and an aluminum wedge to provide a directional thermal gradient within the print volume, consequently controlling the pore orientation along two directions. As depicted in Figure 5-1e, we position the flat surface of the aluminum wedge directly on the cold plate and then attach a PDMS wedge to the top surface; both wedges are identical in size and are connected along a 20 degree wedge angle to ensure a horizontal print bed. The significant disparity between the thermal conductivities of the aluminum wedge (239 Wm-1K-1) and the PDMS wedge (0.15 Wm-1K-1) generates an additional thermal gradient along the horizontal direction. This bidirectional thermal gradient alters the previously vertical orientation of the ice crystals and consequently results in CNC aerogels with a bidirectional pore network [30]. Our results show that such bidirectional CNC aerogels provide vastly superior sound absorption and transmission loss properties as compared to current acoustical materials used for noise reduction applications. Further, we show that CNC aerogels fabricated using unidirectional and bidirectional 3DFP provide better mechanical and functional properties than those fabricated using other methods. Thus, the presented method provides a novel route toward engineering sustainable and multifunctional noise reduction solutions for advanced applications.

5.2 Results and Discussion

The differences between the overall pore structure of samples fabricated using unidirectional and bidirectional 3DFP can be seen in the scanning electron microscopy (SEM) images shown in Figure 5-2. In addition to the differences in the pore alignment, as seen from Figures 5-2b and 5-2f, altering the temperature gradient orientation also affects the wall thickness and pore widths. Overall, as measured over a 12.5 mm sample area, bidirectional printing results in thinner walls with a tighter wall thickness distribution (Figure 5-2d) as compared to the unidirectionally printed sample. As expected, this reduction in wall thickness is associated with an enlargement in the open pore widths of the bidirectional sample (Figure 5-2h). The average pore width-reflecting the spacing between the adjacent ice crystals-of the bidirectional samples is 62 µm while that of the unidirectional samples is 31 µm.

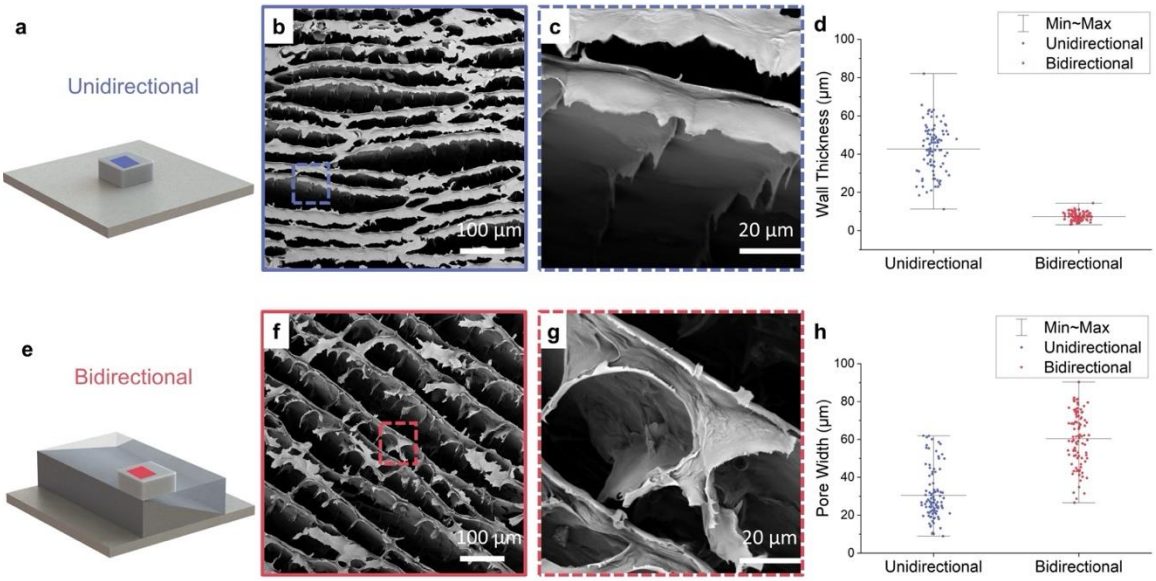

Figure 5-2 Scanning electron microscopy (SEM) images of 3D freeze printed samples. a) Schematics of unidirectional freeze casting setup. b)-c) Top views of aerogels under unidirectional freeze casting. d) Wall thickness of the aerogels. e) Schematics of bidirectional

freeze casting setup. f)-g) Top views of aerogels under bidirectional freeze casting. h) Pore width of the aerogels.

The underlying pore network of open-celled porous materials controls their sound absorption performance [12]. As sound waves travel through a porous material the incident acoustic energy gets absorbed due to the frictional and thermal losses occurring at the fluid-solid interfaces within the pore channels. The amount of energy dissipated is thus intrinsically dependent on the geometrical parameters of the pore network-notably the pore width, orientation, and network tortuosity. The sound absorption coefficients of rigidly backed unidirectional and bidirectional CNC aerogel samples of 12.7 mm thickness under normal incidence conditions are compared in Figure 5-3b. The measurements are performed over a frequency range from 600 Hz to 6100 Hz using the 2-microphone normal incidence impedance tube technique, as prescribed by ASTM E1050-19. The results are obtained by averaging the sound absorption measurements performed for four different samples of each type. Measurements labeled side A are performed with the bottom surface-i.e., the surface in contact with the print plate-facing the incident waves while side B refers to the top surface of the sample. The two sides of the test samples are shown in Figure 5-3a.

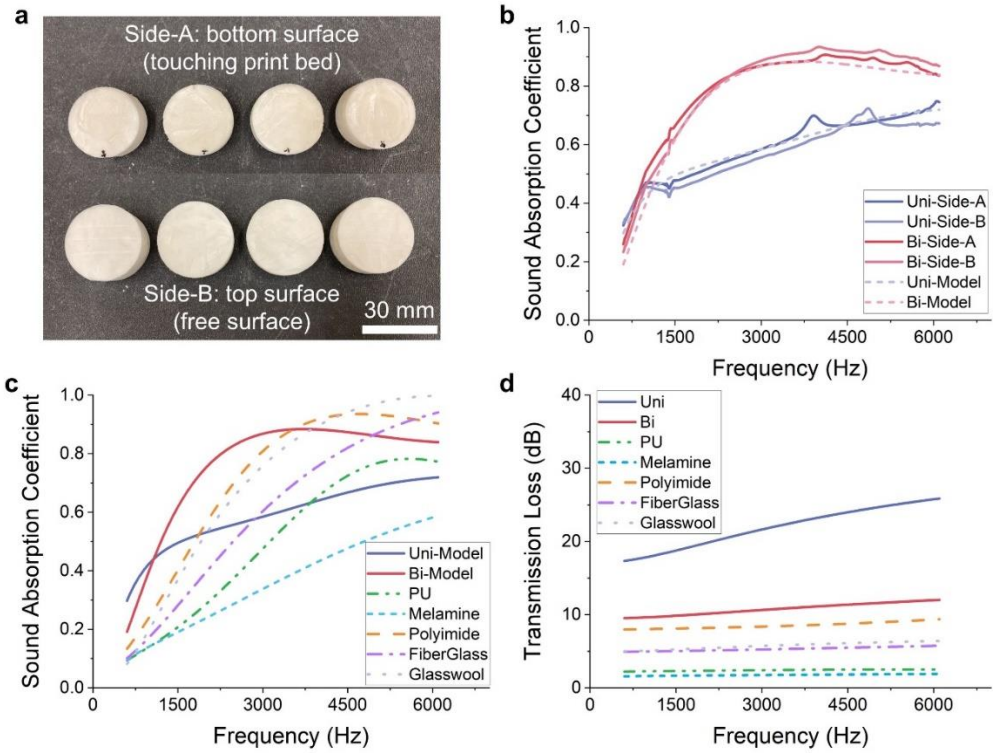

Figure 5-3 Acoustical characteristics of unidirectional and bidirectional CNC aerogels and their comparison with other acoustical materials. a) Test samples used characterization showing the two different sides of each sample. b) Comparison of the sound absorption measurement of the unidirectional and bidirectional samples. The measured data are represented using solid lines while the absorptions predicted by the inverse characterization approach are represented using dashed lines. c) Comparison of the sound absorption coefficients of the 3D freeze printed CNC aerogels with other acoustical materials. d) Comparison of the sound transmission loss curves of the 3D freeze printed CNC aerogels with other acoustical materials.

The absorption measurements show that the differences in the pore structure of the unidirectional and bidirectional samples result in markedly different sound absorption performance over the measurement range. While both absorbers provide broadband performance reminiscent of other resistive porous materials [31], the bidirectional pore structure significantly

improves the absorption coefficient, absorbing more than 60% of the incident acoustic energy for all frequencies above 1500 Hz. Further, minimal differences are observed between the two sides of each sample, indicating the through-thickness uniformity of the 3D printed samples. Note that the observed differences are within the uncertainty bounds of the test procedure and the sample-to-sample property variations observed for sound absorbers printed using other additive techniques [14, 15].

Table 5 - 1 **.** Acoustical transport parameters estimated by the inverse characterization approach.

CNC Aerogel Type	**Porosity**	**Resistivity [Ns/m^4]**	**Tortuosity**	**Viscous Characteristic Length [μm]**	**Thermal Characteristic Length [μm]**
Unidirectional	99%	390,287	4.309	37.4	37.4
Bidirectional	99%	126,274	2.89	68.1	68.1

The differences in the pore structure and its effect on the overall acoustical performance are further quantified by extracting the relevant acoustic transport parameters using an inverse characterization approach [32]. Here, we model both absorbers as acoustically rigid using the Johnson-Champoux-Allard-Lafarge (JCAL) formulation [12, 32]. The estimated acoustic transport properties are provided in Table 5-1. The accuracy of the model is verified by comparing the predicted and measured sound absorption curves in Figure 5-3b. Both predictions (dashed lines) match the measured data (solid lines), establishing the validity of the JCAL formulation for modeling the acoustical behavior of 3D printed CNC aerogel materials. As expected from the SEM observations, the thicker cell walls and narrower average pore width of

the unidirectional samples results in a comparatively higher static airflow resistivity and lower viscous and thermal characteristics lengths. The estimated viscous and thermal characteristic lengths-strongly correlated to the pore and throat diameters [12, 32], respectively, and the dominant parameters controlling the visco-thermal effects at medium and high acoustical frequencies-compare well with the pore width distributions obtained from the SEM characterization (Figure 5-2h). Further, the inverse characterization predicts that the unidirectional thermal gradient results in a more tortuous pore network. A higher tortuosity typically improves the sound absorption performance by increasing the path length traversed by the sound waves. However, the lower sound absorption of the unidirectionally printed samples suggests that their smaller pore width results in an excessively high airflow resistance, resulting in reflecting the incident sound waves rather than absorbing them.

Figures 5-3c and 5-3d compare the predicted normal incidence sound absorption and transmission loss properties of the unidirectional and bidirectional CNC aerogel samples with the predicted properties of 12.7 mm thick samples of other widely used acoustical materials [12, 32, 33]: polyurethane, melamine, polyimide, fiberglass, and glass wool. Figure 5-3c shows that both 3D printed CNC aerogels provide better sound absorption performance than the current acoustical materials at frequencies below 2000 Hz, with the bidirectional CNC aerogel providing the highest absorption until approximately 3000 Hz. Further, Figure 5-3d shows that both CNC aerogels significantly outperform all the other materials in their sound transmission loss performance. Notably, the unidirectional pore network results in transmission loss that is more than 200% higher at lower frequencies and more than 300% higher at higher frequencies as compared to the polyimide sample of the same thickness. The differences between the transmission loss properties of the bidirectional and unidirectional samples are in line with the

previous observations indicating that the narrowed pore widths of the unidirectional CNC aerogels result in higher reflection, reducing the acoustic energy absorbed by the material while increasing the transmission loss.

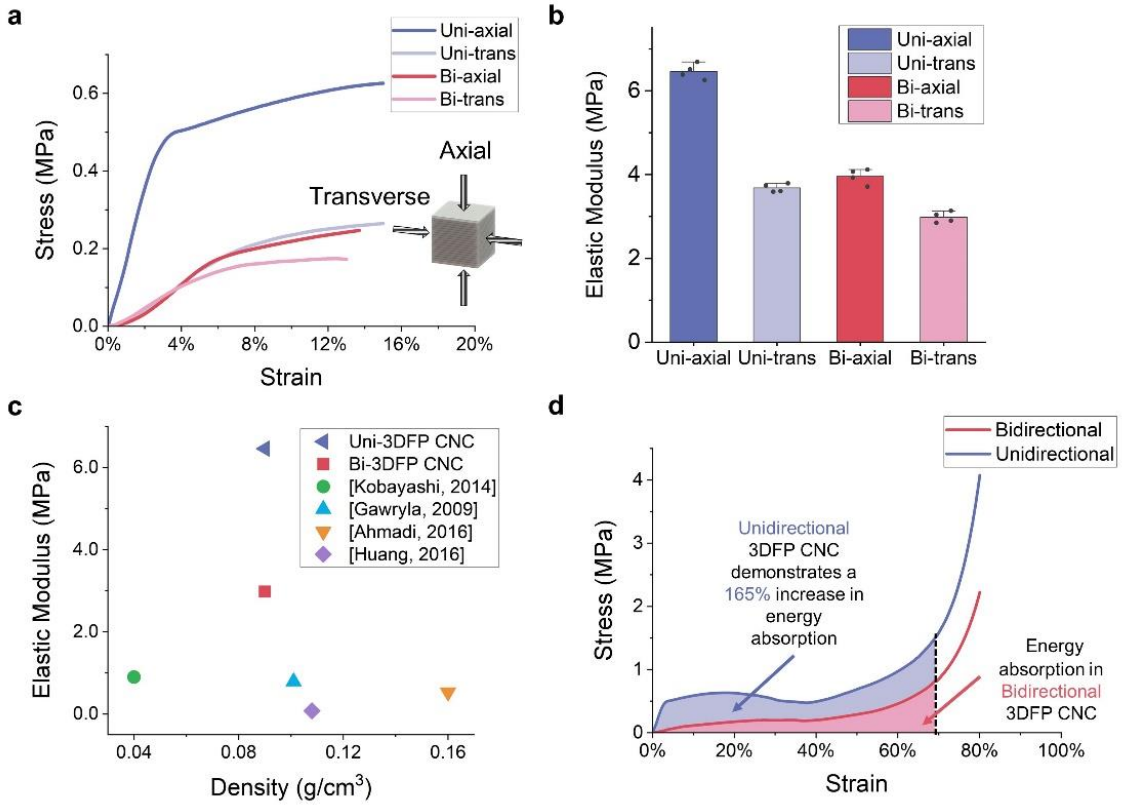

Figure 5-4 Mechanical properties of the CNC aerogel. a) Comparison of stress-strain behavior of unidirectional and bidirectional CNC aerogels under uniaxial and biaxial compressive loading. b) Comparison of their elastic moduli from the stress-strain curves. c) Property map of elastic modulus versus density for CNC based aerogels. d) Comparison of the energy absorption behavior of unidirectional and bidirectional CNC aerogels at low strain rates.

The pore network differences between the unidirectional and bidirectional CNC aerogels also influences their mechanical stiffness properties [34]. Figure 5-4a compares their stress-strain curves when subjected to compression between two parallel plates using a universal testing machine. The testing was conducted by centering cubic samples on the lower stationary plate and

compressing them at a constant rate of 1 $mm.min^{-1}$ using the upper parallel plate. Using the cubic samples allows application of the load along the parallel (axial) and perpendicular (transverse) directions with respect to the freezing direction. As expected, altering the temperature gradient during printing drastically changes the mechanical performance of the resulting CNC aerogels. The vertical cell wall orientation of unidirectional samples allows them to resist a significantly higher amount of stress as compared to the bidirectional samples when compressed axially, i.e., parallel to the cell wall direction. When loaded along the transverse direction, though the initial stress-strain behavior of both samples is similar, the bidirectional sample yields at a lower stress. Interestingly, both samples exhibit a sharper transition from the elastic to the plastic regime under axial loading as compared to the gradual transition observed under transverse loading. Calculating the elastic modulus using the linear regime of the stress-strain curves shows that unidirectional printing results in CNC aerogels that are stiffer along the axial as well as transverse directions. Notably, due to the uniaxial orientation of their pore walls along the loading direction, the unidirectional sample exhibits an axial elastic modulus approximately 45% higher than the bidirectional sample. Figure 5-4c compares the elastic moduli of the unidirectional and bidirectional 3D printed CNC aerogels with other previously reported CNC aerogel-based materials as a function of their mass density [23c, 35]. It can be seen that the controlled pore structure of the unidirectional and bidirectional CNC aerogels results in significantly higher stiffness-to-density ratios, with both materials outperforming other CNC aerogels.

The energy absorption performance of the unidirectional and bidirectional aerogels at low strain-rates are compared in Figure 5-4d. Overall, both materials display stress-strain profiles typically observed for porous materials [34]: the materials initially deform linear elastically,

followed by a stress plateau region with large strain increments, eventually densifying and displaying a sharp increase in the stress. The higher yield stress of the unidirectional aerogels results in a higher plateau stress and a flatter plateau stress profile. Comparatively, their bidirectional orientation and narrower pore wall thickness results in a more gradual pore channel collapse, resulting in a plateau stress profile where the stress is slowly increasing with increasing strain values until the neighboring pore walls come into contact and the sample begins densifying. The larger pore widths of the bidirectional CNC aerogels result in a higher densification strain as compared to the unidirectional CNC aerogels. Overall, the higher plateau stress of the unidirectional CNC aerogels provides approximately 165% higher energy absorption as compared to the bidirectional aerogels, where the energy absorption is calculated as the area under the individual curves until the densification strain.

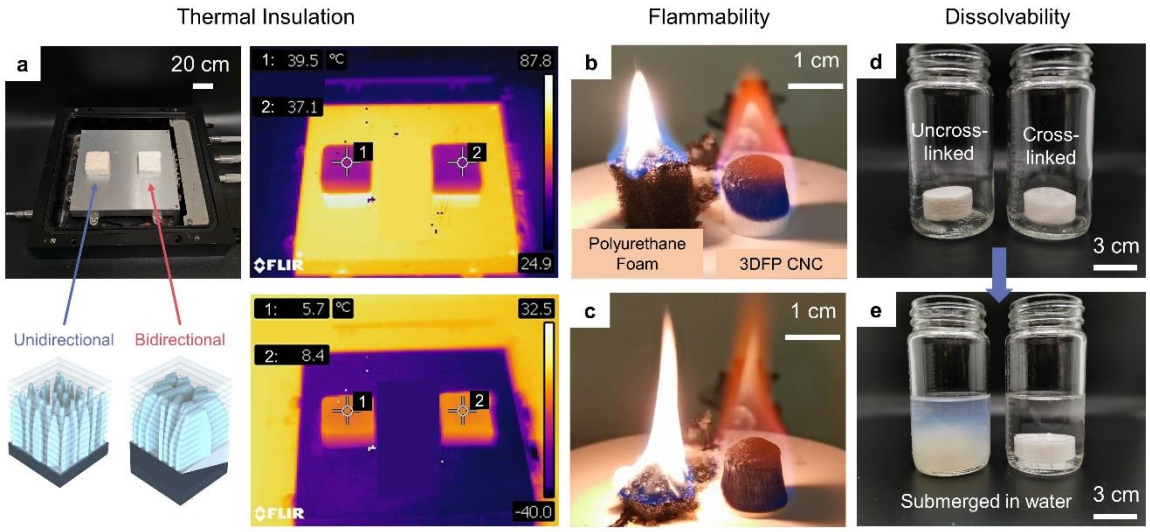

Figure 5-5 Multifunctional performance of 3D Freeze printed CNC aerogels. a) Comparison of thermal insulation abilities of unidirectional and bidirectional CNC aerogels. b-c) Flammability comparison of unidirectional CNC aerogel with polyurethane foam. d-e) Dissolvability comparison of crosslinked and un-crosslinked CNC aerogels.

Figure 5-5 demonstrates the other exceptional functionalities of CNC aerogels that make them a potential solution to applications under challenging environments. Figure 5-5a illustrates the thermal insulation behavior of the unidirectional and bidirectional CNC aerogels under high and low temperature conditions. Samples with identical dimensions (20 mm length, 20 mm width, and 10 mm height) are placed on a hot/cold plate and the thermal conditions are monitored using a thermal imaging camera. As the temperature of the plate is increased to approximately 88°C, the upper surface of the unidirectional samples reaches 39.5°C while the bidirectional sample reaches approximately 37°C. Similarly, when the plate temperature is reduced to -40°C, the upper surfaces of the unidirectional and bidirectional sample reach 5.7°C and 8.4°C, respectively. Thus, while further in-depth investigations are necessary, these results indicate that similar to other high porosity aerogels [36], the 3D freeze printed CNC aerogels exhibit desirable thermal insulation properties, which may be tuned by controlling the pore directionality. Figures 5-5b and 5-5c compare the flammability of a unidirectional CNC aerogel sample with that of a polyurethane acoustic foam sample. As both samples are ignited simultaneously, the CNC aerogel proved considerably more resistant to ignition than the polyurethane foam. Additionally, the polyurethane foam exhibited a more vigorous combustion and burnt at a faster rate as compared to the CNC aerogel sample. Figures 5-5d and 5-5e compare the dissolvability of un-crosslinked and crosslinked unidirectional CNC aerogels. When the aerogels are submerged in water without stirring, the un-crosslinked aerogel quickly dissolves, whereas the crosslinked aerogel effectively maintains its structure. This demonstrates the crosslinked CNC aerogel's potential to withstand high humidity environments without structural failure. The above results show that 3D freeze printed CNC aerogels with controlled

pore network properties are a highly attractive sustainable solution for the design of multifunctional noise reduction technologies.

5.3 Conclusion

We have demonstrated the 3D freeze printing of CNC aerogels with tailorable pore orientations for multifunctional noise reduction applications. The orientation of the microporous network was controlled by replacing the uniform print bed with a flat print substrate composed of PDMS and aluminum wedges. In contrast with the unidirectional temperature gradient in a conventional 3DFP setup, the difference in the thermal conductivities of these two materials creates a bidirectional temperature gradient, which consequently results in a bidirectional pore orientation. Two-microphone, normal incidence acoustic impedance tube testing reveals that the bidirectional CNC aerogels provide higher sound absorption in the low- to medium-frequency regimes as compared to the unidirectional samples. The impedance measurements were used to model the acoustical properties of the porous CNC aerogels using the JCAL formulation. The model predictions show that the 3D freeze printed CNC aerogels outperform the currently used acoustical materials in their sound absorption and transmission loss properties. Notably, the unidirectional CNC aerogels provide more than 200% higher sound transmission loss over the 600 Hz to 6100 Hz range as compared to the polyimide sample of the same thickness. Mechanical testing shows that the pore orientation also affects the effective elastic stiffness and energy absorption properties. Overall, the unidirectional pore network results in a stiffer material and provides greater energy absorption. Similar to their noise reduction capabilities, the 3D freeze printed CNC aerogels demonstrate better stiffness-to-density ratios as compared to other CNC aerogels described in existing literature. Our results show that altering the thermal gradient within the print volume allows the 3D freeze printing of CNC aerogels whose pore orientations,

and thus their pore dependent functional and mechanical properties, can be controlled to achieve optimal, application-specific property combinations. This study establishes a foundation for the development of sustainable porous materials featuring controlled microporous networks and intricate macrostructural shapes suitable for multifunctional noise reduction applications.

5.4 Experimental Section/Methods

Aerogel Fabrication

Ink preparation: The crosslinker, 1,2,3,4-Butanetetracarboxylic acid (Sigma-Aldrich, Saint Louis, MO), was initially added at a concentration of 1 $mg.mL^{-1}$ to deionized (DI) water. This was followed by 30 minutes of magnetic stirring at 350 rpm until it completely dissolved. Subsequently, commercial CNC powders (CelluForce, Montreal, Canada) were gradually added to the solution at a concentration of 15 wt.%. The ink was then homogenized using a high shear probe homogenizer (T18 basic, Ultra Turrax, IKA Works Inc., Wilmington, NC, USA) at 6,000 rpm until it became uniform. Finally, the ink underwent additional magnetic stirring at 100 rpm for another 24 hours to ensure stability. Prior to 3D freeze printing (3DFP), the CNC ink was subjected to a vacuum mixer to reduce air bubbles for 90 seconds. After vacuum mixing, the CNC ink was transferred to a 30 mL syringe for the printing process.

Extrusion: To facilitate the 3D freeze printing (3DFP) process, a commercial CNC milling machine was adapted by replacing its milling modules with a custom-made syringe pump. This syringe pump, driven by a step motor, was seamlessly integrated with the CNC controller to enable continuous ink extrusion. The ink was methodically extruded onto a cold plate (Instec, CO, USA), layer by layer, to construct a three-dimensional structure.

During 3DFP, the cold plate's temperature was meticulously controlled, initially set at 0°C and then steadily reduced at a constant rate of 10°C per minute until reaching -70°C. This temperature

regulation was achieved using a proportional integral derivative (PID) algorithm within the cold plate controller, which adjusted the heating power and cooling pump flow to maintain the desired cooling rate. A liquid nitrogen cooling system, essential for this process, was fully integrated with the cold plate. This system comprised a pump, a Dewar, and a lid equipped with a stoppered port for nitrogen refilling during operation.

In unidirectional freeze casting, the ink was deposited onto a flat cold plate. As illustrated in Figure 5-1c, this method resulted in ice crystals propagating solely in the vertical direction, owing to the unidirectional temperature gradient. During bidirectional freeze casting, the homogeneous aluminum plate was replaced by a PDMS wedge and an aluminum wedge, each with a 20° angle and identical dimensions (90 mm length, 50 mm width, and 18.2 mm height), assembled onto a thick plate (see Figure 5-1d). In this setup, the aluminum wedge was placed at the bottom, directly affixed to the cold plate, with the PDMS wedge positioned on top. The ink was then extruded onto the PDMS wedge's top surface, enabling bidirectional freeze casting.

Post-Processing: The frozen samples were then moved to a -75°C freezer and kept for 12 hours for further freezing. Next, the samples were loaded into a freeze dry system (Labconco, Kansas City, MO) at -35°C under 200mbar vacuum to fully sublimate ice for the duration of 72 hours. Then the temperature of the freeze dryer was adjusted to 25°C and kept it under 200mbar vacuum for another 1 hour. This step was to avoid the condensation of water vapor from the air on the aerogel surface. Finally, the cross-linked CNC aerogels were obtained by a thermal treatment at 120°C for 3 hours following the freeze-drying process.

Scanning Electron Microscopy

The microstructure of the CNC aerogel was characterized by scanning electron microscopy (SEM) (Phenom Pharos Desktop SEM system). The samples were attached to SEM sample holders

with conductive double-side tape and sputter-coated with a thin layer of gold prior to SEM. The accelerating voltage was set at 15 kV during SEM imaging. The captured images were then analyzed using ImageJ.

Acoustic Characterization

Normal Incidence Impedance Tube Testing: The sound absorption coefficient of the 3D printed aerogel samples was determined using a normal incidence two-microphone impedance tube. This measurement process adhered to the ASTM standard E1050-19 guidelines. The setup involved a loudspeaker, powered by an amplifier, positioned at one end of the tube to produce white noise across a frequency spectrum from DC to 10 kHz. Within the tube, which had a diameter of 30 mm, two microphones were placed 22.5 mm apart. These microphones were responsible for measuring the plane wave pressure fields over a frequency range of 600 to 6100 Hz. The data collected from these two microphones enabled the calculation of the transfer function, denoted as H_{12}. The transfer function was defined as the ratio of the pressures measured at the second microphone to that at the reference microphone. Subsequently, the reflection coefficient (R) and the sound absorption coefficient (α) were calculated as:

$$R = \frac{e^{-jks} + H_{12}}{H_{12} - e^{-jks}} e^{-2jk(l+s)} \quad (1)$$

$$\alpha = 1 - |R|^2 \quad (2)$$

where k is the wavenumber, s and l are the microphone spacing, and the distance between the front surface of the sample and its nearest microphone respectively, and j is the imaginary number given by $\sqrt{-1}$. All the tests were conducted at a sound pressure level of 90 dB.

Inverse Characterization: The acoustical transport properties of the unidirectional and bidirectional CNC aerogels were estimated using the inverse characterization approach. [32] This method involves a curve-fitting approach to estimate the acoustical transport properties that

provide the best fit with the measured sound absorption curves. The 3D freeze printed CNC aerogels were modeled as rigid porous materials using the Johnson-Champoux-Allard-Lafarge (JCAL) formulation which requires the determination of five transport parameters for modeling the acoustical behavior. [12, 32] The five transport parameters are: porosity, static airflow resistivity, tortuosity, viscous characteristic length, and thermal characteristic length. The inverse characterization method was implemented using the commercial software package, FOAM-X. The obtained transport properties were then used to predict the sound transmission loss of the sample. The properties of the other acoustical materials were obtained using previously obtained data. [33]

Mechanical Characterization: Compression tests were conducted using a Shimadzu Universal Testing Machine, to conduct compressive tests on our samples. The tests were conducted using cubic samples with sides of length 10 mm. The testing process involved placing each sample at the center of the machine's lower stationary plate. Above it, a top plate was positioned, which then moved downwards at a constant speed of $1mm.min^{-1}$, applying compressive force to the sample. This setup ensured that the compression was evenly distributed across the sample. To accurately capture the behavior of the samples under compression, data collection was conducted at a high frequency of 100Hz. The elastic modulus was calculated from the slopes of the obtained stress-strain curves. Similarly, the energy absorption was calculated as the area under the respective stress-strain curves until the densification strain is achieved.

Acknowledgement

Financial support from the National Science Foundation (Award No. 1943445) and the NASA EPSCoR Cooperative Agreement Notice Grant (Award No. 80NSSC19M0153 and 80NSSC22M0221) is gratefully acknowledged. Bhisham Sharma would like to acknowledge Ola Khaleel, Amrutha Dasyam, and Esmeralda Sanchez-Torres for assistance with acoustic testing.

References

[1] A. Baigi, A. Oden, V. Almlid-Larsen, M.-L. Barrenäs, K.-M. Holgers, *Ear and Hearing* **2011**, 32, 787.

[2] K. I. Hume, M. Brink, M. Basner, *Noise and Health* **2012**, 14, 297.

[3] W. Passchier-Vermeer, W. F. Passchier, *Environmental health perspectives* **2000**, 108, 123.

[4] S. Stansfeld, M. Haines, M. Burr, B. Berry, P. Lercher, *Noise and Health* **2000**, 2, 1.

[5] a)K. Sivakumaran, J. A. Ritonja, H. Waseem, L. AlShenaibar, E. Morgan, S. A. Ahmadi, A. Denning, D. S. Michaud, R. L. Morgan, *Noise & Health* **2022**, 24, 107; b)T. Münzel, T. Gori, W. Babisch, M. Basner, *European Heart Journal* **2014**, 35, 829.

[6] a)B. Roberts, R. L. Neitzel, *The Journal of the Acoustical Society of America* **2019**, 146, 3922; b)G. W. Evans, P. Lercher, M. Meis, H. Ising, W. W. Kofler, *The Journal of the Acoustical Society of America* **2001**, 109, 1023.

[7] W. H. Organization, *Burden of disease from environmental noise: Quantification of healthy life years lost in Europe*, World Health Organization. Regional Office for Europe, **2011**.

[8] G. Shannon, M. F. McKenna, L. M. Angeloni, K. R. Crooks, K. M. Fristrup, E. Brown, K. A. Warner, M. D. Nelson, C. White, J. Briggs, *Biological Reviews* **2016**, 91, 982.

[9] a)B. L. Johnson, M. Y. Lichtveld, *Environmental policy and public health*, CRC Press, **2017**; b)D. Jarosińska, M.-È. Héroux, P. Wilkhu, J. Creswick, J. Verbeek, J. Wothge, E. Paunović, *International Journal of Environmental Research and Public Health* **2018**, 15, 813.

[10] a)L. Lu, K.-L. Yin, R. C. de Lamare, Z. Zheng, Y. Yu, X. Yang, B. Chen, *Signal Processing* **2021**, 183, 108039; b)L. Lu, K.-L. Yin, R. C. de Lamare, Z. Zheng, Y. Yu, X. Yang, B. Chen, *Signal Processing* **2021**, 181, 107929.

[11] a)M. J. Crocker, F. M. Kessler, A. J. Price, *Noise and Noise Control: Volume 1*, Crc Press, **2018**; b)I. L. Vér, L. L. Beranek, *Noise and vibration control engineering: principles and applications*, John Wiley & Sons, **2005**.

[12] J. Allard, N. Atalla, *Propagation of sound in porous media: modelling sound absorbing materials*, John Wiley & Sons, **2009**.

[13] a)Y. Tao, M. Ren, H. Zhang, T. Peijs, *Applied Materials Today* **2021**, 24, 101141; b)S. Kishore, R. Sujithra, B. Dhatreyi, *Materials Today: Proceedings* **2021**, 47, 4700.

[14] B. G. Neto, I. Pereira, S. Futatsugi, E. Brandão, P. H. Mareze, W. Fonseca, presented at *INTER-NOISE 2018 - 47th International Congress and Exposition on Noise Control Engineering: Impact of Noise Control Engineering*, **2018**.

[15] H. S. Seddeq, *Australian Journal of Basic and Applied Sciences* **2009**, 3, 4610.

[16] G. Patterson, *Carbohydrate Polymers* **2021**, 252, 117182.

[17] a)X. Wang, C. Yao, F. Wang, Z. Li, *Small* **2017**, 13, 1702240; b)J. Wang, L. Wang, D. J. Gardner, S. M. Shaler, Z. Cai, *Cellulose* **2021**, 28, 4511; c)Y.-Y. Li, B. Wang, M.-G. Ma, B. Wang, *International Journal of Polymer Science* **2018**, 2018; d)A. Kausar, S. T. Zohra, S. Ijaz, M. Iqbal, J. Iqbal, I. Bibi, S. Nouren, N. El Messaoudi, A. Nazir, *International Journal of Biological Macromolecules* **2023**, 224, 1337; e)S. Kalia, A. Dufresne, B. M. Cherian, B. S. Kaith, L. Avérous, J. Njuguna, E. Nassiopoulos, *International Journal of Polymer Science* **2011**, 2011.

[18] a)D. Trache, A. F. Tarchoun, M. Derradji, T. S. Hamidon, N. Masruchin, N. Brosse, M. H. Hussin, *Frontiers in Chemistry* **2020**, 8, 392; b)A. Dufresne, *Materials Today* **2013**, 16, 220; c)T. Abitbol, A. Rivkin, Y. Cao, Y. Nevo, E. Abraham, T. Ben-Shalom, S. Lapidot, O. Shoseyov, *Current Opinion in Biotechnology* **2016**, 39, 76.

[19] Y. Chen, L. Zhang, Y. Yang, B. Pang, W. Xu, G. Duan, S. Jiang, K. Zhang, *Advanced Materials* **2021**, 33, 2005569.

[20] a)X. Yang, K. Shi, I. Zhitomirsky, E. D. Cranston, *Advanced Materials* **2015**, 27, 6104; b)M. Hamedi, E. Karabulut, A. Marais, A. Herland, G. Nyström, L. Wågberg, *Angewandte Chemie International Edition* **2013**, 52, 12038.

[21] a)D. Bendahou, A. Bendahou, B. Seantier, Y. Grohens, H. Kaddami, *Industrial Crops and Products* **2015**, 65, 374; b)B. Seantier, D. Bendahou, A. Bendahou, Y. Grohens, H. Kaddami, *Carbohydrate Polymers* **2016**, 138, 335.

[22] a)J. Fu, S. Wang, C. He, Z. Lu, J. Huang, Z. Chen, *Carbohydrate polymers* **2016**, 147, 89; b)H. Abdul Khalil, A. Adnan, E. B. Yahya, N. Olaiya, S. Safrida, M. S. Hossain, V. Balakrishnan, D. A. Gopakumar, C. Abdullah, A. Oyekanmi, *Polymers* **2020**, 12, 1759.

[23] a)S. Deville, *Advanced Engineering Materials* **2008**, 10, 155; b)A. E. Donius, A. Liu, L. A. Berglund, U. G. Wegst, *Journal of the Mechanical Behavior of Biomedical Materials* **2014**, 37, 88; c)X. Zhang, M. Liu, H. Wang, N. Yan, Z. Cai, Y. Yu, *Carbohydrate Polymers* **2019**, 208, 232.

[24] G. Yang, H. Tetik, J. N. Weker, X. Xiao, S. Lei, D. Lin, *Review of Scientific Instruments* **2022**, 93.

[25] a)G. Zu, J. Shen, L. Zou, W. Wang, Y. Lian, Z. Zhang, A. Du, *Chemistry of Materials* **2013**, 25, 4757; b)C. Ferraro, E. Garcia-Tuñon, V. G. Rocha, S. Barg, M. D. Fariñas, T. E. G. Alvarez-Arenas, G. Sernicola, F. Giuliani, E. Saiz, *Advanced Functional Materials* **2016**, 26, 1636; c)X. Xu, Q. Zhang, M. Hao, Y. Hu, Z. Lin, L. Peng, T. Wang, X. Ren, C. Wang, Z. Zhao, *Science* **2019**, 363, 723.

[26] a)Y. Tang, S. Gong, Y. Chen, L. W. Yap, W. Cheng, *ACS Nano* **2014**, 8, 5707; b)F. Qian, P. C. Lan, M. C. Freyman, W. Chen, T. Kou, T. Y. Olson, C. Zhu, M. A. Worsley, E. B. Duoss, C. M. Spadaccini, *Nano Letters* **2017**, 17, 7171; c)F. Qian, A. Troksa, T. M. Fears, M. H. Nielsen, A. J. Nelson, T. F. Baumann, S. O. Kucheyev, T. Y.-J. Han, M. Bagge-Hansen, *Nano Letters* **2019**, 20, 131.

[27] a)Z.-Z. Pan, H. Nishihara, S. Iwamura, T. Sekiguchi, A. Sato, A. Isogai, F. Kang, T. Kyotani, Q.-H. Yang, *ACS Nano* **2016**, 10, 10689; b)F. Deuber, S. Mousavi, L. Federer, M. Hofer, C. Adlhart, *ACS Applied Materials & Interfaces* **2018**, 10, 9069; c)K. Yin, P. Divakar, U. G. Wegst, *Acta Biomaterialia* **2019**, 84, 231.

[28] a)Z. He, J. Liu, Y. Qiao, C. M. Li, T. T. Y. Tan, *Nano Letters* **2012**, 12, 4738; b)S. Barg, F. M. Perez, N. Ni, P. do Vale Pereira, R. C. Maher, E. Garcia-Tunon, S. Eslava, S. Agnoli, C. Mattevi, E. Saiz, *Nature Communications* **2014**, 5, 4328; c)J. Kim, N. M. Han, J. Kim, J. Lee, J.-K. Kim, S. Jeon, *ACS Applied Materials & Interfaces* **2018**, 10, 37507.

[29] a)X. Song, H. Tetik, T. Jirakittsonthon, P. Parandoush, G. Yang, D. Lee, S. Ryu, S. Lei, M. L. Weiss, D. Lin, *Advanced Engineering Materials* **2019**, 21, 1800678; b)E. Brown, P. Yan, H. Tekik, A. Elangovan, J. Wang, D. Lin, J. Li, *Materials & Design* **2019**, 170, 107689; c)H. Tetik, J. Orangi, G. Yang, K. Zhao, S. B. Mujib, G. Singh, M. Beidaghi, D. Lin, *Advanced Materials* **2022**, 34, 2104980.

[30] G. Yang, F. Li, J. Xiao, H. Tetik, N. Shah, X. Xiao, J. Li, Y. Liao, S. Lei, W. Tan, *Ceramics International* **2021**, 47, 12234.

[31] a)L. Cao, Q. Fu, Y. Si, B. Ding, J. Yu, *Composites Communications* **2018**, 10, 25; b)T. Yang, L. Hu, X. Xiong, M. Petrů, M. T. Noman, R. Mishra, J. Militký, *Sustainability* **2020**, 12, 8477.

[32] Y. Atalla, R. Panneton, *Canadian Acoustics* **2005**, 33, 11.

[33] D. T. Wevita Vidanalage Dona, Wichita State University, 2020.

[34] M. F. Ashby, *Philosophical Transactions of the Royal Society A: Mathematical, Physical and Engineering Sciences* **2006**, 364, 15.

[35] a)Y. Kobayashi, T. Saito, A. Isogai, *Angewandte Chemie International Edition* **2014**, 53, 10394; b)M. D. Gawryla, O. van den Berg, C. Weder, D. A. Schiraldi, *Journal of Materials Chemistry* **2009**, 19, 2118; c)M. Ahmadi, A. Madadlou, A. A. Saboury, *Food Chemistry* **2016**, 196, 1016.

[36] a)S. Ahankari, P. Paliwal, A. Subhedar, H. Kargarzadeh, *ACS nano* **2021**, 15, 3849; b)S. Sen, A. Singh, C. Bera, S. Roy, K. Kailasam, *Cellulose* **2022**, 29, 4805; c)M. Koebel, A. Rigacci, P. Achard, *Journal of Sol-Gel Science and Technology* **2012**, 63, 315.

Chapter 6 - 3D Printing of Ceramics

Paper title:

Extrusion-based Additive Manufacturing of Zirconium Carbide for Nuclear Fuel Cell Structures

To be submitted to:

Ceramics International

Authors' names:

Guang Yang[1], Yuhui Xiang[2], Thomas Poirier[3], Tiankai Yao[4], Nikhil Churi[5], Brian Taylor[6], Narges Malmir[1] James H. Edgar[3] Dong Lin[2], Shuting Lei[1]

Authors' affiliations:

1. Department of Industrial and Manufacturing Systems Engineering, Kansas State University, Manhattan, KS 66506, USA
2. School of Mechanical, Industrial, and Manufacturing Engineering, Oregon State University, Corvallis, OR 97331, USA
3. Tim Taylor Department of Chemical Engineering, Kansas State University, Manhattan, KS 66506, USA
4. Idaho National Laboratory, Idaho Falls, ID 83415, USA
5. Woodbury School of Business, Utah Valley University, Orem, UT 84058, USA
6. NASA Marshall Space Flight Center, Advanced Propulsion Systems, Huntsville, AL 35808, USA

Abstract

Nuclear thermal propulsion relies on heating hydrogen propellant using nuclear fuel to generate thrust for spacecraft propulsion, with ceramic fuel elements like zirconium carbide (ZrC) offering advantages over metals due to their high melting points and stability. ZrC 's use as a matrix material in nuclear fuel pellets is well-established, although handling radioactive materials poses challenges. Vanadium carbide (VC), a nonradioactive surrogate with similar properties, has emerged for research purposes. Recent advancements include utilizing VC as a sintering additive for ZrC, enhancing densification and mechanical properties. Traditional ZrC fabrication methods struggle with intricate geometries, but additive manufacturing (AM), specifically extrusion-based methods, revolutionizes ceramic fabrication. Extrusion AM offers material flexibility, multi-material printing, minimal waste, and rapid prototyping. This study explores extrusion-based AM for ZrC nuclear fuel cell structures. Experimental findings highlight the impact of Nano Crystalline Cellulose (NCC) and VC additives on 3D-printed ZrC ceramics, with higher NCC concentrations improving ink recovery and reducing deformation but excessive NCC leading to increased porosity. VC additives mitigate decreased mechanical properties caused by higher NCC content, emphasizing the crucial role of ink composition and additive selection in achieving desired material properties for advanced 3D-printed ceramics applications. These insights pave the way for innovative approaches in materials engineering and additive manufacturing for nuclear propulsion and other high-performance applications. The integration of AM technologies with advanced materials like ZrC and tailored additives represents a significant step towards efficient and sustainable propulsion systems for future space exploration missions.

Keywords

Zirconium carbide, Additive Manufacturing, Three-interval thixotropy test

6.1 Introduction

Nuclear thermal propulsion works by using nuclear fuel to heat a hydrogen propellant to generate thrust and propel a spacecraft. The higher the gas temperature the larger the specific impulse, hence the better rocket performance. In this regard, ceramic fuel elements have advantage over their metallic counterparts because of their high melting points, chemical stability, corrosion resistance, and high fission product retention [1]. Among ceramic materials for nuclear fuel applications, zirconium carbide (ZrC) is a versatile material with a remarkable combination of properties, including its high melting point, exceptional thermal stability, and efficient neutron absorption capabilities, making it a desirable candidate for such a purpose [2]. In nuclear fuel pellets, zirconium carbide is commonly used as a matrix material for fuel rods. This matrix serves as a protective barrier around the nuclear fuel, which can be in the form of uranium or other fissile materials [3]. However, working with radioactive materials such as uranium carbide requires strict regulations and safety measures, which makes it impractical to handle in an ordinary research lab. Therefore, vanadium carbide (VC) is chosen as a surrogate material for uranium carbide because it is nonradioactive, and both materials have a similar crystal structure [4].

Recent advancements in the field of materials science and engineering have also introduced the utilization of VC as a sintering additive for zirconium carbide, marking a significant leap [5]. Vanadium carbides possess remarkable properties, including high melting points and excellent thermal and mechanical stability, making them an ideal candidate for enhancing the sintering process of ZrC, a material known for its exceptional hardness and refractory nature [6]. The incorporation of vanadium carbides as a sintering aid has led to enhanced densification and improved mechanical properties of the resulting composite materials.

In the realm of ZrC ceramics, the conventional fabrication methods have long grappled with the challenge of producing intricate geometries [7-9]. Crafting complex shapes often necessitated costly machining of these dense, erosion-resistant, and brittle composites, utilizing ultra-hard (diamond) tooling [10]. However, the landscape of ceramics fabrication has undergone a profound transformation with the emergence of Additive Manufacturing (AM), or 3D printing, technology. Various AM techniques, such as binder jetting [11, 12], laser powder bed fusion (LBPF) [13, 14], Stereolithography (SLA) [15-18] and material extrusion [19, 20], have become integral to the field.

Among these methods, Extrusion-based additive manufacturing stands out for its distinctive advantages. Unlike traditional approaches, it offers unmatched material flexibility, accommodating a broad spectrum of materials ranging from polymers and ceramics to metals and bioinks. This versatility empowers the creation of intricate, tailor-made structures designed for specific applications. Furthermore, it facilitates multi-material printing, enabling the construction of composite structures endowed with diverse properties. Noteworthy is its minimal waste production, swift prototyping capabilities, and seamless customization, making it highly coveted in research, development, and various industries. These unique merits position extrusion-based additive manufacturing as a frontrunner in the field, sparking innovation in both manufacturing and scientific endeavors.

In this study, we use an extrusion-based additive manufacturing method for creating zirconium carbide nuclear fuel cell structures. The experimental results highlighted significant findings regarding the impact of NCC and VC additives on the properties of 3D-printed ZrC ceramics. The rheological analysis demonstrated that higher NCC concentrations in the ink formulation resulted in improved ink recovery times, leading to enhanced self-supporting

capacity during printing and reduced deformation of printed structures. Microstructural analysis revealed a delicate balance, where lower NCC concentrations promoted denser microstructures with reduced porosity, positively affecting mechanical properties such as compressive strength and hardness. However, excessive NCC content increased porosity, adversely affecting material integrity. Mechanical testing further confirmed these trends, showing that while higher NCC content generally decreased elastic modulus and compressive strength, the inclusion of VC additives helped mitigate these effects within specific concentration ranges, showcasing improved mechanical properties. These results emphasize the critical role of ink composition and additive selection in achieving desired material properties for advanced applications in 3D-printed ceramics.

6.2 Experimental section

6.2.1 Ink Preparation

As illustrated in Fig. 6-1a, ink is prepared by mixing ZrC/VC powder and water. The incorporation of NCC as a binder and thickener enables precise control over the ink's viscosity, ensuring its printability. The ink was prepared by mixing zirconium carbide powders (with a d50 value of 3-5 micrometers, Standford Advanced Materials, Lake Forest, CA) and vanadium carbide powders (average particle size $\leqslant$ 2 micrometers, Sigma-Aldrich, Saint Louis, MO) in deionized (DI) water at a total solid concentration of 70 wt%. Darvan C-N (Vanderbilt Minerals, Norwalk, CT) as the dispersant was added at 1 wt% based on the total weight of the slurry. The mixture was homogenized for 24 hours using magnetic stirring at 350 rpm. Subsequently, NanoCrystalline Cellulose (CelluForce, Canada) was added as a binder and thickener to adjust the ink's viscosity. The ink was stirred magnetically at 350 rpm and mechanically at 800 RPM until it stabilized.

6.2.2 Design of Experiments (DOE)

To systematically study the impact of both NCC and VC as additives for ZrC, a comprehensive 2-variable 3-level full factorial experimental design was employed. This experimental approach, outlined in Table 6-1, involved varying each variable at low, medium, and high levels, resulting in a total of 9 different inks. These inks were meticulously prepared and printed using consistent parameters as detailed in previous section, providing a structured foundation for analyzing the intricate relationship between material properties and the additives of the ink.

Table 6 - 1 **.** Design of experiments with two major additives for the ink

Ink #	Concentration of NCC	Concentration of VC
1	Low (100mg/mL)	Low (0 vol%)
2	Low (100mg/mL)	Medium (10 vol%)
3	Low (100mg/mL)	High (20 vol%)
4	Medium (150mg/mL)	Low (0 vol%)
5	Medium (150mg/mL)	Medium (10 vol%)
6	Medium (150mg/mL)	High (20 vol%)
7	High (200mg/mL)	Low (0 vol%)
8	High (200mg/mL)	Medium (10 vol%)
9	High (200mg/mL)	High (20 vol%)

6.2.3 Rheology Properties Testing

The suspension rheology was characterized using an MCR92 modular compact rheometer (Anton Paar, Vemon Hills, IL) with a 25 mm parallel plate geometry and a gap of 500 μm. The

three-interval thixotropy test was performed at the shear rate at 0.1 reciprocal seconds [0.1/s] and 5 reciprocal seconds [5/s] at a constant temperature of 25 °C.

6.2.4 3D Printing and Post-processing

Prior to printing, the ink was prepared by loading it into a 30 mL syringe and agitating it using a vortex mixer to remove air bubbles. Following this, the slicing software Cura was utilized to design internal structures and establish printing parameters. The prepared syringe was then connected to a customized 3D printer for the additive manufacturing process, adhering to the predefined patterns illustrated in Fig. 6-1b & c. The ink was dispensed through a 0.413 mm nozzle at a printing speed of 15 mm/s, with a layer height set at 0.5 mm for the printed object. Subsequently, the printed sample was allowed to air-dry naturally at room temperature (25°C) for a duration of 12 hours.

To enhance the strength of the printed samples, a meticulous sintering process was employed involving controlled heating, pressure, and a specialized environment. As depicted in Fig. 6-1d, the furnace chamber underwent three purge cycles: initially reaching a pressure of less than 5x10-2 torr to eliminate air, then reducing the argon backfill to less than 5x10-5 torr (99% removal), and finally decreasing another backfill to less than 5x10-3 torr before filling the furnace to approximately 862 torr with 99% Argon. Following these purges, an argon flow of 500 sccm was initiated before commencing temperature control. The furnace was gradually heated to 1450°C at 10°C per minute monitored using a type C thermocouple, then further raised to 1750°C at 5°C per minute under pyrometer control. After dwelling at 1750°C for 2 hours, the samples were cooled to room temperature over 6 hours, completing the sintering process.

6.2.5 Scanning Electron Microscopy (SEM) Characterization

To assess the microstructural features of the 3D printed ZrC samples, an SEM analysis was conducted using the FEI QUANTA 3D DualBeam SEM/Focused Ion Beam (FIB) system (FEI, Hillsboro, OR). Sample preparation involved mounting the ZrC specimens on SEM stubs with conductive double-sided adhesive tape to ensure stability and high-resolution imaging, followed by sputter-coating with a 10 nm thick gold layer to enhance conductivity and prevent charging effects. The SEM was operated at an accelerating voltage of 30 kV, balancing image resolution and beam penetration. High-resolution SEM images of the ZrC surfaces and cross-sections were captured at various magnifications, providing a detailed view of the specimens' microstructure.

The porosity of the samples was characterized using ImageJ software. Initially, the Threshold function was applied to convert the image to binary, effectively isolating the porosity from the background. Subsequently, Particle Analysis was conducted to quantify the empty area, with the resulting percentage of empty area representing the porosity of the samples.

6.2.6 Mechanical Properties Testing

The uniaxial compressive test was conducted using the Compact Table-Top Universal Tester (Shimadzu, Kyoto, Japan). Cylindrical samples, 10 mm in diameter and 10 mm in height, were prepared and polished with ISO P120 sandpapers. The test was performed in displacement control mode at a rate of 1 mm/min until ultimate failure.

The hardness test was carried out on the same machine, replacing modules with a Vickers indenter. It operated in displacement control mode at 1 mm/min until reaching 4 kgf, followed by a 15-second hold time. Indentation results were analyzed using an optical microscope.

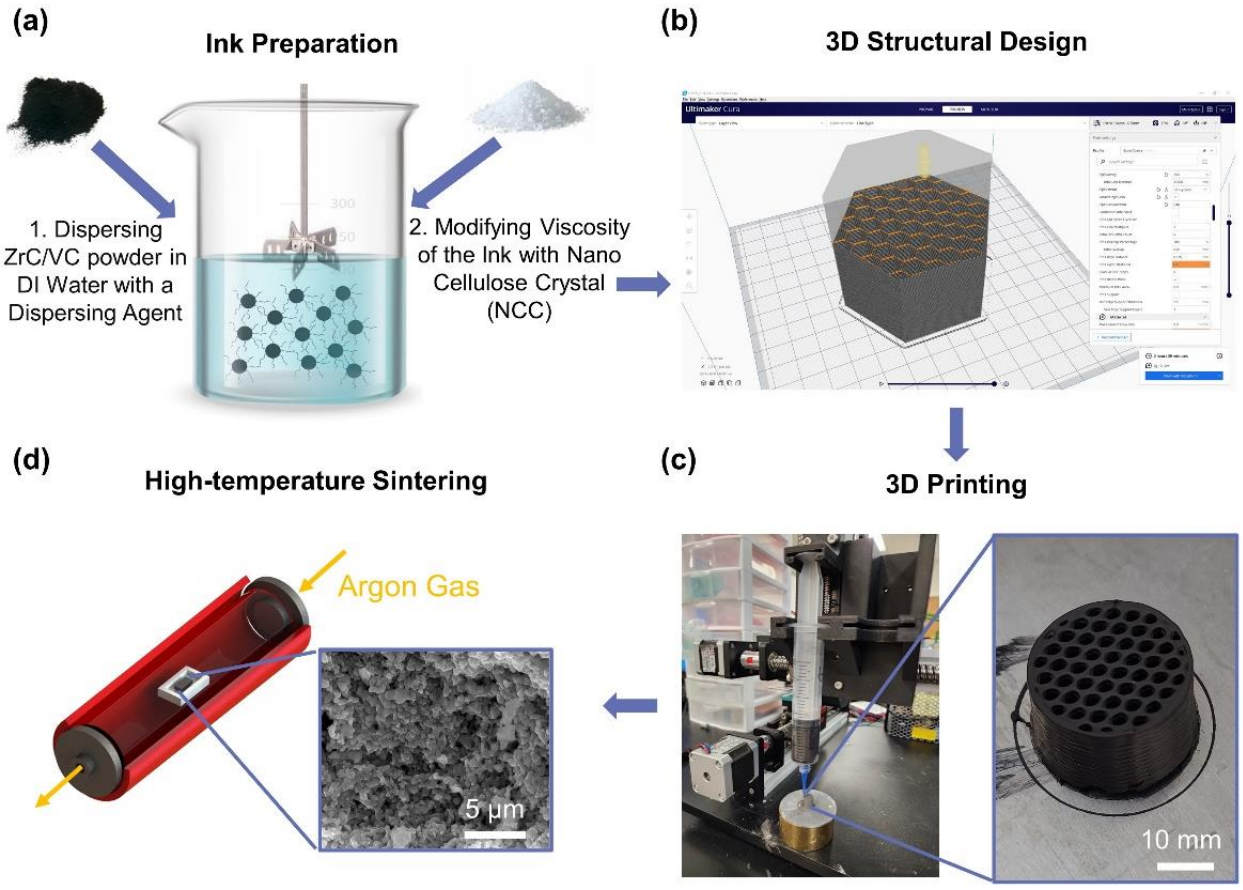

Figure 6-1 Schematic of the 3D Printing process. a) Ink preparation. b) 3D structural design. c) 3D printing. d) High-temperature sintering

6.3 Results and discussion

6.3.1 Rheological Characteristics of the Ink

To achieve self-supporting 3D structures with precise shape fidelity, it is imperative to consider the transition kinetics from a fluid-like flow to a solid-like behavior. Rapid recovery plays a crucial role in ensuring that the printed paste maintains its shape, restoring its elastic behavior and preventing excessive flow immediately after extrusion. This recovery can be quantified by assessing viscosity as shear stress quickly decreases from values exceeding the flow point to low, near-rest shear values.

The three-interval thixotropy test (3ITT) is a rheological assessment that furnishes this critical information and can be conducted in either rotational or oscillatory modes. It simulates an extrusion-based printing process by employing five consecutive steps with varying shear rates (as depicted in Fig. 6-2a): 1. A very slight shear rate within the linear viscoelastic range of the amplitude sweep, mimicking the ink's resting state as it slowly advances through the 3D printing cartridge. 2. An immediate increase in shear rate, resembling the ink's behavior during rapid acceleration. 3. A very high shear rate exceeding the flow point, positioned as close as possible to the maximum shear rate, emulating the extrusion process through a small nozzle. 4. A prompt decrease in shear rate to an extremely low level, enabling the ink to rapidly recover to its high-viscosity state. 5. A return to a very slight shear rate to replicate the ink's resting state after deposition.

The objective of these tests is to evaluate the swift recovery of solid-like behavior to maintain nozzle shape and ensure both accurate printing fidelity and the self-supporting capacity of the printed structure. As depicted in Fig 6-2b, the 3ITT was performed on inks with varying amounts of NCC added. In the initial interval, the rheometer shear rate was set at 0.1 [1/s] for 20 seconds, simulating the ink's slow advancement through the syringe. The viscosity briefly increased due to the acceleration of the rheometer's rotating disks before stabilizing. In the subsequent interval, the disk shear rate abruptly surged to 5 [1/s] for 20 seconds, imitating ink extrusion from the nozzle. During this phase, the ink exhibited fluid-like behavior with a rapid viscosity decrease. In the third interval, the disk shear rate returned to 0.1 [1/s], and the ink's viscosity rapidly recovered to its initial level.

Generally, with increasing NCC content, the ink's viscosity exhibited synchronized growth at both high and low shear rates. However, the crucial finding in these tests, as illustrated

in Fig. 6-2c, was the significant reduction in ink recovery time with higher NCC concentrations. Within the first 5 seconds, inks with 150 and 200 mg/mL NCC added recovered to over 90% of its original viscosity, whereas the ink with 100 mg/mL NCC added only reached 83.62% of its original viscosity. By 15 seconds, the former recovered to 99% of its initial viscosity, while the latter attained only 93.7% of its initial viscosity. This rapid ink recovery time is pivotal for printing outcomes as it significantly influences the self-supporting capacity of the printed structure. Fig. 6-2d further corroborates this characteristic of the ink. Clearly, the ink with low NCC content struggled to maintain the structure, leading to substantial deformation in the bottom structure. In contrast, inks with higher NCC concentrations exhibited robust self-supporting behavior, ensuring stable and accurate printing results.

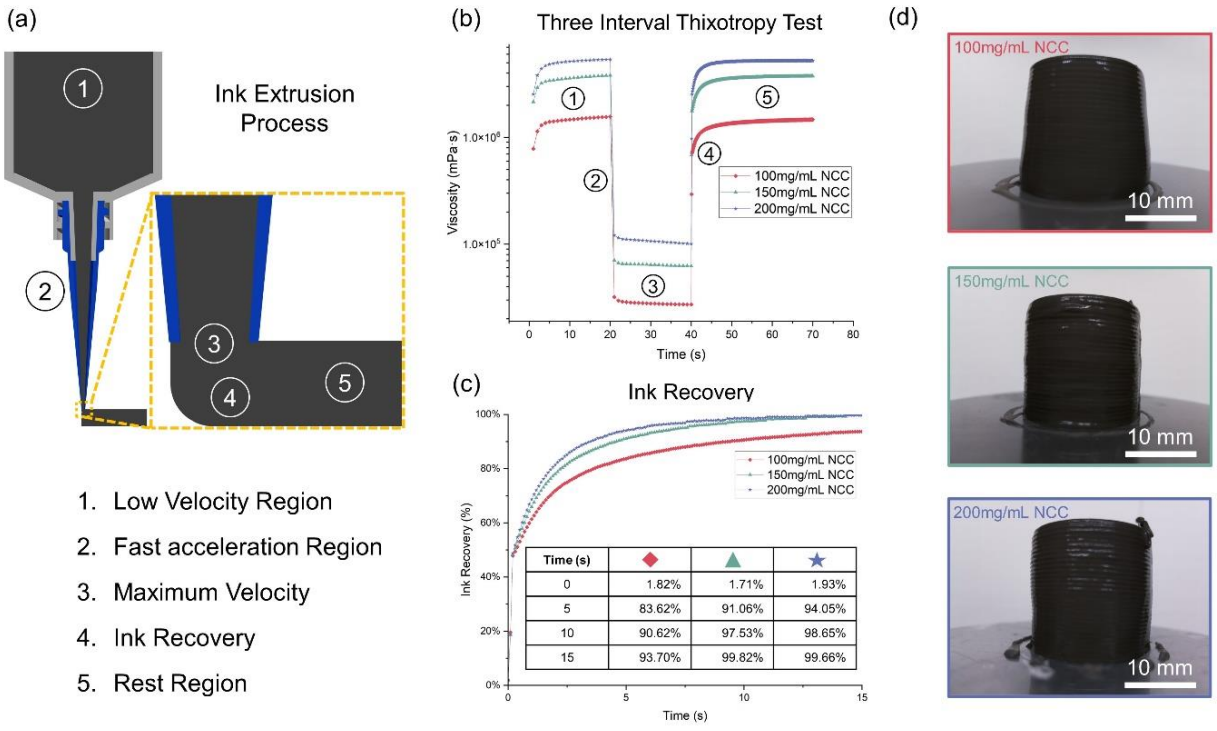

Figure 6-2 a) Ink extrusion process. b) 3ITT result. c) Ink recovery time results. d) Printed ZrC cylindrical sample with different NCC added.

After the samples were printed, they were air-dried at room temperature (25°C) for 12 hours. Time-lapse images were captured every minute during the drying process, as depicted in Fig. 6-3. The top surface diameter, bottom surface diameter, and height of the samples were continuously monitored, enabling the calculation of volumetric shrinkage, as illustrated in Fig. 6-3b. Analyzing three different conditions with varying NCC concentrations revealed a clear trend: the shrinkage decreased from 26.54% to 22.03% as NCC content increased from 100 mg/mL to 200 mg/mL. Notably, the total drying time was also reduced by approximately 2 hours.

The deformation of the printed samples was assessed both before and after the drying process. Due to the ink's varying self-supporting capacity, increased layers during deposition concentrated more weight on the bottom layers, leading to overall shape deformations, particularly at the bottom of the sample. To quantify this deformation, a deviation angle was introduced, measured between the outer surface of the printed cylindrical sample and the vertical reference line. As demonstrated in Fig. 6-3c, the sample with 100 mg/mL NCC exhibited the largest deviation angle at 6.6°, which increased to 7.35° after drying. However, as the NCC concentration increased, the deviation angle decreased significantly by 56.6% to 89.5%. Remarkably, in the case of the sample with 200 mg/mL NCC, the deviation angle reduced from 1.21° to 0.77° after drying. This reduction highlights the substantial improvement in ink's self-supporting capacity due to the increased NCC content, resulting in superior printing and drying outcomes.

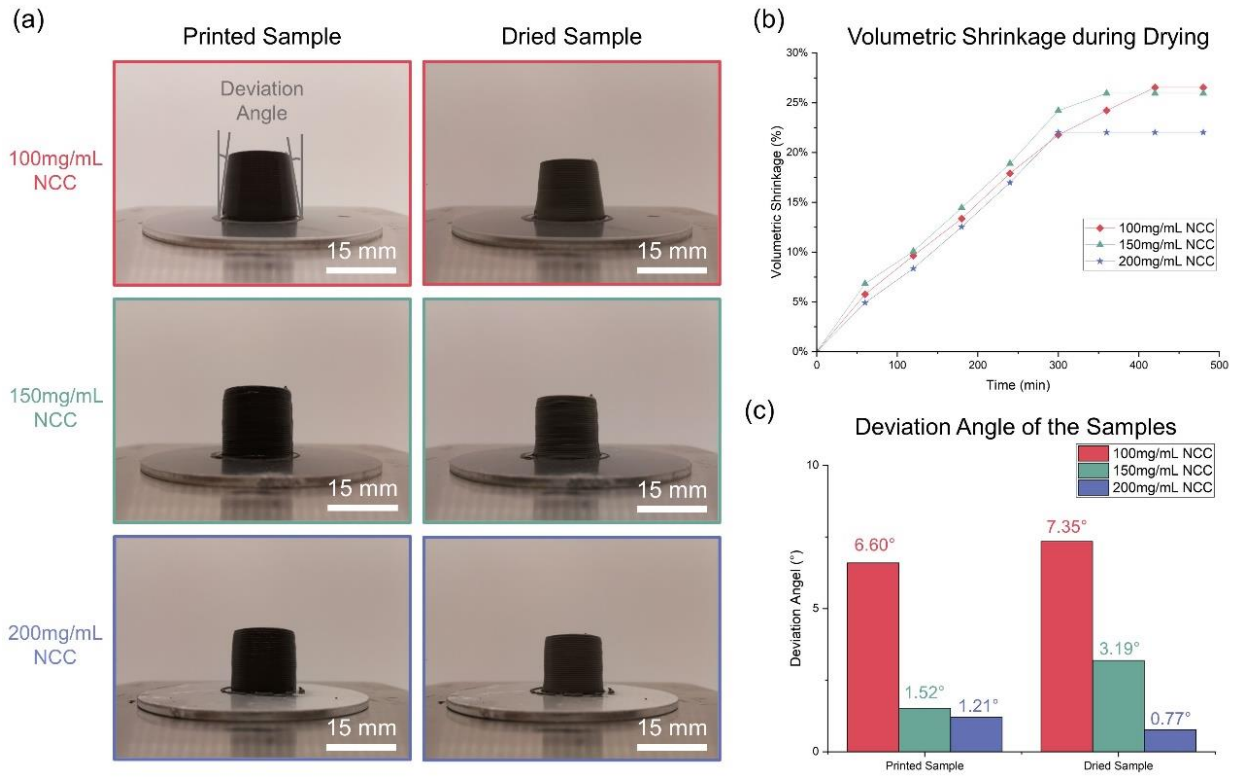

Figure 6-3 a) Images of samples before and after drying process. b) Volumetric shrinkage results during the drying process. c) Deviation angle of the samples before and after drying process.

6.3.2 Microstructure Analysis

The microstructure of 3D-printed ZrC (Zirconium Carbide) samples is a critical aspect that directly influences the material's mechanical properties and overall performance. This microstructure encompasses various factors such as grain size, particle distribution, and porosity, all of which play crucial roles in determining how the material behaves under different conditions. After the samples underwent sintering at 1750°C, the examination of their cross-sections using SEM at high magnification revealed significant insights into their microstructural characteristics. Figure 6-4a provides a visual representation of how the microstructure varies under different conditions, particularly concerning the addition of NCC. When a low concentration of NCC (100mg/mL) is added, it fosters a closer bond among ceramic particles,

resulting in larger grain sizes and reduced porosity. This closer bonding is crucial for enhancing the material's mechanical strength and structural integrity. On the contrary, higher concentrations of NCC lead to increased porosity due to the presence of more voids or gaps among the ceramic particles. These gaps hinder the fusion of particles during sintering, resulting in smaller grain sizes and compromised material properties. The reason behind this behavior lies in the decomposition of NCC during the sintering process. As NCC decomposes, it creates additional space within the particles, making it more challenging for them to sinter effectively. This phenomenon is reflected in the observed microstructural changes and corresponding mechanical properties shown in the next section.

To quantify the porosity accurately, sophisticated image analysis techniques were employed using ImageJ software. Figure 6-4b illustrates the process, where SEM images were meticulously processed to isolate areas of interest containing microstructures. By applying the Threshold function to convert these images into binary form, the porosity areas were effectively separated from the background. Subsequent Particle Analysis provided quantitative data on the empty areas, representing the porosity levels in the samples. To ensure the reliability of the data, multiple images (three per condition) were analyzed, validating the observed trends. Samples with 100mg/mL NCC exhibited the lowest porosity levels (approximately 4%-6%), indicating a denser and more compact microstructure. As the NCC concentration increased to 200mg/mL, porosity levels escalated to 12% and higher, signifying a more porous microstructure with compromised material properties.

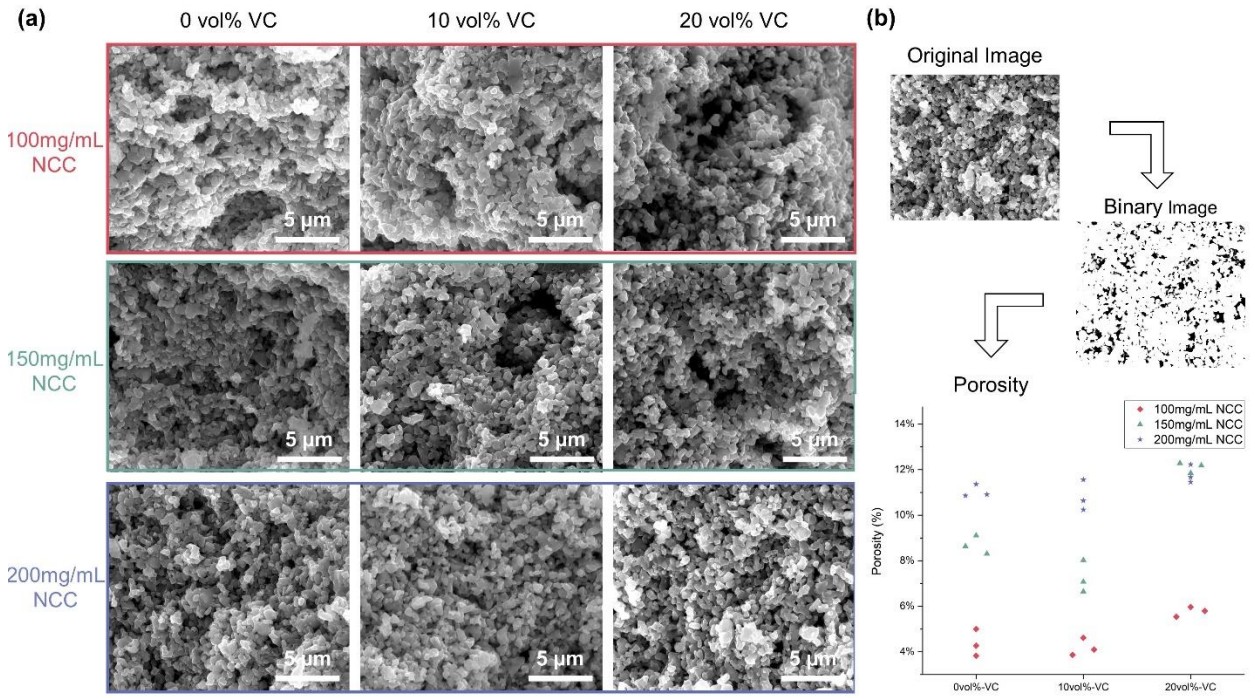

Figure 6-4 a) SEM images depicting cross-sectional views under various conditions. b) Description of the porosity calculation method.

6.3.3 Mechanical Properties

In the realm of 3D printing for advanced applications, such as nuclear fuel cells, understanding and optimizing the mechanical properties of materials is paramount. Zirconium carbide (ZrC), a promising candidate for these purposes, demands meticulous attention to its mechanical traits. Key factors such as elastic modulus, representing a material's ability to deform under stress and return to its original shape, are crucial for ensuring structural integrity and stability within the intricate designs of nuclear fuel cells. Compressive strength, which measures the ability to withstand pushing forces, is vital in enduring the extreme conditions within nuclear reactors. Additionally, hardness, indicating resistance to deformation and wear, is essential for durability and long-term performance. Achieving a delicate balance among these properties is

imperative for the successful 3D printing of ZrC components, ensuring they endure the harsh nuclear environment while maintaining efficiency and safety in fuel cell applications.

Fig. 6-5 shows the mechanical properties tests for the sintered ZrC samples. The typical stress-strain curve of sintered cylindrical ZrC samples under uniaxial compressive test is shown in Fig. 6-5a. Unlike ductile materials, which deform plastically under stress, the ZrC samples exhibited no plastic deformation before fracturing. Due to the brittle nature of the ceramics, the samples failed instantly after getting to its maximum strength and random cracks could be observed through the entire sample. The elastic modulus and compressive strength were obtained from the stress-strain curve generated during the compressive test.

The elastic modulus, a crucial parameter indicating a material's stiffness, was calculated from the linear elastic segment of the stress-strain curve, as illustrated in Fig. 6-5b. Variations in the elastic modulus were observed under different conditions. Specifically, increasing the NCC concentration from 100mg/mL to 150mg/mL caused a significant decrease in the elastic modulus. Surprisingly, further increasing the NCC concentration to 200mg/mL did not result in as substantial a reduction in the elastic modulus. Additionally, incorporating a 10 vol% concentration of VC led to the highest elastic modulus observed for each condition, with an average increase ranging from 8.7% to 15.8%. However, increasing the VC concentration to 20 vol% led to a subsequent decrease in the elastic modulus, sometimes even surpassing samples without added VC.

The compressive strength, as shown in Fig. 6-5c, indicating the maximum stress a material can withstand without failure, was determined from the point on the stress-strain curve where the stress significantly deviated from linearity and began to decrease. Despite inherent fluctuations due to the brittle nature of ZrC samples, the trend closely followed that of the elastic

modulus. Generally, an increase in NCC content led to a decrease in compressive strength. However, the introduction of a 10 vol% concentration of VC resulted in notably higher compressive strength compared to other tested conditions, with an average increase ranging from 24.7% to 48.9%.

Finally, micro indentation tests were conducted on samples under nine distinct conditions employing Vickers' indentation method with a diamond indenter. The results of the hardness tests are depicted in Fig. 6-5d, indicating consistent outcomes. Increased NCC content corresponded to reduced hardness, whereas a 10 vol% concentration of VC exhibited comparatively superior hardness compared to other conditions. The addition of 10 vol% of VC resulted in an average hardness increase ranging from 37.2% to 52.5%.

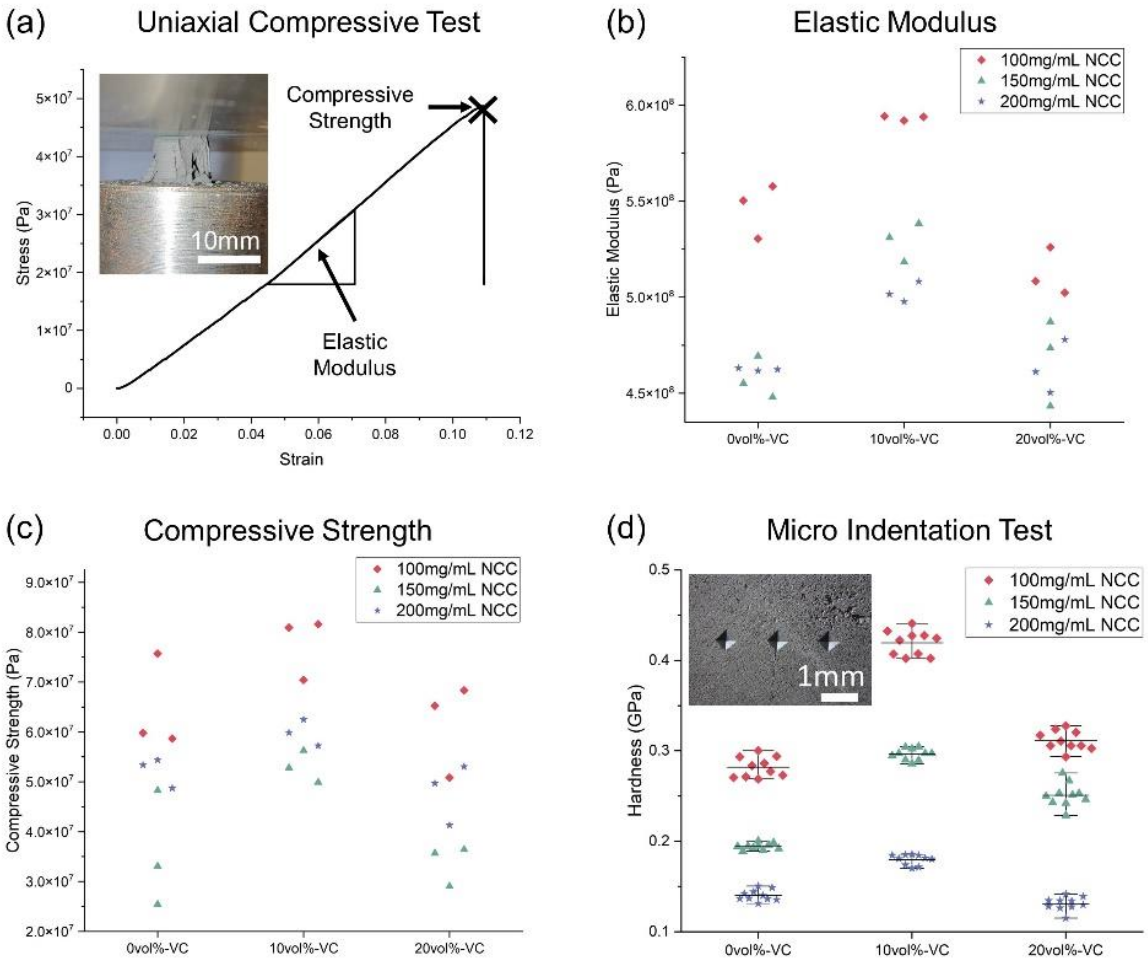

Figure 6-5 a) Mechanical properties of the sintered samples a) Uniaxial compressive test. b) Elastic modulus. c) Compressive strength. c) Micro indentation tests.

6.4 Conclusions and future work

The comprehensive study on the preparation and characterization of ZrC/VC ink for 3D printing applications has provided valuable insights into optimizing ink formulations and understanding the resulting material properties. Through systematic ink preparation and rheological analysis, it was observed that the addition of Nano Crystalline Cellulose (NCC) as a binder and thickener significantly influenced ink viscosity and recovery behavior during the printing processes. Higher concentrations of NCC led to improved ink recovery times, enhancing the self-supporting capacity of printed structures and reducing deformation.

The microstructure analysis of 3D-printed ZrC samples revealed a delicate balance between NCC concentration and the resulting porosity levels. Lower concentrations of NCC facilitated denser microstructures with reduced porosity, positively impacting mechanical properties such as compressive strength and hardness. However, excessive NCC content resulted in increased porosity, affecting material integrity and mechanical performance.

Mechanical testing, including uniaxial compressive tests and hardness evaluations, highlighted the influence of NCC and VC concentrations on material properties. While higher NCC content generally reduced elastic modulus and compressive strength, the incorporation of vanadium carbide (VC) additives mitigated these effects, showcasing improved mechanical properties under specific concentration ranges.

Overall, this study underscores the importance of precise ink formulation, rheological control, and additive selection for achieving desired material properties in 3D-printed ZrC ceramics. Future research directions may focus on further optimizing ink compositions, exploring

additional additives, and investigating post-printing treatments to enhance the performance and applicability of printed ZrC ceramic components in advanced engineering applications.

Acknowledgement

This material is based upon work supported by the National Aeronautics and Space Administration under Cooperative Agreement No. 80NSSC22M0261.

References

[1] J. Marra, Advanced ceramic materials for next-generation nuclear applications, IOP Conference Series: Materials Science and Engineering, IOP Publishing, 2011, pp. 162001.

[2] Y. Katoh, G. Vasudevamurthy, T. Nozawa, L.L. Snead, Properties of zirconium carbide for nuclear fuel applications, Journal of Nuclear Materials, 441 (2013) 718-742.

[3] S. Hamilton, N.D. Jerred, R. Scott, M. Bachhav, T. Yao, V.M. Miller, Diffusion study of uranium mononitride/zirconium carbide composite for space nuclear propulsion, Journal of Nuclear Materials, 583 (2023) 154535.

[4] B. Taylor, B. Emrich, D. Tucker, M. Barnes, N. Donders, K. Benensky, Study of a Tricarbide Grooved Ring Fuel Element for Nuclear Thermal Propulsion, 2018.

[5] X.-G. Wang, J.-X. Liu, Y.-M. Kan, G.-J. Zhang, Effect of solid solution formation on densification of hot-pressed ZrC ceramics with MC (M= V, Nb, and Ta) additions, Journal of the European Ceramic Society, 32 (2012) 1795-1802.

[6] L. Wu, T. Yao, Y. Wang, J. Zhang, F. Xiao, B. Liao, Understanding the mechanical properties of vanadium carbides: Nano-indentation measurement and first-principles calculations, Journal of alloys and compounds, 548 (2013) 60-64.

[7] D. Gosset, M. Dollé, D. Simeone, G. Baldinozzi, L. Thomé, Structural evolution of zirconium carbide under ion irradiation, Journal of nuclear materials, 373 (2008) 123-129.

[8] G.-M. Song, Y.-J. Wang, Y. Zhou, The mechanical and thermophysical properties of ZrC/W composites at elevated temperature, Materials Science and Engineering: A, 334 (2002) 223-232.

[9] T. Zhang, Y. Wang, Y. Zhou, T. Lei, G. Song, Elevated temperature compressive failure behavior of a 30 vol.% ZrCp/W composite, International Journal of Refractory Metals and Hard Materials, 25 (2007) 445-450.

[10] C.B. Carter, M.G. Norton, Ceramic materials: science and engineering, Springer2007.

[11] J. Gonzalez, J. Mireles, Y. Lin, R.B. Wicker, Characterization of ceramic components fabricated using binder jetting additive manufacturing technology, Ceramics International, 42 (2016) 10559-10564.

[12] W. Du, X. Ren, C. Ma, Z. Pei, Ceramic binder jetting additive manufacturing: Particle coating for increasing powder sinterability and part strength, Materials Letters, 234 (2019) 327-330.

[13] K. Shahzad, J. Deckers, J.-P. Kruth, J. Vleugels, Additive manufacturing of alumina parts by indirect selective laser sintering and post processing, Journal of Materials Processing Technology, 213 (2013) 1484-1494.

[14] S.L. Sing, W.Y. Yeong, F.E. Wiria, B.Y. Tay, Z. Zhao, L. Zhao, Z. Tian, S. Yang, Direct selective laser sintering and melting of ceramics: a review, Rapid Prototyping Journal, 23 (2017) 611-623.

[15] B. Mansfield, S. Torres, T. Yu, D. Wu, A review on additive manufacturing of ceramics, International Manufacturing Science and Engineering Conference, American Society of Mechanical Engineers, 2019, pp. V001T001A001.

[16] Z. Chen, Z. Li, J. Li, C. Liu, C. Lao, Y. Fu, C. Liu, Y. Li, P. Wang, Y. He, 3D printing of ceramics: A review, Journal of the European Ceramic Society, 39 (2019) 661-687.

[17] H. Wu, Y. Cheng, W. Liu, R. He, M. Zhou, S. Wu, X. Song, Y. Chen, Effect of the particle size and the debinding process on the density of alumina ceramics fabricated by 3D printing based on stereolithography, Ceramics International, 42 (2016) 17290-17294.

[18] H. Xing, B. Zou, S. Li, X. Fu, Study on surface quality, precision and mechanical properties of 3D printed ZrO2 ceramic components by laser scanning stereolithography, Ceramics International, 43 (2017) 16340-16347.

[19] H. Shao, D. Zhao, T. Lin, J. He, J. Wu, 3D gel-printing of zirconia ceramic parts, Ceramics International, 43 (2017) 13938-13942.

[20] M. Faes, J. Vleugels, F. Vogeler, E. Ferraris, Extrusion-based additive manufacturing of ZrO2 using photoinitiated polymerization, CIRP Journal of Manufacturing Science and Technology, 14 (2016) 28-34.

Chapter 7 - Summary and Future Work

The thesis delves comprehensively into the development and utilization of a groundbreaking technique termed 3D Freeze Printing (3DFP) aimed at addressing the intricate challenges faced in the realm of aerogel manufacturing. This innovative approach seamlessly integrates the principles of freeze casting with additive manufacturing (AM) methodologies, presenting a promising avenue for advancing aerogel production techniques. The primary objectives of this research encompass a meticulous characterization of the 3DFP process, an expansion of its material applicability horizon, and a comparative analysis evaluating the multifaceted aerogels produced through 3DFP against traditionally manufactured counterparts.

The research journey embarks upon a thorough exploration of freeze casting techniques alongside established extrusion-based 3D printing methods. This initial phase involves leveraging cutting-edge imaging tools such as X-ray synchrotron micro-radiography to enable real-time monitoring and analysis of material behaviors during both freeze casting and 3DFP processes. This holistic understanding serves as a foundational pillar for optimizing the 3DFP approach across various industrial sectors.

A pivotal highlight of the thesis lies in the detailed production and comprehensive analysis of cellulose nanocrystal (CNC) aerogels using the 3DFP method. This investigation not only underscores the exceptional acoustic absorption capabilities of CNC aerogels but also highlights their tailored mechanical attributes achieved through freezing direction manipulation. The demonstrated potential of these aerogels in lightweight sound absorption devices, especially within aerospace contexts, signifies a significant breakthrough in lightweight material technology with wide-ranging implications.

Moreover, the research extends its exploratory reach into the domain of extrusion-based 3D printing, focusing specifically on the fabrication of zirconium carbide (ZrC) nuclear fuel cell structures. The study delves deep into elucidating the influence of incorporating additives such as Nano Crystalline Cellulose (NCC) and Vanadium Carbide (VC) on the rheological and mechanical properties of these intricate structures. This integration of additive manufacturing principles with advanced materials not only marks substantive progress towards sustainable propulsion systems for space exploration but also underscores the potential synergies between cutting-edge material science and futuristic technological advancements.

In conclusion, this thesis significantly contributes to the forward march of materials science and advanced manufacturing, particularly in optimizing aerogel manufacturing processes tailored to meet the diverse needs of various industries. By addressing critical challenges inherent in aerogel fabrication and harnessing the potential of innovative methodologies like 3DFP, this research not only paves the way for futuristic technologies but also advocates for sustainable industrial practices within the aerogel applications domain. Furthermore, this research emphasizes the importance of bridging theoretical insights with practical industrial applications, fostering interdisciplinary collaborations across sectors ranging from chemical and machinery to electronics, aerospace, and biomedical engineering. Ultimately, this dissertation serves as a catalyst for advancing aerogel technology, unlocking new avenues in multifunctional material design, and propelling sustainable technological innovations across a spectrum of industrial domains, thereby shaping a brighter and more sustainable future.

Recommendations for future work:

- Expansion of Material Types: Investigate and incorporate a wider range of materials beyond silica, CNC, and ZrC for aerogel fabrication. Explore new material combinations and formulations to tailor aerogels for specific industry applications.
- Optimization of 3DFP Process: Conduct systematic studies to optimize extrusion processes in 3DFP for enhanced control over aerogel properties. This includes exploring freezing direction modifications, additive concentrations, and printing parameters.
- Multifunctional Aerogels Evaluation: Conduct comprehensive evaluations of multifunctional properties such as mechanical strength, thermal conductivity, and adsorption capacities for aerogels fabricated using 3DFP. Compare these properties with conventionally fabricated aerogels for performance validation.
- Industry-Specific Applications: Collaborate with industries like chemical, machinery, electronics, aerospace, and biomedical engineering to develop customized aerogel solutions. Focus on addressing industry-specific challenges and requirements for aerogel materials.
- Sustainable Technological Advancements: Continue research on sustainable additives and manufacturing processes for aerogels. Aim to improve eco-friendliness and sustainability profiles of aerogel materials for future industrial applications.
- Space Exploration and Propulsion Systems: Explore the performance of aerogels, including nano-cellulose aerogels and advanced ceramic aerogels, under extreme conditions relevant to space environments. Collaborate with space agencies and aerospace companies for validation and integration into space technologies.